CHARACTERIZING ASTROPHYSICAL SOURCES OF GRAVITATIONAL WAVES

by

Joey Shapiro Key

A dissertation submitted in partial fulfillment
of the requirements for the degree

of

Doctor of Philosophy

in

Physics

MONTANA STATE UNIVERSITY
Bozeman, Montana

April, 2010

APPROVAL

of a dissertation submitted by

Joey Shapiro Key

This dissertation has been read by each member of the dissertation committee and has been found to be satisfactory regarding content, English usage, format, citations, bibliographic style, and consistency, and is ready for submission to the Division of Graduate Education.

Dr. Neil J. Cornish

Approved for the Department of Physics

Dr. Richard J. Smith

Approved for the Division of Graduate Education

Dr. Carl A. Fox

STATEMENT OF PERMISSION TO USE

In presenting this dissertation in partial fulfillment of the requirements for a doctoral degree at Montana State University, I agree that the Library shall make it available to borrowers under rules of the Library. I further agree that copying of this dissertation is allowable only for scholarly purposes, consistent with "fair use" as prescribed in the U.S. Copyright Law. Requests for extensive copying or reproduction of this dissertation should be referred to ProQuest Information and Learning, 300 North Zeeb Road, Ann Arbor, Michigan 48106, to whom I have granted "the exclusive right to reproduce and distribute my dissertation in and from microform along with the non-exclusive right to reproduce and distribute my abstract in any format in whole or in part."

Joey Shapiro Key

April, 2010

DEDICATION

In memory of Dr. William A. Hiscock.

TABLE OF CONTENTS

TABLE OF CONTENTS – CONTINUED

LIST OF TABLES

Table Page

LIST OF FIGURES

Figure Page

LIST OF FIGURES – CONTINUED

Figure Page

LIST OF FIGURES – CONTINUED

Figure Page

LIST OF FIGURES – CONTINUED

Figure Page

ABSTRACT

The Laser Interferometer Space Antenna (LISA) and the Laser Interferometer Gravitational-wave Observatory (LIGO) are designed to detect gravitational waves from a wide range of astrophysical sources. The parameter estimation ability of these detectors can be determined by simulating the response to predicted gravitational wave sources with instrument noise and searching for the signals with sophisticated data analysis methods. A possible source of gravitational waves will be beams of radiation from discontinuities on cosmic length strings. Cosmic strings are predicted to form kinks and cusps that travel along the string at close to the speed of light. These disturbances are radiated away as highly beamed gravitational waves that produce a burst-like pulse as the cone of emission sweeps past an observer. The detection of a gravitational wave signal from a cosmic string cusp would illuminate the fields of string theory, cosmology, and relativity. Gravitational wave sources also include coalescing binary systems of compact objects. Colliding galaxies have central black holes that sink to the center of the merged galaxy and begin to orbit one another and emit gravitational waves. Previous LISA data analysis studies have assumed that binary black hole systems have a circular orbit or an extreme mass ratio. It is ultimately necessary to understand the general case of spinning black hole binary systems in eccentric orbits and how LISA observations can be used to measure the eccentricity of the orbits as well as the masses, spins, and luminosity distances of the black holes. Once LISA is operational, the comparison of observations of eccentric and circular black hole binary sources will constrain theories on galaxy mergers in the early universe.

CHAPTER 1
INTRODUCTION

In the next two decades, the field of gravitational wave astronomy will make revolutionary contributions to both astronomy and physics. The ground based detector network including the Laser Interferometer Gravitational-Wave Observatory (LIGO) [1] and Virgo [2] has completed five science runs and is poised to make the first direct detection of gravitational waves. The Laser Interferometer Space Antenna (LISA) [3] will observe the low frequency gravitational wave region from 10^{-5} Hz to 1 Hz to complement the frequency range for the ground based detectors from approximately 10 Hz to 10 kHz. The LISA frequency range is guaranteed to contain sources of strong gravitational waves and also offers tremendous potential for new and possibly unexpected discoveries. Arrays of pulsars form a natural very long arm length gravitational wave detector and the timing residuals of their pulses can also be used to search for very low frequency gravitational waves in the range from 10^{-9} Hz to 10^{-6} Hz distorting the space-time between the Earth and the observed pulsars [4].

The ability of these instruments to detect gravitational waves depends on advanced data analysis solutions to extract gravitational waveforms from the intrinsically noisy data. LIGO has developed a sophisticated pipeline to analyze their data and has already made interesting astrophysical statements from gravitational wave non-detections [5]. The LISA mission has demonstrated successful source parameter determination with realistic simulated data for a wide range of possible LISA sources through the Mock LISA Data Challenges [6].

For very wide frequency band gravitational wave sources we can study the ability of LISA and the LIGO-Virgo network to make joint detections. Topological defects known as cosmic superstrings are a consequence of several classes of theories about

the early universe and their detection would illuminate the fields of string theory, cosmology, and relativity. Cusps and kinks on long cosmic strings are predicted to create beams of gravitational radiation with a wide frequency spectrum that would be detectable by LISA and the network of gravitational wave detectors here on the Earth. We have developed search techniques to find multiple cusp signals in simulated data and estimate the parameters of each individual source. Our study demonstrates the ability of space-borne and ground-based gravitational wave detectors to detect and characterize the gravitational wave signals from cosmic string cusps. Our work demonstrates that, should they exist, cosmic strings will indeed be a detectable source for Advanced LIGO and the LISA mission.

Inspiraling binaries of compact objects such as black holes are promising sources for current and future gravitational wave detectors. Binary black hole systems have been studied in various special limits such as circular orbits, extreme mass ratio inspirals (EMRIs), or specific spin orientations (for example [7, 8, 9, 10]). The general case of gravitational waveforms from spinning black hole binaries with comparable masses and eccentric orbits includes the full seventeen parameters necessary to describe a generic binary black hole system. These general waveforms are necessary to accurately measure parameter values for binary black hole systems, constrain galaxy merger scenarios, and test the theory of general relativity in the strong field regime.

There is substantial observational evidence for black holes with $M \sim 10M_{\odot}$ with stellar companions in x-ray binaries (XRB) (see [11] for a review). There could also exist binary systems of these stellar mass black holes that would be difficult to detect with electromagnetic astronomy. Conventional telescopes cannot see through the plane of our galaxy because their view is obscured by gas and dust. Gravitational waves however travel unimpeded through the obscuring material that blocks photons, so the gravitational waves emitted by millions of binaries of stellar remnants in our

galaxy can reach us here in our solar system. The data from gravitational wave detectors will have a large impact on our understanding of stellar evolution and compact binary formation.

The history of galaxy evolution in the universe will be illuminated by the study of massive black hole mergers with black hole masses in the range $M \sim 10^5 - 10^7 M_\odot$. There exists mounting evidence that when galaxies collide their central black holes sink to the center of the merged galaxy and begin to orbit one another, losing energy and angular momentum in the form of gravitational waves [12, 13]. These systems will be strong sources for LISA [14]. While it has previously been assumed that the gravitational wave signals from most massive black hole binary systems will enter the LISA band only after the orbit has been circularized, there are models that predict that LISA could observe systems with significant orbital eccentricity [15]. We have thus relaxed the assumption of circular orbits to calculate gravitational waveform templates that make it possible to accurately measure the eccentricity of binary black hole systems with LISA, along with precise measurements of the masses, spins, and luminosity distances. These other parameters will be quite well determined for black hole binary systems and a bias in these parameters can be avoided by using the general eccentric waveforms, even in the case of very small eccentricity.

Our studies show that even very small values of orbital eccentricity are detectable for LISA on the order of $e = 10^{-3}$. Neglecting the effects on the waveforms due to eccentricity results in a loss of estimated power and a bias in the values of the other parameters [16]. Finding departures from the theory of general relativity with black hole waveforms also requires the fully eccentric waveforms since the eccentricity effects are on the order of possible departures from theory [17]. The strong field regime around supermassive black holes offers the best tests for Einstein's theory

by measuring coherent residuals left after subtracting an eccentric binary black hole template from the data.

Our data analysis methods use comparisons of templates generated for different source parameters with synthesized LISA data. We focus on examples of supermassive black hole binaries, but these methods are also useful for studying gravitational wave signals from the stellar mass black hole binary population. The seventeen dimensional parameter space describing binary black hole systems makes grid based template searches computationally prohibitive and successful hierarchical grid searches unnecessarily demanding of specific tailoring. Our search methods avoid these problems by using Markov Chain Monte Carlo (MCMC) techniques, including parallel tempering of the chains to ensure full exploration of the available parameter space. MCMC methods have the added benefit of producing the posterior distribution function (PDF) of the search space, yielding accurate uncertainty values for each parameter. Our eccentric binary black hole study establishes how well the various source parameters will be resolved by the LISA mission and provides the first steps in creating the templates necessary for measuring orbital eccentricity and comparing theories that make predictions about the shapes of the orbits of binary black holes in the center of merged galaxies.

CHAPTER 2

CONVENTIONS

The units in this document will be based on the usual choice of geometrical units for relativity topics where Newton's gravitational constant and the speed of light are set to 1, $G = c = 1$. This choice results in mass, distance, and time all measured in seconds. Frequencies will still be given in Hertz. The exception is the gravitational wave detector section 3.3.1 where c will be used explicitly.

Vector quantities will be written in bold face type, while their magnitudes will be reported in standard type. For instance $\mathbf{V}$ is a vector with magnitude V.

A time derivative will be denoted by an over-dot, such that

$$\dot{f}(t) = \frac{d\, f(t)}{dt} \quad .$$

CHAPTER 3

GRAVITATIONAL WAVES

3.1 Introduction

The General Theory of Relativity [18] predicts disturbances in space-time produced by time varying mass distributions. These ripples in space are known as gravitational waves. A binary system of two stars orbiting one another will create gravitational waves that will carry away energy and angular momentum from the system. Gravitational waves have been indirectly detected in this context with the observations made by Russell Hulse and Joseph Taylor of the pulsar PSR B1913+16, also known as the Hulse-Taylor pulsar [19]. Their observations of this neutron star that emits beams of radiation indicated that it was in a binary orbit with a companion star. General relativity makes exact predictions for how much energy the system should lose due to gravitational wave emission. Long term observation of the pulsar revealed a decay in the orbit of the stars that exactly matched the prediction of general relativity and Hulse and Taylor were awarded the Nobel Prize for Physics in 1993 for their discovery.

The direct detection of gravitational waves is the challenging and exciting next step toward the era of gravitational wave astronomy. There exists a network of gravitational wave detectors here on Earth and there are plans to build a space based detector in the next decade. The ground based detectors include the LIGO instruments in Hanford, Washington and Livingston, Louisiana [1, 20], the Virgo detector near Pisa, Italy [2, 21] and GEO 600 near Sarstedt, Germany [22, 23]. These are L-shaped laser interferometric detectors that seek to measure the distance changes in their long arms as gravitational waves pass through the Earth. The LIGO-Virgo

network has completed five science runs and though they have yet to make a direct detection of a gravitational wave signal they have already made significant contributions to astronomy. In 2007 a Gamma Ray Burst (GRB) event detected from the direction of the nearby Andromeda Galaxy was ruled out as a neutron star merger in the Andromeda Galaxy with high confidence by the non-detection of gravitational waves from the event by LIGO [5].

The future of gravitational wave astronomy lies with the upgrade of the ground based detectors to their advanced configurations and the launch of the LISA observatory. The advanced ground based detectors will have increased sensitivity to gravitational waves more than a factor of ten beyond initial LIGO, resulting in an increase in event rates by one thousand fold. LISA will be able to detect gravitational wave frequencies unaccessible to the ground based instruments in a range guaranteed to be rich in sources of gravitational waves.

With the new generation of gravitational wave detectors we will begin the era of gravitational wave astronomy. Electromagnetic observatories will be able to work together with gravitational wave observatories and the pulsar timing arrays to answer some of the outstanding questions in astronomy as well as make new and exciting discoveries. In preparation for the first direct detection of gravitational waves, gravitational wave astronomers have been developing the tools that will be necessary to analyze the data from their detectors to determine the characteristics of the sources they will be observing. Understanding the instruments and their sources of noise as well as the possible sources of gravitational waves is essential to our ability to do precision gravitational wave astronomy and finally test general relativity in the strong field regime near massive bodies such as black holes.

3.2 Sources of Gravitational Waves

The description of gravity as the curvature of space-time leads to the concept of the propagation of gravity. Massive bodies such as stars warp the space around them. When two bodies orbit one another, moving through space-time, the curvature moves with them. Such time varying asymmetric mass distributions produce gravitational radiation, ripples in space-time that propagate at the speed of light. The universe creates a number of systems predicted to be sources of gravitational waves.

Mountains on rotating neutron stars and the asymmetric collapse of the core of an exploding star will radiate energy in the form of gravitational radiation. Most stars in the universe come in systems of two or more objects orbiting around one another. The strongest sources of gravitational waves will be the systems consisting of compact objects such as white dwarfs, neutron stars, or black holes. These compact binary star systems emit gravitational waves in three phases: as they spiral in toward one another, as they merge to create a single object, and as the merged star rings down to a symmetric configuration. Understanding each of these phases adds to our ability to detect the gravitational wave signals from binary star systems.

There also exists the possibility that gravitational wave detections will provide observational tests for some of the exotic theories in cosmology, including string theory and alternative theories of gravity. There may be a network of long strings in the universe with a gravitational wave signature that would be detectable by the next generation of gravitational wave instruments. Cusps would tend to form on these cosmic length strings and a segment of the cusp could be moving near the speed of light. This time variation in the concentration of energy would produce a beam of gravitational radiation.

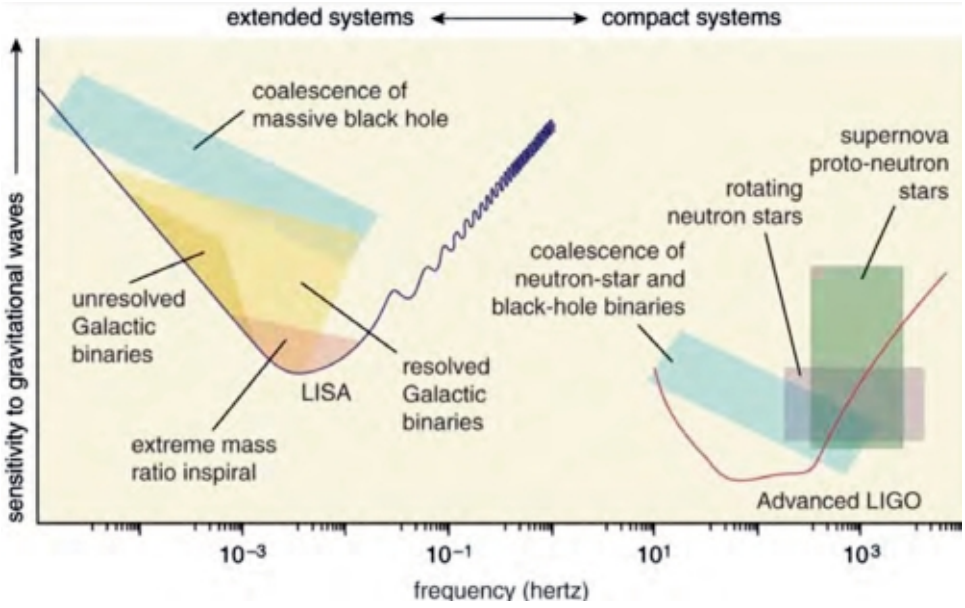

Figure 3.1: The characteristic strain sensitivity curves for LISA (blue) and Advanced LIGO (red). Frequency and characteristic strain ranges for several gravitational wave source types are indicated by shaded regions. Image from the LISA Science Case document [24].

Theories of gravity that pass observational tests in the solar system and in binary pulsar systems still need to be tested in the strong field regime near a black hole. The orbits of small bodies spiraling in toward a supermassive black hole will be sensitive probes of the structure of space-time near a supermassive black hole. The gravitational waves from these Extreme Mass Ratio Inspirals (EMRIs) will provide the evidence we need to test competing theories of gravity.

Gravitational wave observations have the potential to reach back farther than the oldest light in the universe to probe times before the universe had cooled enough to allow photons to propagate freely through space. The Comic Microwave Background (CMB) radiation is the isotropic signal reaching us from 380,000 years after the Big Bang, when the hot young universe had cooled enough to allow neutral atoms to form and light to propagate through the expanding universe [25]. Electromagnetic

observations cannot reach back farther than the last scattering surface, but primordial gravitational waves are reaching us from earlier times carrying information about the very early universe.

One of the most exciting aspects of opening the door to an entirely new branch of astronomy will be the unpredicted discoveries. Just as each new band of the electromagnetic spectrum brought predicted and totally new discoveries to light, gravitational wave astronomy will teach us unexpected lessons about our universe.

3.3 Gravitational Wave Detectors

To detect gravitational waves an instrument must be designed that can measure small changes in the distance between free moving masses. There are three primary ways to achieve this goal, with resonant mass bar detectors, pulsar timing experiments, or interferometers. Bar detectors made the first attempts to measure gravitational waves, but have not proved sensitive enough to make detections. The sensitivities needed to capture gravitational wave signals can be reached by building large scale laser interferometer detectors or by using a natural detector formed by the local array of millisecond pulsars.

3.3.1 The Laser InterferometerGravitational-wave Observatory

The Laser Interferometer Gravitational-wave Observatory (LIGO) is a National Science Foundation (NSF) project designed to directly detect gravitational waves [1, 20]. The two LIGO sites in Hanford, Washington and Livingston, Louisiana consist of L-shaped interferometers with 4 kilometer long arms. Laser light is divided by a beam splitter and travels down the long vacuum tubes to mirrors at the end stations that reflect the light back to the central station. Precise measurements determine if

the relative lengths of the two arms have changed due to a passing gravitational wave. To be sensitive to gravitational waves, the LIGO detectors must be able to measure distance changes one thousand times smaller than the width of a proton.

The sensitivity of ground based interferometers such as LIGO to gravitational wave signals can be understood by describing the fundamental noise sources and the instrument response. The gravitational wave amplitude that can be detected depends on the search for the specific kind of signal in question, but we expect a possible gravitational wave amplitude at the Earth of $h \sim 10^{-21}$. For the LIGO detectors with arm length $L = 4$ km, the interferometer needs to be able to measure distance changes $\Delta L = (1/2)hL \sim 2 \times 10^{-18}$ m. The possibility of such precision measurements with laser interferometry was thoroughly analyzed in Ref. [26]. The displacement measurement accuracy represents the coherent displacement of all of the atoms of the macroscopic mirrors. It may be more illuminating to consider the corresponding phase shift of the laser light for detection at this level. Following the calculations in Ref. [27], the phase shift $\Delta\phi$ can be calculated for a Michelson interferometer and for a Michelson interferometer with Fabry-Perot cavities as is the case for LIGO:

$$\begin{aligned} \Delta\phi_{\rm Mich} &= \frac{4\pi}{\lambda_L} hL \\ \Delta\phi_{\rm FP} &= \frac{2\mathcal{F}}{\pi} \Delta\phi_{\rm Mich} \end{aligned} \tag{3.1}$$

where $\lambda_L = 1\mu$m is the laser wavelength and $\mathcal{F} = 200$ is the finesse of the cavity with LIGO values. So we aim to measure a phase shift with LIGO $\Delta\phi_{\rm FP} \sim 10^{-8}$ rad.

The sensitivity of an interferometer to gravitational wave signals is often expressed as the transfer function $T(f)$, relating the detector input to the detector output. The transfer function of a Michelson interferometer with Fabry-Perot cavities can be

approximated by

$$T_{\rm FP}(f) \simeq \frac{8\mathcal{F}L}{\lambda_{\rm L}} \frac{1}{\sqrt{1+(f/f_p)^2}} \tag{3.2}$$

where f_p is the pole frequency related to the storage time in the cavity $\tau_{\rm S}$ and defined by

$$f_p \equiv \frac{1}{4\pi\tau_{\rm S}} \simeq \frac{c}{4\mathcal{F}L} \ . \tag{3.3}$$

If we consider various noise sources as the detector input in the absence of a gravitational wave signal and divide by the transfer function we can calculate the strain sensitivity of the detector to compare with a gravitational wave signal h.

We can understand the frequency range where LIGO is sensitive to gravitational waves by finding the strain sensitivity due to some of the fundamental noise sources. The LIGO noise sources associated with the laser system are the shot noise and radiation pressure. The laser light comes in discrete photon packets and there are uncertainties associated with the counting statistics for the arrival of discrete independent events. The number of photons N_γ arriving at the photodetector in an observation time T follows the Poisson distribution. For large N the Poisson distribution becomes a Gaussian with standard deviation equal to $\sqrt{N}$ and we find a fluctuation in the number of photons $\Delta N_\gamma = \sqrt{N_\gamma}$. This results in a fluctuation of the observed power

$$(\Delta P)_{\rm shot} = \frac{1}{T}\sqrt{N_\gamma}\hbar\omega_{\rm L} = \sqrt{\frac{\hbar\omega_{\rm L}}{T}P} \tag{3.4}$$

where $P = N_\gamma \hbar\omega_{\rm L}/T$.

The strain sensitivity due to shot noise in units of $\mathrm{Hz}^{-1/2}$ is given in Ref. [27]:

$$S_n^{1/2}(f)\Big|_{\rm shot} = \frac{1}{8\mathcal{F}L}\left(\frac{4\pi\hbar\lambda_{\rm L}}{\eta P_{\rm bs}}\right)^{1/2}\sqrt{1+(f/f_p)^2} \tag{3.5}$$

where $\eta = 0.93$ is a typical value of the efficiency of the photodiode and $P_{\rm bs}$ is the power on the beam-splitter after recycling.

We can see that $S_n^{1/2}(f)\Big|_{\rm shot}$ is flat up to the pole frequency and then rises linearly in f. This is due to the combination of the shot noise itself, which is independent of f, with the transfer function which degrades linearly with f after the pole frequency. This result suggests that shot noise can be reduced by increasing the laser power on the beam-splitter $P_{\rm bs}$. However, the radiation pressure of a beam of photons on the reflecting mirrors also fluctuates due to uncertainty in the number of photons arriving at the mirror, generating a force that shakes the mirrors. This force grows as $\sqrt{P_{\rm bs}}$ while the shot noise decreases as $1/\sqrt{P_{\rm bs}}$. The thermal excitations are overcome by averaging over many vibrations since the atomic vibrations are random and incoherent. The ~ 7 cm wide laser beam averages over about 10^{17} atoms and at least 10^{11} vibrations per atom in a typical measurement. The effect is thus suppressed by a factor of $\sim \sqrt{10^{28}}$. It turns out that the atomic vibrations are completely irrelevant compared to the coherent effect of a gravitational wave.

The strain sensitivity due to radiation pressure is also given in Ref. [27]:

$$S_n^{1/2}(f)\Big|_{\rm rad} = \frac{16\sqrt{2}\mathcal{F}}{ML(2\pi f)^2}\sqrt{\frac{\hbar P_{\rm bs}}{2\pi\lambda_{\rm L}c}}\frac{1}{\sqrt{1+(f/f_p)^2}} \tag{3.6}$$

where M is the mass of the mirror and we see that $S_n^{1/2}(f)\Big|_{\rm rad}$ falls off as f^{-2}. For the ground based detectors the low frequency limit in sensitivity is actually set by seismic noise below ~ 75 Hz that overwhelms the radiation pressure. There are also other thermal vibrations that are relevant for the LIGO noise spectrum. For a continued discussion of the sensitivity of the ground based interferometers to gravitational waves see Ref. [27]. The composite sensitivity curve for the Advanced LIGO configuration as a function of frequency can be seen in Figure 3.1.

Advanced engineering designs and implementations have brought the LIGO detectors to their design concept sensitivity. Collaborating with other ground based

gravitational wave detectors in Europe, the sixth science run with the various detectors operating simultaneously will be completed in 2010. The array of detectors is essential for making the marginal detections predicted as possible for the initial design of the LIGO-Virgo network. There are thousands of understood noise sources for detectors fastened to the Earth, including seismic activity and weather. Noise sources are local, while a gravitational wave signal of cosmic origin would produce a predicted pattern of responses in the various detectors of the network and cross correlation of the detector outputs would be able to uncover a weak signal.

Significant upgrades will be made to the LIGO and Virgo detectors to produce the advanced generation of gravitational wave detectors by 2015. Improvements in laser power, seismic isolation, and other systems will result in at least a factor of ten improvement in sensitivity across the frequency band. This will result in sensitivity to signals in a volume of space one thousand times larger than that accessible to the initial detectors. While the astrophysical prediction for the rate of events producing gravitational waves detectable by initial LIGO was small, a significant increase in possible detections is predicted for the advanced detectors ranging from a few detections per year to a few detections per week [28].

3.3.2 The Laser Interferometer Space Antenna

The National Aeronautics and Space Administration (NASA) and the European Space Agency (ESA) have plans to launch a space-based gravitational wave detector known as the Laser Interferometer Space Antenna (LISA) [3, 29]. The concept for LISA places test masses in space and tracks the distances between them to indicate the passage of a gravitational wave. In practice the LISA array will consist of three satellites in an equilateral triangle configuration each housing two proof masses and laser systems to accurately monitor the distances between the proof masses. The

masses will be freely floating within each satellite, protected from external forces such as the solar wind by the satellite housing. The distance between the satellites will have a mean value of five million kilometers (5×10^9 m) and distance changes will be measured to less than the width of an atom ($\sim 10^{-11}$ m). LISA's long arms make it sensitive to a region of the gravitational wave frequency spectrum between roughly 10 μHz and 1 Hz. This range in frequencies will be rich in sources of gravitational waves from tens of thousands of detectable galactic compact binary systems [30] as well as extragalactic sources such as massive binary black hole systems.

The basic LISA configuration will have the center of mass of the constellation in a nearly circular orbit around the Sun, 20° behind the Earth. The plane of the constellation will be tilted 60° with respect to the ecliptic, tumbling in retrograde motion as it orbits the Sun (see Figure 3.2).

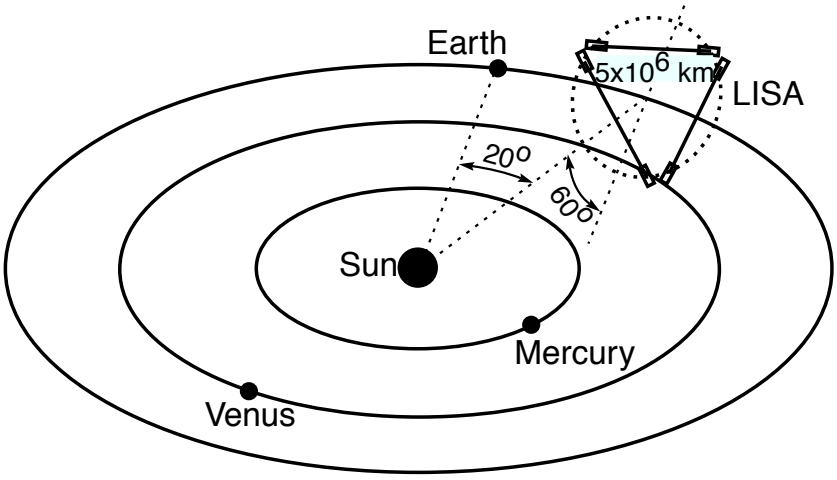

Figure 3.2: The basic LISA configuration as it orbits the Sun [31].

The frequency range where LISA will be sensitive to gravitational waves is determined by the various noise sources and the detector arm length. Similar to the situation for the ground based detectors, there will be shot noise and radiation pres-

sure associated with the lasers. It has been shown that the frequency fluctuations of the lasers and the noise due to the mechanical vibrations of the optical benches would overwhelm gravitational wave signals but that these noise sources can be cancelled by optimal combinations of the six measured phase outputs with appropriate time delays [32, 33]. The formation of these so called Time Delay Interferometry (TDI) channels is described below in Eqn. 3.15 and Eqns. 3.17. The sensitivity of LISA to gravitational wave signals after noise cancellation with TDI is limited at low frequencies by the test-mass acceleration noise, in part due to laser radiation pressure. At mid frequencies the laser shot noise and optical-path measurement errors contribute to sensitivity limits. At high frequencies the gravitational wavelength becomes shorter than the LISA arm length, reducing the efficiency of the interferometric measurement [29]. The composite sensitivity curve for LISA as a function of frequency can be seen in Figure 3.1.

An accurate model for the motion of the LISA spacecraft is essential for determining the response it will have to gravitational wave signals. The time dependent locations of the LISA spacecraft can be written in the solar system barycenter frame. The eccentricity of the LISA orbit around the Sun will be small and it is sufficient to write the Cartesian coordinates of the three spacecraft to second order in the

eccentricity of the orbit,

$$\begin{aligned}
x(t) &= R\cos(\alpha) + \frac{1}{2}e_L R\Big(\cos(2\alpha-\beta) - 3\cos(\beta)\Big) \\
&\quad + \frac{1}{8}e_L^2 R\Big(3\cos(3\alpha-2\beta) - 10\cos(\alpha) \\
&\quad - 5\cos(\alpha-2\beta)\Big) \\
y(t) &= R\sin(\alpha) + \frac{1}{2}e_L R\Big(\sin(2\alpha-\beta) - 3\sin(\beta)\Big) \\
&\quad + \frac{1}{8}e_L^2 R\Big(3\sin(3\alpha-2\beta) - 10\sin(\alpha) \\
&\quad + 5\sin(\alpha-2\beta)\Big) \\
z(t) &= -\sqrt{3}e_L R\cos(\alpha-\beta) \\
&\quad + \sqrt{3}e_L^2 R\Big(\cos^2(\alpha-\beta) + 2\sin^2(\alpha-\beta)\Big)\,. \qquad (3.7)
\end{aligned}$$

Here $R = 1$ AU is the radial distance to the guiding center, e_L is the eccentricity of the LISA orbit, $\alpha = 2\pi f_m t + \kappa$ is the orbital phase of the guiding center, and $\beta = 2\pi n/3 + \lambda$ $(n = 0, 1, 2)$ is the relative phase of the spacecraft within the constellation. The parameters κ and λ give the initial ecliptic longitude and orientation of the constellation.

Using these coordinates the instantaneous separations between spacecraft are given by

$$\begin{aligned}
L_{12}(t) &= L\Bigg(1 + \frac{e_L}{32}\Bigg[15\sin\Big(\alpha-\lambda+\frac{\pi}{6}\Big) \\
&\quad - \cos\Big(3(\alpha-\lambda)\Big)\Bigg]\Bigg) \\
L_{13}(t) &= L\Bigg(1 + \frac{e_L}{32}\Bigg[-15\sin\Big(\alpha-\lambda-\frac{\pi}{6}\Big) \\
&\quad - \cos\Big(3(\alpha-\lambda)\Big)\Bigg]\Bigg) \\
L_{23}(t) &= L\Bigg(1 - \frac{e_L}{32}\Bigg[15\cos(\alpha-\lambda) \\
&\quad + \cos\Big(3(\alpha-\lambda)\Big)\Bigg]\Bigg)\,, \qquad (3.8)
\end{aligned}$$

with $L = 2\sqrt{3}Re$. For the mean LISA arm length of $L = 5 \times 10^9$ m the eccentricity of the spacecraft orbits $e_L = 0.00965$ and the second order effects are one hundred times smaller than the leading order.

The response of the instrument to a passing gravitational wave is encoded in the changing separation between the spacecraft.

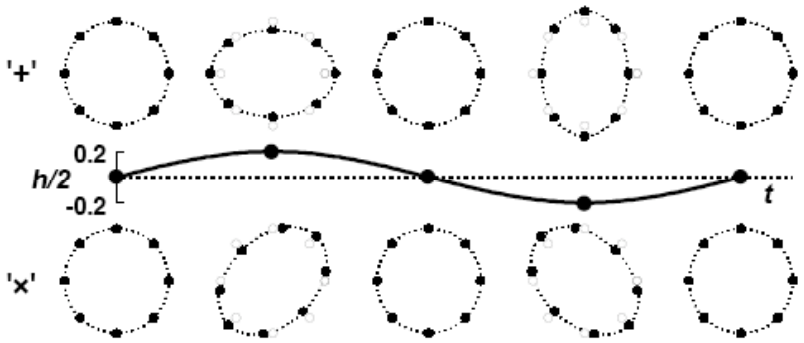

Figure 3.3: The effect of a gravitational wave passing through the plane of the page on a ring of test masses. The top row shows the change in position of the test masses for the + polarization and the bottom row shows the corresponding response to the $\times$ polarization. This cartoon illustrates how distance changes can be used to monitor the passage of a gravitational wave.

An arbitrary gravitational wave signal can be written as a linear combination of two independent polarizations, known as h_+ and $h_\times$. The polarization vectors are perpendicular to the direction of propagation of the gravitational wave, $\hat{\mathbf{k}}$. The effect of a passing gravitational wave on a ring of test masses is illustrated in Figure 3.3. The metric tensor of the gravitational wave at some location $\mathbf{x}$ is written as

$$\mathbf{h}(\xi) = h_+(\xi)\boldsymbol{\epsilon}^+ + h_\times(\xi)\boldsymbol{\epsilon}^\times \tag{3.9}$$

where the wave variable $\xi = t - \hat{\mathbf{k}} \cdot \mathbf{x}$ gives surfaces of constant phase.

The polarization tensors can be expanded in terms of the basis tensors $\mathbf{e}^+$ and $\mathbf{e}^\times$ [34]

$$\begin{aligned} \boldsymbol{\epsilon}^+ &= \cos(2\psi)\mathbf{e}^+ - \sin(2\psi)\mathbf{e}^\times \\ \boldsymbol{\epsilon}^\times &= \sin(2\psi)\mathbf{e}^+ + \cos(2\psi)\mathbf{e}^\times \,, \end{aligned} \tag{3.10}$$

where ψ is the principle polarization angle and the basis tensors $\mathbf{e}^+$ and $\mathbf{e}^\times$ are expressed in terms of two orthogonal unit vectors,

$$\begin{aligned} \mathbf{e}^+ &= \hat{\mathbf{u}} \otimes \hat{\mathbf{u}} - \hat{\mathbf{v}} \otimes \hat{\mathbf{v}} \\ \mathbf{e}^\times &= \hat{\mathbf{u}} \otimes \hat{\mathbf{v}} + \hat{\mathbf{v}} \otimes \hat{\mathbf{u}} \,. \end{aligned} \tag{3.11}$$

These vectors, along with the propagation direction of the gravitational wave $\hat{\mathbf{k}}$, form an orthonormal triad, which may be expressed as a function of the source location on the celestial sphere (θ, ϕ),

$$\begin{aligned} \hat{\mathbf{u}} &= \cos\theta\cos\phi\,\hat{\mathbf{x}} + \cos\theta\sin\phi\,\hat{\mathbf{y}} - \sin\theta\,\hat{\mathbf{z}} \\ \hat{\mathbf{v}} &= \sin\phi\,\hat{\mathbf{x}} - \cos\phi\,\hat{\mathbf{y}} \\ \hat{\mathbf{k}} &= -\sin\theta\cos\phi\,\hat{\mathbf{x}} - \sin\theta\sin\phi\,\hat{\mathbf{y}} - \cos\theta\,\hat{\mathbf{z}} \,. \end{aligned} \tag{3.12}$$

The three arms of the LISA constellation will form three independent interferometers. We can construct the three Michelson signals using each spacecraft as a vertex. The Michelson signal for spacecraft 1 is

$$S_1(t) = \Phi_{12}(t_{21}) + \Phi_{21}(t) - \Phi_{13}(t_{31}) - \Phi_{31}(t) \,, \tag{3.13}$$

where t_{21} and t_{31} are found from

$$\begin{aligned} t_{21} &= t - \ell_{21}(t_{21}) \\ t_{31} &= t - \ell_{31}(t_{31}) \end{aligned} \tag{3.14}$$

where $\ell_{ij}(t_{ij})$ is the length of the arm between spacecraft i and spacecraft j at time t_{ij}.

The Michelson channels can be used in the absence of noise, but the intrinsic fluctuations in the phase of the lasers will be larger than the fluctuations due to gravitational waves. This can be mitigated by combining the different Michelson channels in such a way as to cancel the laser phase noise. The TDI signals are constructed by combining time-delayed Michelson signals in such a way as to reduce the overall laser phase noise down to a level that will not overwhelm the detector's output [33]. For instance the X signal is given by [35]:

$$\begin{aligned} X(t) &= \Phi_{12}(t_{21}) + \Phi_{21}(t) - \Phi_{13}(t_{31}) \\ &\quad -\Phi_{31}(t) - \Phi_{12}(t'_{21}) - \Phi_{21}(t_{13}) \\ &\quad +\Phi_{13}(t'_{31}) + \Phi_{31}(t_{12})\,, \end{aligned} \tag{3.15}$$

where the new times t_{12}, t_{13}, t'_{21}, and t'_{31} are defined through the implicit relationships

$$\begin{aligned} t_{12} &= t_{21} - \ell_{12}(t_{12}) \\ t_{13} &= t_{31} - \ell_{13}(t_{13}) \\ t'_{21} &= t_{13} - \ell_{21}(t'_{21}) \\ t'_{31} &= t_{12} - \ell_{31}(t'_{31})\,. \end{aligned} \tag{3.16}$$

By permutations of the indices similar forms for the Y and Z-signals can be constructed. A noise orthogonal set of TDI variables can be formed as a linear combination of the X-Y-Z signals.

$$\begin{aligned} A &= \frac{2X - Y - Z}{3} \\ E &= \frac{Z - Y}{\sqrt{3}} \\ T &= \frac{X + Y + Z}{3} \end{aligned} \tag{3.17}$$

The instrument response will be given in terms of the TDI variables as the optimal combination of the detector phase output.

The well modeled LISA constellation and its understood noise sources can be combined with expected gravitational wave signals to produce a simulated LISA data stream. Realistic simulated LISA data are necessary for demonstrating the ability of the gravitational wave community to do astrophysics with LISA by extracting signals and source parameters from inherently noisy data.

CHAPTER 4
PARAMETER ESTIMATION

Beyond the first direct detection of a gravitational wave signal, gravitational wave astronomy seeks to contribute to the fields of astrophysics and relativity by making precise measurements of signals from systems unprobed by electromagnetic observations to complement traditional astronomy. The ability of gravitational wave detectors to extract astrophysical information from their data hinges on the advanced data analysis techniques necessary to identify gravitational wave signals and their dependence on the physical source parameters. The challenge lies in the noisy data and large parameter spaces of the expected sources.

A wide range of expected gravitational wave signals can be modeled to build templates to compare to the data. This process is known as template matching and can raise quiet signals above the noise to make detections. For the large parameter spaces of many expected gravitational wave signals stepping along a grid of templates can be too computationally expensive to be used for accurately characterizing a signal. A successful technique for data analysis using template matching that avoids using a grid is the Markov Chain Monte Carlo method.

4.1 Posterior Distribution Function

The goal of a parameter estimation study is to find how accurately we can determine the values of the source parameters for a given signal. For complicated search spaces it is not sufficient to find the parameters that best fit the data and estimate their errors as Gaussian curves about this peak. The surface is often not Gaussian and multi-modal structures are not captured in such an estimate. It is preferable to

determine the true distribution about the best fit values. In the Bayesian framework, this is called the posterior distribution function (PDF), and is calculated by

$$p(\mathbf{x}) \propto \mathcal{L}(\mathbf{x})\Pi(\mathbf{x}) \ . \tag{4.1}$$

Here the physical parameters are contained in the vector $\mathbf{x}$ and the measure of the fit of the template $h(\mathbf{x})$ to the data s is defined as the likelihood

$$\mathcal{L}(\mathbf{x}) = Ce^{-\frac{1}{2}(s-h(\mathbf{x})|s-h(\mathbf{x}))} \ , \tag{4.2}$$

where C is a normalization constant that does not depend on the signal or the template. The noise weighted inner product used in the likelihood calculation is defined as

$$(a|b) = 2\int_0^\infty \frac{a^*(f)b(f) + a(f)b^*(f)}{S_n(f)}\, df \ , \tag{4.3}$$

where $S_n(f)$ is the one-sided noise spectral density.

The factor $\Pi(\mathbf{x})$ in Eqn. 4.1 is known as the prior probability density for $\mathbf{x}$ and reflects our knowledge, however uninformative, about the PDF before analyzing the data. For example, the prior for angular parameters such as sky location keep the parameters in their proper range, $\cos\theta = [-1:1]$ and $\phi = [0:2\pi]$.

The global maximum of the PDF occurs where the template parameters are the best fit to the data, weighted by the prior distribution. The distribution about this location in parameter space gives the uncertainties in the parameters. Sampling the PDF with Markov Chain Monte Carlo techniques provides a practical way to find both best fit parameters and the distribution that reveals the uncertainty in each parameter.

4.2 Markov Chain Monte Carlo Techniques

The Markov Chain Monte Carlo (MCMC) method provides a powerful tool for exploring large parameter spaces without creating a large grid of templates [36, 37]. Instead of stepping along a grid to find the best fit to the data, a template $h(\mathbf{x})$ is generated at some place in parameter space, $\mathbf{x}$, and compared to the data, s. Each of the parameters is then varied by some amount to reach a new place in parameter space, $\mathbf{y}$. The quality of the fit at each location is evaluated as a likelihood calculation (Eq. 4.2) and the Hastings Ratio H is formed to compare the two templates [38]:

$$H = \frac{\Pi(\mathbf{y})\mathcal{L}(\mathbf{y})q(\mathbf{x}|\mathbf{y})}{\Pi(\mathbf{x})\mathcal{L}(\mathbf{x})q(\mathbf{y}|\mathbf{x})} \ . \tag{4.4}$$

The Hastings ratio is built with $\Pi(\mathbf{x})$, the prior distribution for the template parameters, and $q(\mathbf{y}|\mathbf{x})$, the proposal distribution, which is the function that generates proposals for moves from $\mathbf{x}$ to $\mathbf{y}$. Once a jump is proposed, the parameters $\mathbf{y}$ are adopted with probability $\alpha = \min[1, H]$. When $\mathbf{y}$ is a better fit to the data than $\mathbf{x}$, H is greater than 1 and the parameters $\mathbf{y}$ are adopted. If $\mathbf{y}$ is a worse fit to the data, H is less than 1, and there is a probability equal to H that the parameters $\mathbf{y}$ will be adopted. This process is repeated until some convergence criteria are reached.

A properly constructed MCMC search will sample the parameter space with the number of iterations spent at each parameter value proportional to how well that value fits the data. The chain of values for each parameter is used to form histograms that represent the marginalized PDFs that show the resolution and expected error for the parameter.

4.3 Proposal Distributions

An MCMC search is guaranteed to eventually converge on the posterior distribution regardless of choice of proposal distribution. In practice the performance of the algorithm is quite sensitive to the choice of proposal distribution, and care must be taken to ensure that the chains do not get stuck on local maxima of the likelihood surface. We employ several techniques to ensure rapid exploration of the full parameter space including Gaussian proposals, moves that exploit symmetries of the likelihood surface to encourage jumps between local maxima, variable jump sizes, and parallel tempering to encourage wide exploration of the parameter space.

4.3.1 Gaussian Proposals

The Fisher Information Matrix, Γ, can be used to propose a jump to parameter values $\mathbf{y}$ based on the Gaussian approximation to the likelihood at $\mathbf{x}$. These proposals efficiently explore local maxima by calculating the eigenvectors and eigenvalues from the Fisher Matrix to propose appropriate sized jumps along independent eigendirections rather than the correlated coordinate directions.

The elements of the Fisher matrix are given by

$$\Gamma_{ij}(\mathbf{x}) = (h_{,i}|h_{,j}) \tag{4.5}$$

where $h_{,i} = \partial_{x_i} h$.

A Gaussian Fisher proposal distribution is useful for local exploration of a parameter space, but more global proposal distributions are needed to ensure full coverage of the possible parameter values.

4.3.2 Parallel Tempering

Global exploration of the parameter space is enhanced by creating a set of parallel chains with likelihood surfaces at different "temperatures" T such that

$$\mathcal{L}_i(\mathbf{x}) = \mathcal{L}(\mathbf{x})^{1/T_i} \quad . \tag{4.6}$$

Chains that explore surfaces with $T \gg 1$ tend to more frequently accept bigger steps since the contrast between maxima and minima is decreased, and this encourages wider exploration of the parameter space [39, 40, 41]. The chains can exchange parameters according to the Hastings ratio for parallel tempering

$$H_{PT} = \frac{\mathcal{L}_a(\mathbf{x}_b)\mathcal{L}_b(\mathbf{x}_a)}{\mathcal{L}_a(\mathbf{x}_a)\mathcal{L}_b(\mathbf{x}_b)} \quad , \tag{4.7}$$

for chains with temperature T_a and T_b and parameters $\mathbf{x}_a$ and $\mathbf{x}_b$, respectively.

It is usual to implement the parallel tempering method for N_C chains with the T values given by

$$T_i = (\Delta T)^{i-1} \tag{4.8}$$

where

$$\Delta T = (T_{\max})^{\frac{1}{N_C - 1}} \quad . \tag{4.9}$$

Each chain explores its own likelihood surface until an exchange of parameters with a neighboring chain is proposed as a step in the MCMC algorithm. The two chains trade parameter values and continue to explore from their new locations. Ideally, the chain with the highest T value has an effective likelihood surface that is smooth enough such that the chain freely explores the entire range of parameters. The discovery of a favorable location in parameter space is then propagated down to the $T = 1$ chain as adjacent chains continue to exchange parameters. Only the $T = 1$ chain samples the true PDF and is used to produce the parameter histograms.

There are several trade-offs that go into the choice of ΔT and N_C. The signal in each chain has an effective signal-to-noise ratio that can be approximated by

$$\mathrm{SNR}_{\mathrm{eff}} \sim \frac{\mathrm{SNR}}{\sqrt{\mathrm{T}_{\mathrm{max}}}} \, . \tag{4.10}$$

It is ideal to have the hottest chain with $\mathrm{SNR}_{\mathrm{eff}} < 5$ so that it searches a smooth likelihood surface and tends to explore widely [42]. The temperature increment between chains should not be larger than $\Delta T < 2$ to ensure good mixing between chains [41, 43]. The parallel chains need to remain in contact with one another so they are able to exchange parameters. The geometric spacing given in Eqn. 4.8 is designed to create a set of chains that tend to exchange parameters. The choice of ΔT and N_C thus depends on the expected SNR of the signal. For example, to explore a signal with SNR = 30, a good choice of parameters would be $\Delta T = 1.4$ and $N_C = 12$, giving $T_{\mathrm{max}} \approx 40$ and the corresponding $\mathrm{SNR}_{\mathrm{eff}} < 5$. While the cost per iteration of a parallel tempered MCMC algorithm is N_C times larger than a standard MCMC algorithm, the improvement in the mixing, especially between widely separated maxima, ultimately leads to a far more efficient exploration of the posterior.

4.3.3 Variable Jump Size

Among the various useful jump proposals are very simple proposals such as small and large jumps along either the parameter directions or the eigen-directions. The biggest proposed jumps should cover the entire parameter range and are not very likely to be accepted. Very small jumps are likely to be accepted but are not efficient as the only type of proposal since they do not explore widely. It is useful to include some mix of large and small jump proposals in the set of proposal distributions to keep the chain moving.

For parallel tempered chains the size of the jumps can be scaled by the temperature. The hotter chains are more likely to accept larger jumps in their flattened likelihood surface and wide exploration by these hot chains is important for determining the global structure of the search space. Jump proposals are thus scaled by a factor of $\sqrt{T}$.

4.3.4 Symmetry Proposals

While MCMC techniques are general and work for searching arbitrary likelihood surfaces it can be an advantage to understand the search space for a specific problem. Multimodal likelihood surfaces often contain a pattern relating the global maximum to other local maxima. It often speeds up the convergence of an MCMC search to propose jumps that might move the parameters to a new local maximum.

Examples of symmetries in the likelihood surface have been found in gravitational wave data analysis problems such as EMRI sources [44] and bursts from cosmic string cusps [41]. The use of symmetry based proposals has been shown in these cases to produce a thorough exploration of the global structure of the likelihood surface. The example of gravitational wave bursts from cosmic string cusps and their signal symmetries will be discussed in the next chapter. We take advantage of our knowledge of the symmetries for this type of source and use symmetry based proposals in our search.

4.4 Parameter Uncertainties

The use of MCMC techniques in gravitational wave data analysis is well documented as a solution to parameter estimation problems [41, 10, 45]. The result of a well constructed MCMC is a set of samples from the posterior distribution. The

number of samples from a particular region of parameter space is proportional to the posterior weight contained in that region. This feature avoids the need to estimate the error in a parameter as a Gaussian distribution around the maximum likelihood value. The uncertainty in each parameter is given by the distribution produced by the MCMC.

We have found that in combination, the proposal distributions discussed above provide a variety of jump proposals that tend to produce an MCMC that efficiently maps out the desired PDF and provides accurate parameter uncertainties even for very large search spaces. The probability that the source parameters take values in a certain interval is easily calculated from the MCMC output by normalizing the number of iterations spent in that intervals by the total number of iterations in the chain. Two specific examples of this technique will be described in Chapters 5 and 7.

CHAPTER 5

COSMIC STRING CUSPS

5.1 Introduction

Cosmic strings were first predicted to form during symmetry breaking in the very early universe [46]. Strings with $G\mu \sim 10^{-6}$, where μ is the string tension and G is Newton's constant, were studied as possible seeds for structure formation and the source of anisotropies in the cosmic microwave background (CMB) radiation [47]. Observations of the CMB combined with other cosmological data sets imply that $G\mu < 2.3 \times 10^{-7}$, which rules out cosmic strings as the source of structure in the universe [48]. This bound makes field theoretic cosmic strings poor candidates for detection by current gravitational wave observatories, but the next generation of detectors will have increased sensitivity to gravitational waves from field theoretic strings [49].

Interest in detecting gravitational wave signatures from cosmic string networks has recently been revived in the context of cosmic superstrings, which can be produced in a variety of string inspired inflationary models [50, 51, 52, 53, 54, 55, 56, 57]. Cosmic superstrings could potentially be observed via gravitational lensing, pulsar timing, observations of the cosmic microwave background, or from the energy they radiate in the form of gravitational waves [47].

A string network consists of long, horizon sized strings and loops that tend to intersect and reconnect, forming sharp edges known as kinks. Cusps with high Lorentz boosts will also generally form on strings and loops. A cosmic string network will produce a gravitational wave background, as well as bursts of gravitational waves from cusps and kinks that stand out above the background. The strongest bursts

come from cusps, where small portions of the string will be traveling near the speed of light, leading to the emission of a beam of gravitational radiation [58, 59]. Current and future ground based gravitational wave detectors (LIGO-Virgo and Advanced LIGO) and the planned NASA/ESA space based detector (LISA) may be able to detect such signals and determine several properties of the string network [60, 61, 62].

In this chapter we consider how these cusp signals may be detected, and how well the signal parameters may be inferred using data from ground and space based gravitational wave observatories. The broad spectrum nature of the signals raises the possibility of joint detection in space and on the ground, and we investigate how this impacts parameter estimation. Our original paper with these results represents the first time that joint LIGO-Virgo-LISA observations have been considered for any gravitational wave source [41].

The signal parameters that can be measured depend on combinations of the key physical parameters, so observations of individual bursts are not enough to constrain the string model. Ultimately it will be quantities such as the event rate as a function of burst amplitude, and the power spectra of the un-resolved confusion background from more distant bursts and the decay of loops that will provide the strongest model constraints. In this chapter we focus on individual bursts and defer the analysis of what can be learned from a global analysis for future work [62].

It has been pointed out that detecting cosmic strings with a microlensing quasar survey has been essentially ruled out by the low event rates ($\sim 10^{10}$ quasar sources would have to be monitored for a year to expect a few events) and the long lensing periods (20-40 years) that are predicted [63]. Still, loops of cosmic string with tensions in the range $10^{-10} < G\mu < 10^{-6}$ are predicted to produce microlensing of stars in the local group of galaxies [64]. A detection of a cosmic string by a gravitational wave detector could thus be followed by an electromagnetic observation by looking in the

direction determined by the gravitational wave observation for microlensing events. This possibility motivates accurate parameter estimation from the gravitational wave detection to provide well determined sky location and orientation information for the string.

5.2 Gravitational Wave Signature

The gravitational wave signature from a cosmic string cusp is very simple. In the limit that the line of sight to the cusp is coincident with the axis of the emission cone, the waveform is linearly polarized and described by the power law

$$h(t) = 2\pi A|t - t_*|^{1/3} \,. \tag{5.1}$$

Here t_* denotes the time when the observer sees the intensity peak. The equation holds for times near t_* as discussed in [60]. The overall amplitude A is related to the distance to the cusp r, the string tension $G\mu$, and the characteristic length scale of the cusp L as

$$A \sim \frac{G\mu L^{2/3}}{r} \,. \tag{5.2}$$

Since L and r are unknown, a measurement of A does not directly reveal the string tension.

The signal is slightly more complicated for off-axis observations. For small viewing angles α, defined as the angle between the line of sight and the axis of the emission cone, the main effect is to round off the cusp waveform (Eqn. 5.1) such that the power spectrum decays rapidly for frequencies greater than $f_{\max} \sim 2/(\alpha^3 L)$. Once again, the observable quantity $f_{\max}$ does not directly reveal the physical quantity of interest, L, since it also involves the unknown viewing angle α.

The observed gravitational wave signal will also depend on how the waveform is projected onto the detector, which will depend on the sky location (θ, ϕ) and the polarization angle ψ. Thus, the detected signal depends on the parameters $A, t_*, f_{\max}, \theta, \phi, \psi$. These six measurable quantities depend on the two intrinsic source parameters $(G\mu, L)$ and the six extrinsic (observer dependent) quantities $(r, \alpha, t_*, \theta, \phi, \psi)$. Clearly the observation of a single burst is insufficient to uniquely determine the intrinsic source parameters. These can only be determined by considering the full gravitational wave signal from a string network, including the spectrum of the background and the rate distribution of the brighter bursts [62].

5.2.1 Template Generation

Cosmic string cusp templates are easy to generate in the frequency domain as the time dependence of the detector response can be ignored: The effective duration of the burst is set by the lowest frequencies the gravitational wave detector can detect. For LISA this is $f_{min} \sim 10^{-5}$ Hz, and for Advanced LIGO the limit is $f_{min} \sim 10$ Hz, which leads to effective durations of 10^5 seconds and 0.1 seconds respectively. In both cases the duration of the burst is short compared to the time scale over which the antenna pattern varies - a year for LISA and a day for LIGO.

The frequency domain waveform for a burst of gravitational waves from a cosmic string cusp is a power law with an exponential decay beginning at the maximum frequency given by the viewing angle [65].

$$h(f) = \begin{cases} Af^{-\frac{4}{3}} & f < f_{max} \\ Af^{-\frac{4}{3}} e^{1-f/f_{max}} & f > f_{max} \end{cases} \tag{5.3}$$

When convolved with the instrument response and considered relative to the instrumental noise spectrum the effective duration of the bursts is even shorter than

the simple estimates based on the low frequency limit. Figure 5.1 shows that for LISA observations $99.9 + \%$ of the full signal to noise ratio (SNR) is reached for observation times of less than 400 seconds, so the stationary detector approximation is very accurate.

The SNR for a template h is calculated:

$$\mathrm{SNR} = (h|h)^{1/2} \tag{5.4}$$

where the noise weighted inner product for the independent data channels β over some observation time T_{obs} is defined as

$$(a|b) = \frac{2}{T_{obs}} \sum_{\beta} \sum_{f} \frac{a^*_\beta(f) b_\beta(f) + a_\beta(f) b^*_\beta(f)}{S^\beta_n(f)} \tag{5.5}$$

and $S_n(f)$ is the one-sided noise spectral density in each channel.

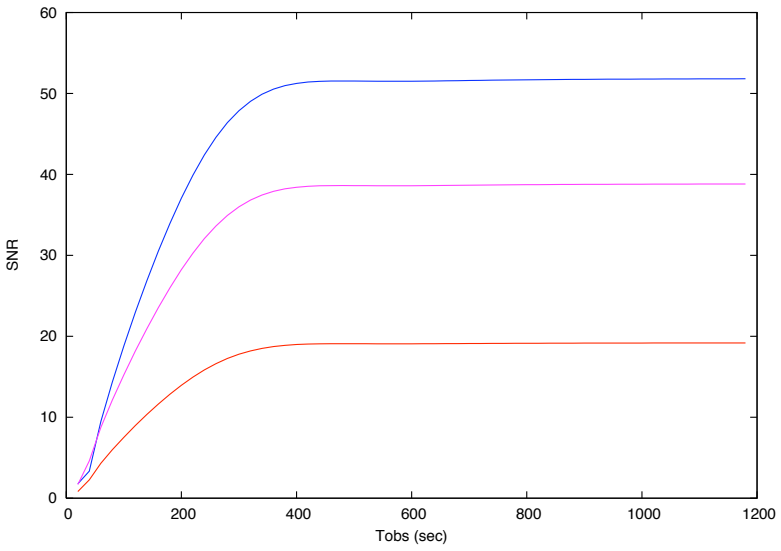

Figure 5.1: The SNR as a function of observation time for three different sets of parameter values for cosmic string cusp bursts of gravitational waves from the MLDC.

5.2.1.1 LISA Instrument Response: To foster the development of LISA data analysis techniques, and to demonstrate mission readiness, a series of Mock LISA Data Challenges has been conducted [6]. The simulated data sets include anticipated sources of instrument noise and a wide range of astrophysical sources. Data analysis techniques can be used to separate the signals from the noise and estimate the parameters of the sources. The MLDC Taskforce has created both training data sets with an answer key for the injected source parameters and blind data sets with a secret answer key. The injected parameter values for the blind data sets are revealed after a set deadline and submissions by data analysis groups are evaluated for accuracy [66]. Challenge 3.4 contains gravitational waveforms for burst signals from cosmic string cusps and we demonstrate the ability of gravitational wave detectors to characterize these sources.

We adopt the standard MLDC ecliptic coordinate system with origin at the barycenter. The individual data streams from the six LISA phase meters can be combined to cancel out the laser phase noise and form Time Delay Interferometry (TDI) variables [33] as described in Chapter 3. The data sets for MLDC Challenge 3.4 included both the phase meter outputs and the complete set of Michelson style TDI variable $\{X, Y, Z\}$. The latter can be used to construct three noise orthogonal data streams that are similar to the $\{A, E, T\}$ variables described in Ref. [67]. Each data stream s contains the response to the gravitational wave signal and additive, stationary, Gaussian distributed instrument noise: $s_\beta = h_\beta + n_\beta$.

The gravitational wave response is computed by convolving $h(\mathbf{x}, f)$ with the static limit of the LISA instrument response [34]. The various time delays in the response

appear as phase shifts that give rise to transfer functions of the form

$$T_{ij}(f) = \frac{1}{2}\mathrm{sinc}[\frac{f}{2f_*}(1-\hat{\mathbf{k}}\cdot\hat{\mathbf{r}}_{\mathbf{ij}})]\exp\{-i[\frac{f}{2f_*}(3+\hat{\mathbf{k}}\cdot\hat{\mathbf{r}}_{\mathbf{ij}})]\} + \frac{1}{2}\mathrm{sinc}[\frac{f}{2f_*}(1+\hat{\mathbf{k}}\cdot\hat{\mathbf{r}}_{\mathbf{ij}})]\exp\{-i[\frac{f}{2f_*}(1+\hat{\mathbf{k}}\cdot\hat{\mathbf{r}}_{\mathbf{ij}})]\}$$

where $\hat{\mathbf{k}}$ is the propagation direction of the gravitational wave, $\hat{\mathbf{r}}_{\mathbf{ij}}$ is the unit vector pointing from spacecraft i to spacecraft j, and $f_* = 1/(2\pi L)$ is the LISA transfer frequency for arm length L. The transfer function has zeros at frequencies that depend on the propagation direction. This gives LISA angular resolution for burst sources since bursts from different sky locations (θ, ϕ) will project differently onto the detector.

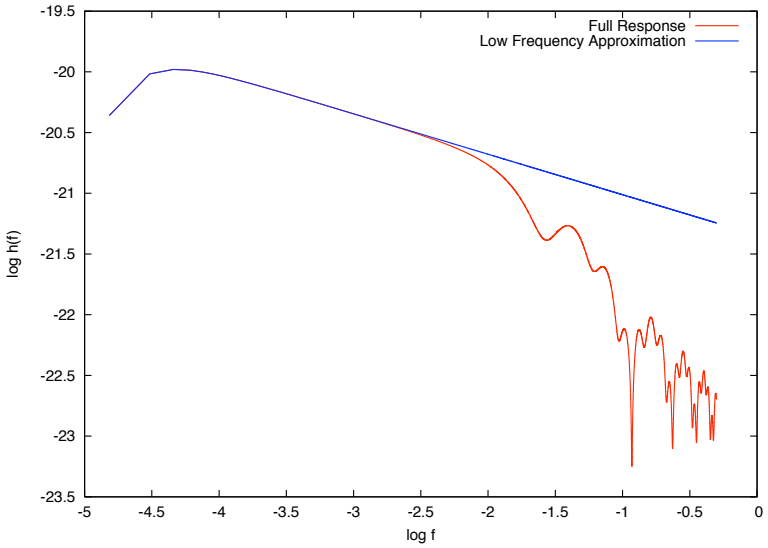

Figure 5.2: The low frequency approximation to the LISA response compared to the full response for the same source.

It is the high frequency component of the gravitational wave signal (Eqn. 5.3) from a cosmic string cusp that determines the resolution of the source on the sky. Cusps seen with large viewing angles result in signals with frequency cut-offs below

the transfer frequency, and as a result, little or no sky resolution. Figure 5.2 shows the LISA instrument response in the low frequency limit compared to the full LISA response to the same source. The specific locations of the minima of the full response depend on the sky location of the source and angular resolution is achieved because templates with different sky locations have different response shapes. The time domain LISA response to two of the MLDC training data sources in the A, E, and T channels can be seen in Figures 5.3 and 5.4. The high frequency components are absent in Figure 5.3 and clearly visible in Figure 5.4.

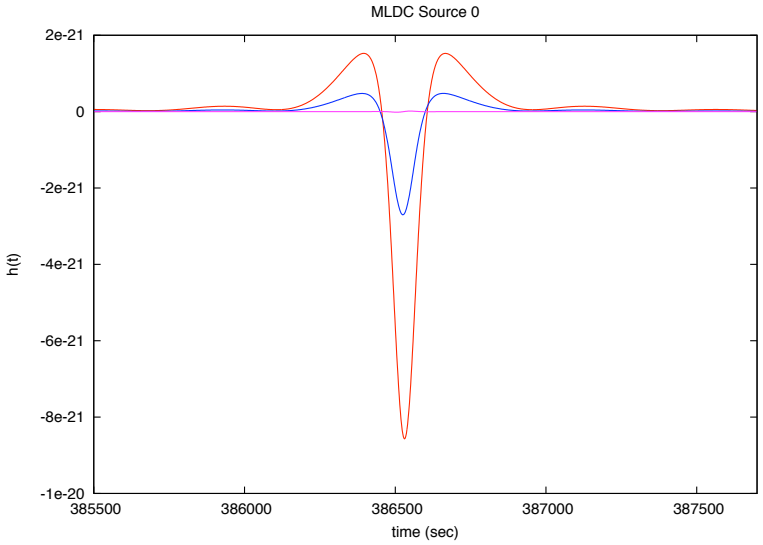

Figure 5.3: The time domain A, E, and T channel responses to Mock LISA Data Challenge 3.4 training source 0 with $f_{max} = 2.36 \times 10^{-3}$ Hz.

5.2.1.2 LIGO-Virgo Instrument Response: The individual LIGO and Virgo instrument responses are similar to the low frequency limit of the LISA response,

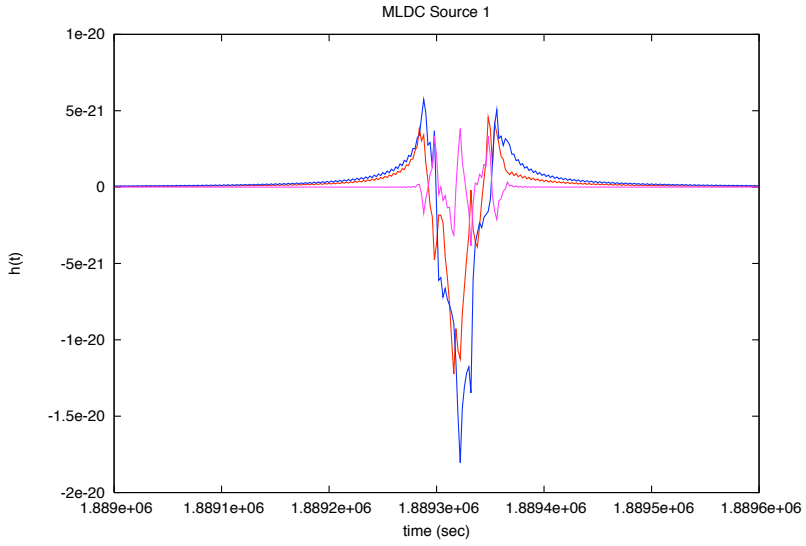

Figure 5.4: The time domain A, E, and T channel responses to Mock LISA Data Challenge 3.4 training source 1 with $f_{max} = 1.15$ Hz.

save for a factor of $\sqrt{3}$ because of the equilateral triangle configuration of LISA as opposed to the 90° orientation of the ground based detector arms.

The orientation and location of each detector is most easily defined in an Earth fixed coordinate system with origin at the geocenter [68]. The Earth can be considered stationary for the short duration that the cusp signal is in the LIGO-Virgo band. This allows us to generate the waveform templates in the frequency domain with the different times of arrival at each detector appearing as relative phase shifts in the signal.

During the epoch of joint LISA-LIGO-Virgo observations the ground based detectors are expected to be operating in advanced configurations, so the baseline Advanced LIGO wideband noise curve was used for the terrestrial network in our joint detection studies.

5.3 MCMC Techniques

5.3.1 Markov Chain Monte Carlo

The Markov Chain Monte Carlo search method provides a powerful tool for searching large parameter spaces without creating a large grid of templates [36, 37]. For studying bursts of gravitational waves from cosmic string cusps the signal was parameterized by $\mathbf{x} \rightarrow \{\ln A, t_*, \ln f_{\max}, \theta, \phi, \psi\}$, and the priors were taken to be uniform in these quantities, save for θ, where a uniform sky distribution is given by $\Pi(\theta) = \frac{1}{2}\sin(\theta)$.

5.3.2 Proposal Distributions

As discussed in Chapter 4, an MCMC search is guaranteed to eventually converge on the posterior distribution regardless of choice of proposal distribution. In practice the performance of the algorithm is quite sensitive to the choice of proposal distribution, and care must be taken to ensure that the chains do not get stuck on local maxima of the PDF. We employed several techniques to ensure rapid exploration of the full parameter space: local coordinate transformations to uncouple the parameters; moves that exploit symmetries of the likelihood surface to encourage jumps between local maxima; and parallel tempering to encourage wide exploration of the posterior.

5.3.2.1 Detector Symmetry Based Proposals: Understanding the symmetries associated with the detection of bursts provides another effective proposal distribution. Any burst short enough to treat the LISA detector as stationary will have a degeneracy such that sky locations related by a reflection in the plane of the detector will produce an *identical* response. There are additional symmetries in the low

frequency limit that result from 120° rotations in the plane of the detector. These symmetries are broken at higher frequencies by the slightly different arrival times of the gravitational waves across the LISA array. Rotations thus produce two sets of secondary maxima (Figure 5.5).

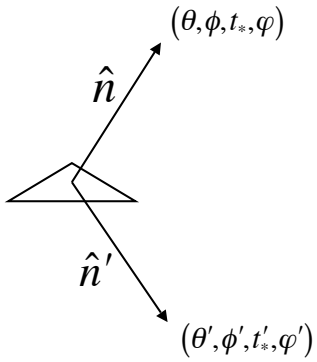

Figure 5.5: Reflection in the plane of the detector gives a degenerate set of parameter values. Rotations in the plane of the detector give two sets of secondary maxima.

The MCMC searches for cosmic string cusps include proposal jumps from $\mathbf{x}$ to the set of parameters $\mathbf{y}$ that give the degenerate detector response. The mapping between these sets of parameters involves the sky location, polarization angle, and the time of arrival at the solar barycenter. The symmetry reflection and rotations are included as possible jumps, but the rotations are rarely accepted unless the chain happens to be at a secondary maximum and the rotation takes the chain to one of the two primary maxima.

Our Fisher matrix prediction uses the LISA symmetry and calculates the approximation to the response at the two degenerate sky locations. While the likelihood is identical at the two locations in parameter space, the curvature of the likelihood surface is different. The Fisher matrix is useful for driving jumps in the MCMC searches, but it is not a perfect prediction of the PDF for the source. The maps shown in Figures 5.6 and 5.7 compare the marginalized PDFs for the sky location

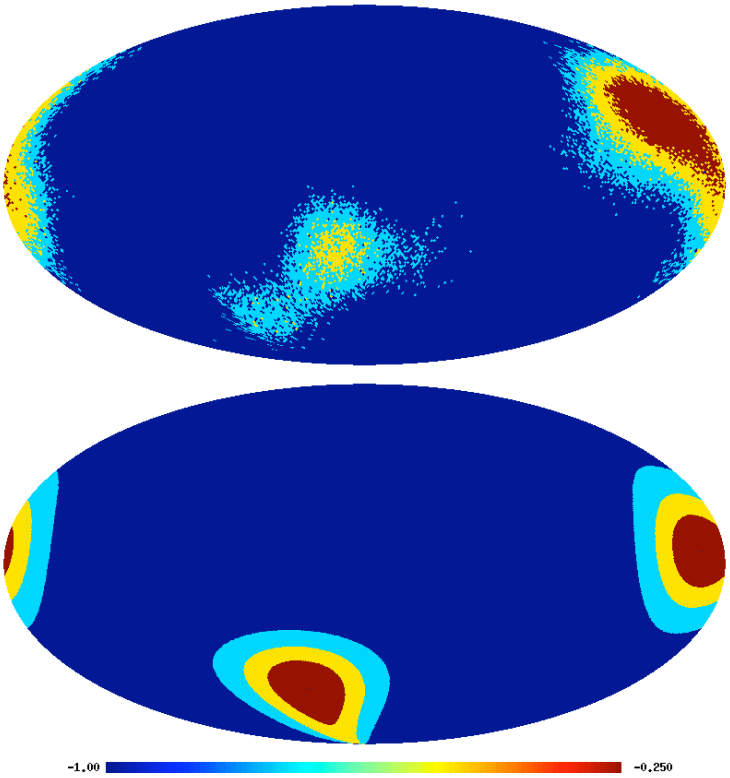

Figure 5.6: A sky location histogram of a Parallel Tempered MCMC search for Mock LISA Data Challenge 3.4 source 2 (MLDC source 3.4.2) on the full sky with quartile contours and a Fisher matrix approximation for the source location below for comparison (marginalized over the other source parameters). The all-sky figures use the HEALPix pixelization of the sky (http://healpix.jpl.nasa.gov).

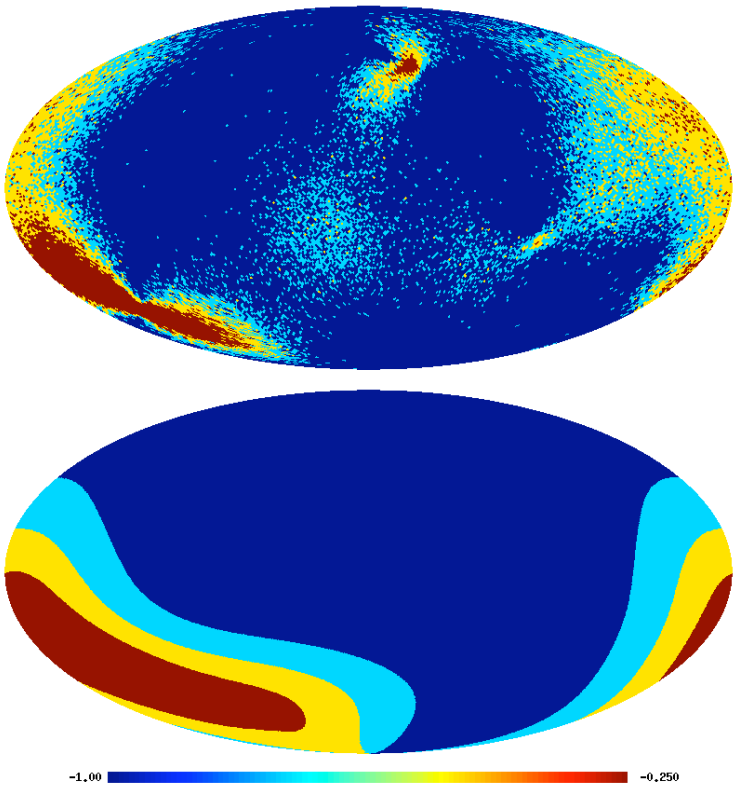

Figure 5.7: A sky location histogram of a Parallel Tempered MCMC search for Mock LISA Data Challenge 3.4 source 4 (MLDC source 3.4.4) on the full sky with quartile contours and a Fisher matrix approximation for the source location below for comparison (marginalized over the other source parameters).

derived from the Fisher matrix approximation and from Markov Chain Monte Carlo explorations of two bursts in the Mock LISA Data Challenge 3.4 training data.

We compared MCMC runs with and without the symmetry based jumps, and while parallel tempering did allow the chains to transition between the various maxima, the mixing was greatly enhanced by including the symmetry based jumps. A chain with such symmetry jumps moves freely between the two degenerate locations in parameter space, exploring both peaks and producing bimodal histograms for each source parameter.

The use of a variety of proposal distributions is essential for an efficient search of the parameter space. In the case of cosmic string cusp gravitational wave sources the symmetry considerations are especially important to avoid getting stuck on a single maximum. The detection of a cosmic string cusp by LISA must include the two degenerate answers, with the possibility of the degeneracy being broken by a simultaneous detection by the ground based gravitational wave detector network.

5.4 Mock LISA Data Challenges (MLDC)

Challenge 3.4 contains gravitational waveforms for burst signals from cosmic string cusps, comprised of a month long data set (2^{21} samples with 1 second sampling) with cosmic string cusp waveforms injected with a Poisson event rate of five events per month. The training data set includes an answer key with the number of injected sources and their parameter values. The training data happens to contain five sources, but the Poisson distribution of events means there is a good chance that the blind data could have between two and eight sources. The MLDC sources have SNR uniformly distributed in [10, 100] and $\log(f_{\max}/\mathrm{Hz})$ uniformly distributed in [-3,1]. This is also the first MLDC data set with non-symmetric instrument noise. The cusp burst

sources can be found using a symmetric approximation for the noise (leading to a small systematic bias in the recovered parameters), or the source parameters and the individual noise levels can be fitted simultaneously in the search. The time of arrival at the solar system barycenter (t_*) is highly correlated with the sky location of the source. A search for t_* leads to poor determination of the time of arrival of the burst due to the inherently poor resolution of the sky location. A better choice of variable is the time of arrival at the guiding center of the LISA constellation ($t_\triangle$). The detector time of arrival is not as correlated with the sky location parameters, resulting in better conditioned Fisher Information Matrices to drive the local jumps of the Markov Chain.

5.4.1 Training Data Results

The training data were analyzed without reference to the answer key so as to mimic the steps that will be taken to analyze the blind challenge data. The parallel tempering technique takes care of both detection and characterization, so the analysis does not have to be be broken up into distinct stages. On the other hand, running the search on the full $\sim 2 \times 10^6$ seconds of data to find signals with duration $\sim 10^3$ seconds is not very efficient, so we adopted the strategy of dividing the full data set into 64 segments of length 32,768 seconds. Time domain filters were used to limit spectral leakage, and the finite response of these filters meant that signals in the first and last $\sim 10\%$ of each segment had to be discarded. To ensure full coverage, a second pass was performed using segments offset from the first by $16,384$ seconds.

The basic parallel tempered MCMC algorithm was able to both detect and characterize the cosmic string cusp signals in each segment. The "burn-in" time for the chains to lock onto the signals was shortened by several orders of magnitude by analytically maximizing over the time of arrival at the detector center and the amplitude.

These maximizations render the chains non-Markovian, and must be turned off after the burn-in is complete, and the samples from the burn-in must be discarded.

A fully-fledged Bayesian MCMC analysis of the data would involve conditions to decide when the burn-in phase was complete, the ability to search for multiple cusp signals simultaneously, and evidence based selection of the putative detections. While parallel tempered MCMC algorithms can do all of these things, we settled on a less sophisticated approach that could be implemented with less effort. The first stage of the analysis was to search each data segment using $N_C = 12$ chains with $\Delta T = 1.55$ and $N = 10,000$ iterations. A simple SNR threshold was used to decide if a source had been found in the data segment. Triggers with SNR $= (s|h)^{1/2} > 8$ were recorded for further analysis (the loudest noise triggers had SNR < 6). If a trigger was found the signal was regressed from the data and the search repeated (in other words the search is sequential rather than simultaneous).

The initial search did not fit for instrument noise levels, but found all five signals in the training data and recovered the source parameters to good accuracy (Table 5.4.1). Since the segmented data are searched twice, we expect to find each source twice, but one trigger happened to fall near the boundary between segments and was thus discarded. The source was found on the offset pass.

The initial detection of the burst could be done at similar cost using the template grid approach used to search for cosmic string bursts in LIGO data [60]. The main value of the MCMC approach is that it allows us to construct the joint posterior distribution function during the parameter estimation stage of the analysis.

5.4.2 Blind Data Results

The same methods employed in the search for cosmic string signals in the training MLDC data were used to find the signals in the blind data. Three sources were found

Table 5.1: The triggers produced by a search of the MLDC 3.4 training data. All but one of the sources was detected in both passes through the data (one signal happened to straddle a data segment boundary). The injected $f_{\max}$ values are listed, along with the recovered values for SNR. The difference between the injected and recovered parameter values for f_{max} and $t_{\triangle}$ are given in the last two columns. Note that sources with $f_{\max} > f_*$ have large Δf's. These parameter errors are from the first stage of the filtering - the fit improves after the second stage.

Source	$f_{\max}$ (Hz)	SNR	Δf (Hz)	Δt (sec)
3.4.0	2.36e-3	53.54	3.98e-5	4.64
		53.99	7.70e-5	5.42
3.4.1	1.15	21.46	1.11	2.54
		21.27	2.62	2.94
3.4.2	0.46	31.07	0.329	0.15
3.4.3	1.15e-2	73.87	3.82e-4	1.16
		76.58	9.11e-4	0.38
3.4.4	2.27	14.07	2.25	3.44
		14.12	4.14	2.45

in the month long data set. The triggers are listed in Table 5.2 and the recovered best fit parameters are listed in Table 5.3. The evaluation of the recovered template can be found in Table 5.4 with comparable ρ and SNR values indicating a good match to the data.

Table 5.2: The triggers produced by a search of the MLDC 3.4 blind data with the time of each trigger and the recovered SNR. One source was found on only one pass through the data since it straddled the segment boundary.

	SNR1	t_* (sec)	SNR2	t_* (sec)
Source 0	40.461692	599202.3	40.764385	599242.1
Source 1	33.094462	1072929	33.071948	1072929
Source 2	43.264396	1603018		

Table 5.5 shows the parameter estimation errors, SNRs, and individual TDI-channel fitting factors (FF_A and FF_E) for the blind challenge sources. The recovered SNR was computed by filtering the noisy data with the appropriate template, while

Table 5.3: The recovered best fit parameters for the MLDC blind search.

	θ (rad)	ϕ (rad)	ψ (rad)	A	t_* (sec)	$f_{\max}$
Source 0	0.3094	3.926	4.552	9.912e-22	599287.64	Nyquist
Source 1	-0.3233	3.934	4.957	2.763e-21	1072739.28	1.056e-3
Source 2	-0.2325	5.899	5.919	1.512e-21	1602943.85	Nyquist

Table 5.4: The MLDC blind data best fit parameters recovered from the search produce waveforms that can be compared with the data to test how well each source was recovered.

MLDC source 0	SNR	ρ	Correlation
With Noise	40.34	42.09	0.748116

MLDC source 1	SNR	ρ	Correlation
With Noise	20.16	19.62	0.815867

MLDC source 2	SNR	ρ	Correlation
With Noise	42.71	42.80	0.679256

the fitting factors were computed between noiseless signals. Although the accuracy of parameters is poor, when computing the overlap between a template with the recovered parameters and a template with the injected parameters, we find that the fitting factors are very high. This suggests that these results are not due to shortcomings in the search methods, but rather to the character of the waveforms. For relatively short signals such as these bursts, LISA can be considered a static detector, and its response is not imprinted with any modulations from the LISA orbit or from the rotation of the constellation. The sky position of burst sources can then only be determined by triangulation between the spacecraft. This is a weaker effect than determining sky location with a time dependent LISA, and triangulation effects vanish in the limit of long wavelengths.

The determination of sky position is intrinsically harder for burst sources, and it is further complicated by the presence of degeneracies such as the reflection of sky position across the instantaneous LISA plane. The time of arrival at the solar system barycenter t_* and the signal polarization are strongly coupled with sky position, and therefore are also determined poorly. To compensate for this fact, the task force calculate the error in the arrival time of the burst at the center of the detector constellation t_Δ. This parameter has a weaker correlation with the sky position and is constrained better by observations.

5.4.3 Parameter Estimation

An MCMC search for a signal in noisy data returns the PDF that maps out the uncertainty in each parameter as discussed in Chapter 4. This can be compared to the Gaussian approximation for the variance in each parameter derived from the Fisher Information Matrix. To study the parameter estimation abilities of gravitational wave detectors for cosmic string cusps, the five distinct triggers from the search phase of the

Table 5.5: Select parameter errors, SNRs, and fitting factors from the MLDC task force evaluation of the MLDC 3.4 entries [**?**]. There were three injected sources and we recovered all three. Here Δsky is the geodesic angular distance between the recovered and true sky positions; t_Δ is the time of burst arrival at LISA; ψ and $\mathcal{A}$ are the gravitational wave polarization and amplitude.

	Δsky (deg)	Δt_Δ (sec)	$\Delta\psi$ (rad)	$\Delta\mathcal{A}/\mathcal{A}$	SNR	FF$_A$	FF$_E$
Source 0	106.6	2.071	2.600	0.745	43.287	0.99975	0.99565
Source 1	53.1	3.223	0.158	0.011	33.696	0.99926	0.99978
Source 2	137.9	0.980	0.110	0.161	41.418	0.99327	0.99948

training data were used as starting points for MCMC runs. Data segments of length $16,384$ seconds, centered on the time of arrival of the burst, were used in the second stage of the analysis. The parallel tempering routine used $N_C = 12$ chains with a maximum temperature of $T_{\max} = 125$, spacing $\Delta T = 1.55$, and $N = 10^6$ iterations. Histograms for the six source parameters for MLDC training source 3.4.3 are shown in Figure 5.8. The sky location parameters θ and ϕ have a bimodal distribution due to the degeneracy of two sky locations from the detector symmetry. The time of arrival of the signal at the detector is very well determined, matching a Gaussian distribution with a variance of less than one second. The maximum frequency cutoff can also be well determined for sources such as this with $f_{\max}$ below the LISA transfer frequency.

Although not much SNR is gained in the high frequency portion of the signal, the LISA transfer function is essential for determining the direction to the source. This is illustrated quite well by training data source 3.4.3 with SNR = 77 and $f_{\max} = 0.0115$ Hz. Even this source with high SNR has poor angular resolution (Figure 5.9). A new search for a source with identical parameters, and almost identical SNR, but with $f_{\max} = 1.15$ Hz reveals the importance of the high frequency component of the signal (Figure 5.10).

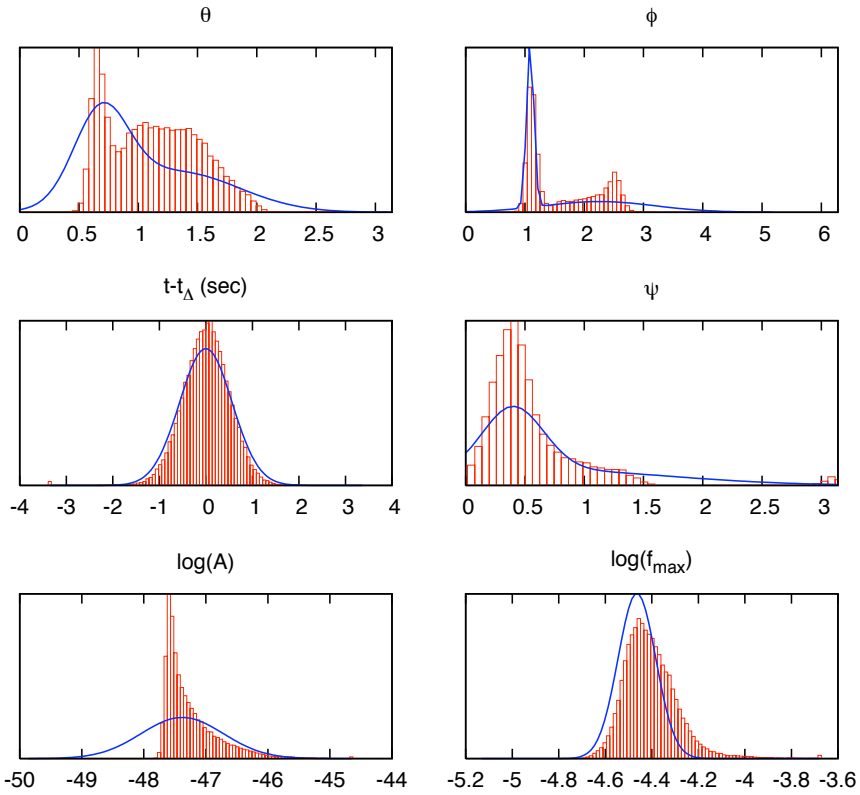

Figure 5.8: The distribution of recovered parameter values for an MCMC search for MLDC training source 3.4.3 using simulated LISA data. The Fisher Matrix Gaussian approximation is shown in blue for comparison.

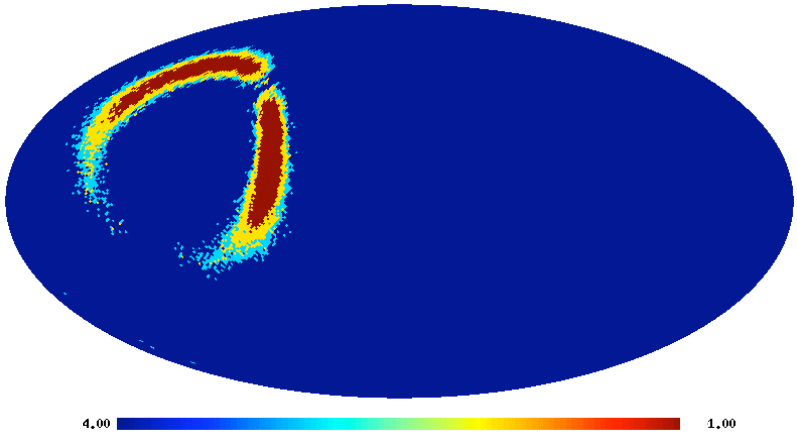

Figure 5.9: An MCMC search for an MLDC training data source with high SNR but a maximum frequency cutoff below the LISA transfer frequency.

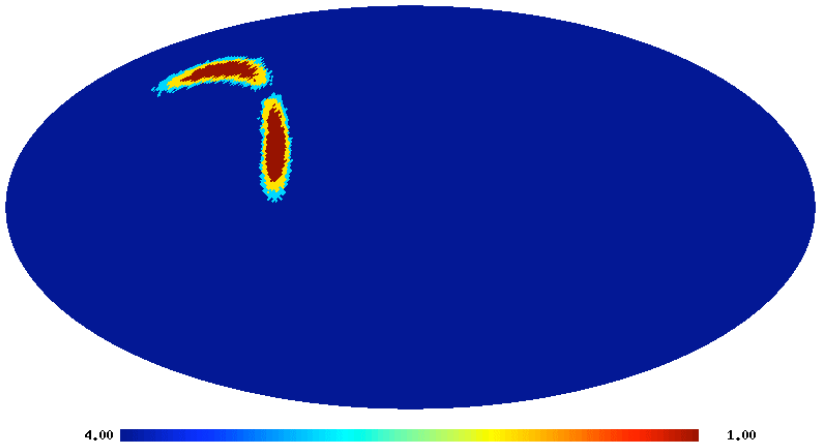

Figure 5.10: An MCMC search for a source with the same parameter values as Figure 5.9, except for a maximum frequency above the LISA transfer frequency.

5.5 Advanced Ground Based Detectors

The wide frequency range of gravitational wave signals from cosmic string cusps allows them to be detected simultaneously by space based and ground based gravitational wave detectors. The current ground based detectors have not yet reported a detection of a gravitational wave signal, but the next generation of detectors, such as Advanced LIGO, will have increased sensitivity to gravitational waves, including bursts from cosmic string cusps. We investigated the performance of the advanced terrestrial network by using the MLDC training source parameters, with the exception of the $f_{\max}$ parameter, which we set at 500 Hz to ensure that the signal will be in the LIGO-Virgo band. The value of $f_{\max}$ is related to the viewing angle α, defined as the angle between the line of sight and the axis of the emission cone. The main effect of off-axis observation is a rounding of the cusp waveform (Eqn. 5.1) such that the power spectrum decays rapidly for frequencies greater than $f_{\max} \sim 2/(\alpha^3 L)$.

The relative orientation of the ground and space based detectors was fixed by setting the start of the LISA observations to the autumnal equinox in the year 2020. When just considering the ground based network we use right ascension α and declination δ to describe the sky location, and the polarization basis defined in Ref. [68]. The time of arrival of the bursts is referenced to the Earth geocenter. We use the reference Advanced LIGO wideband noise curve with strain spectral density

$$S_n(f) = 10^{-49}\left(x^{-4.14} - \frac{5}{x^2} + 111\left(\frac{2 - 2x^2 + x^4}{2 + x^2}\right)\right), \tag{5.6}$$

where $x = f/215\,\mathrm{Hz}$.

The ground based detector network of the 4 km LIGO detectors in Hanford, WA and Livingston, LA and the Virgo detector in Italy, if operating at Advanced LIGO design sensitivity should respond to the MLDC sources with network SNRs of 24.3, 7.9, 4.3, 35.8, and 5.7 for sources 3.4.0 $\rightarrow$ 3.4.4, respectively. Without the benefit of joint LISA observations, sources 3.4.2 and 3.4.4 may not be bright enough to be detected. Simulated data were generated for the LIGO-Virgo network and single chain MCMC runs of 10^6 iterations were used to produced the parameter histograms shown in Figures 5.11 and 5.12, corresponding to MLDC training source 3.4.0 and 3.4.3 respectively. The Fisher Matrix estimates for the parameter distributions are also shown, and are seen to agree well with the MCMC derived PDFs. The f_{max} parameter is poorly determined, resulting in a wide spread of f_{max} values visited by the MCMC chains. The sky location of the burst is determined to an accuracy of ~ 10 square degrees.

5.5.1 Combining Space andGround Based Detectors

The broad spectrum nature of signals from cosmic string cusps allows for joint observations between a space based detector such as LISA and the network of ground

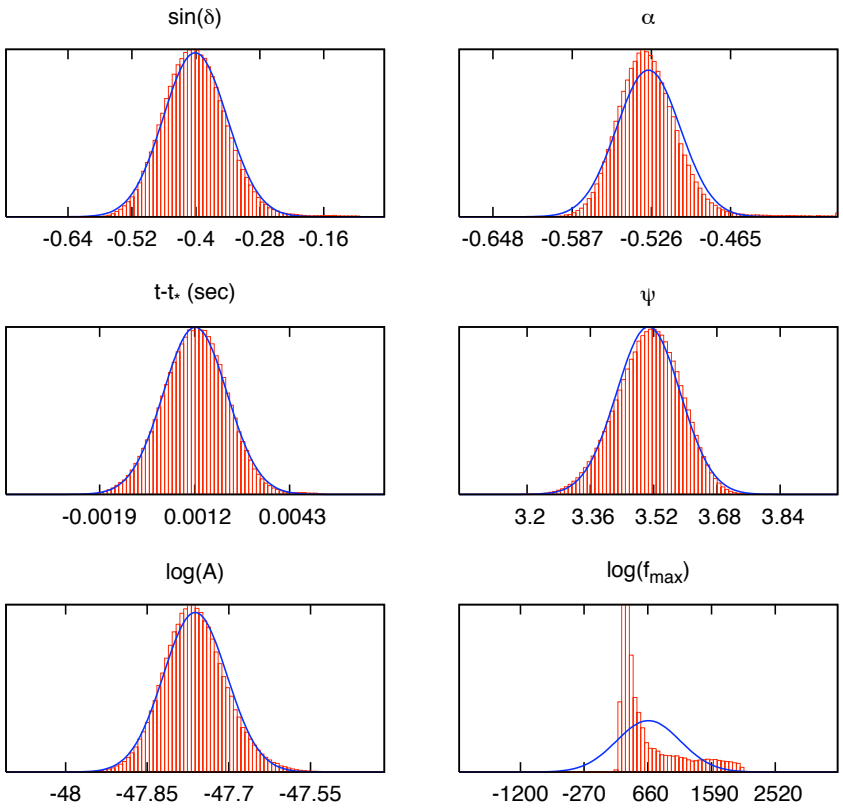

Figure 5.11: The distribution of parameter values for an MCMC search of simulated data using the parameters for MLDC training source 3.4.0 (with $f_{\max}$ boosted to 500 Hz) for the advanced ground based detector network. The Gaussian Fisher Matrix approximation is included in blue for comparison.

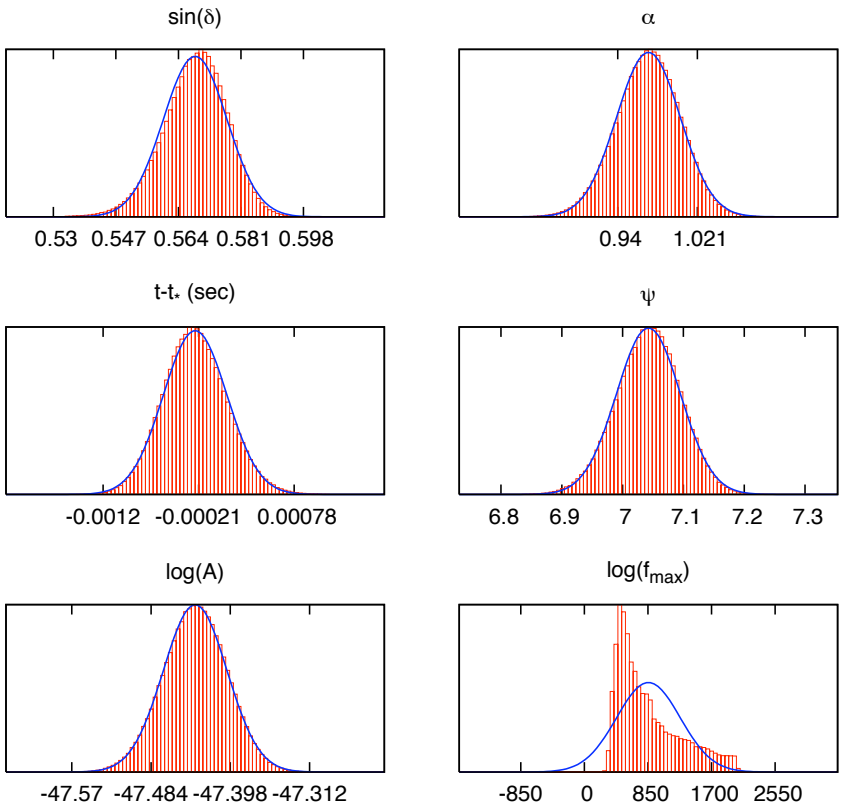

Figure 5.12: The distribution of parameter values for an MCMC search of simulated data using the parameters for MLDC training source 3.4.3 (with $f_{\max}$ boosted to 500 Hz) for the advanced ground based detector network. The Gaussian Fisher Matrix approximation is included in blue for comparison.

based detectors. The LISA sensitivity range is from about 10^{-5} Hz to 1 Hz while LIGO is sensitive in the range 10 Hz to 10 kHz. A burst from a cosmic string cusp with a cut-off frequency above ~ 50 Hz would produce a response across the LIGO-Virgo-LISA network, and the extra information from joint detection would improve estimates of the source parameters. One might expect that the large Earth-LISA baseline (up to 170 seconds delay) would result in extraordinary angular resolution, but the relatively poor determination of the time of arrival at the LISA guiding center (of order 1 second) diminishes the effect.

For joint observations we adopted the Barycentric ecliptic coordinate system used to describe LISA observations. For the time of arrival of the burst we used the geocenter time of arrival ($t_{\oplus}$), as this choice gives the smallest correlation with the sky location uncertainty.

Table 5.6 shows the parameter estimation improvement gained by combining LISA with a ground based network detection. The gains in sensitivity can mostly be attributed to the higher SNR. This can be understood by looking at the off-diagonal components of the Fisher Information Matrix, and noting that even without the LISA contribution the parameter correlations are already quite small. On the other hand, the addition of the LISA data reduces the sky location uncertainty to less than a square degree, which improves the prospects of performing a microlensing follow-up.

5.6 Conclusions

A matched filter analysis using parallel tempered Markov Chain Monte Carlo techniques can both detect and characterize the gravitational wave signals from cosmic string cusps in simulated LISA and LIGO-Virgo data. Some cosmic string cusp waveforms have a broad enough frequency range that they can be detected jointly by

Table 5.6: A joint detection by LISA and an advanced ground based network results in improvements in parameter estimation as shown for three sources from the MLDC 3.4 training data. The Gaussian standard deviation σ is given for the sky location parameters θ and ϕ and the time of arrival t.

MLDC 3.4.0	SNR	σ_θ (rad)	σ_ϕ (rad)	σ_t (sec)
LIGO-Virgo	24.3	5.7e-02	3.8e-02	1.2e-03
LISA + LIGO-Virgo	76.2	2.5e-02	9.6e-03	5.1e-04

MLDC 3.4.1	SNR	σ_θ (rad)	σ_ϕ (rad)	σ_t (sec)
LIGO-Virgo	7.9	1.0e-02	6.9e-02	4.5e-04
LISA + LIGO-Virgo	22.9	4.7e-03	4.8e-02	2.4e-04

MLDC 3.4.3	SNR	σ_θ (rad)	σ_ϕ (rad)	σ_t (sec)
LIGO-Virgo	35.8	1.7e-02	2.4e-02	3.5e-04
LISA + LIGO-Virgo	84.8	5.3e-03	2.4e-03	5.9e-05

space and ground based detectors, and these joint detections significantly improve the angular resolution over what can be achieved by LISA alone. The addition of LISA observations to the ground based network leads to a more modest improvement that may improve the prospects of finding electromagnetic counterparts from microlensing of stars in foreground galaxies.

The analysis presented here can be improved in several ways. Rather than performing the search with the SNR of the best fit template being used as a frequentist detection statistic, the Bayesian evidence for the signal can be computed by thermodynamic integration across the parallel chains [69]. The instrument noise levels must be treated as search parameters when computing the evidence, and the noise model should take into account the non-symmetric noise levels found in the Challenge 3.4 data. The signal model can be extended to account for multiple overlapping bursts, which would be an improvement on the sequential regression used in the current anal-

ysis. A more realistic analysis should also take into account the confusion background that would accompany the bright burst signals.

CHAPTER 6
BINARY BLACK HOLE FORMATION

A promising source of gravitational waves are compact binary objects, including systems of black holes orbiting one another. Observations have shown that today there are massive black holes in the center of nearly all galaxies [70, 71, 72]. Galaxy mergers are also a common process, as evidenced by observations of galaxies in various stages of merger. Various three-body interactions and gas driven processes cause the black holes at the centers of the individual galaxies to sink toward the center of the merged galaxy and begin orbiting one another [13]. Gravitational radiation eventually takes over as the dominant mechanism driving the evolution of the system. The history of galaxy evolution in the universe will be illuminated by the study of massive black hole mergers with precise measurements of the source parameters including masses, spins, orbital eccentricity, and luminosity distances. If black hole mergers are efficient and there is roughly one binary black hole merger for every galaxy merger, then the rate at which LISA measures these events could be several per year [73].

6.1 Observational Evidence for Massive Black Holes

There is strong observational evidence for the existence of astrophysical black holes [72]. Our own Milky Way galaxy hosts a central massive black hole as evidenced by observations of stellar proper motion around a dark object of mass $M \simeq (3.7 \pm 0.2) \times 10^6\ M_\odot$ [74, 75, 76, 77] and size smaller than about one astronomical unit [78], consistent with the identification of the object as a black hole.

There is also strong observational evidence for the presence of massive black holes in the bulges of nearly all local, massive galaxies [70, 71]. These black holes have

masses in the range $M \sim 10^5 - 10^9\ M_\odot$, approximately proportional to the mass of the host galaxies, $M \sim 10^{-3}\ M_{\rm galaxy}$ [79]. There is a nearly linear relation between the mass of a massive black hole and the mass of the galactic bulge hosting the black hole [80, 81]. The black hole mass is also tightly correlated with other properties of the galactic bulge, such as the central stellar velocity dispersion σ (the M-σ relation) [82]. These observations suggest that the central black holes are linked to the evolution of galactic structure in the universe.

Details of the formation process of massive black holes are not well known. A major source of uncertainty in predicting the evolution of massive black holes comes from the unknown fraction of galaxies containing a massive black hole (the occupation number) at high redshifts. Early seed massive black holes can grow both through gas accretion and through coalescence with other seed black holes. Improvements in numerical simulations and electro-magnetic observations will continue to constrain formation scenarios, but it will be gravitational wave observations of black hole mergers at high redshift by LISA that will be able to discriminate between formation mechanisms [83].

6.2 Binary Systems of Massive Black Holes

Galaxies tend to grow through the galaxy merger process. As galaxies with central black holes merge, the black holes tend to form a bound system in the merged galaxy [12]. Understanding the details of the formation of massive black hole binary systems during galaxy mergers turns out to be a challenging problem in theoretical astrophysics [84]. The evolution of a massive black hole binary can be roughly divided in three phases characterized by dynamical friction, slingshot interactions, and gravitational radiation. As the galaxies merge, the massive black holes interact

with the surrounding stellar population due to dynamical friction. The gravitational interaction between the moving massive body and the surrounding stars causes the smaller bodies to accelerate and gain energy and angular momentum, while the black hole is slowed by an amount to conserve the energy and angular momentum of the system. The black holes thus both tend to sink toward the center of the merged galaxy. The binding energy of the binary then increases from gravitational slingshot interactions ejecting stars on orbits intersecting the binary from the loss cone. The loss cone is defined as the set of orbits that intersect the binary or that pass within some distance of its center of mass. For example, stars within the tidal disruption loss cone are on a close enough approach to the black holes that tidal forces disrupt the star and these stars are removed in a single orbital period or less. For the binary to continue to bind, a repopulation of the loss cone is required. The repopulation of the loss cone is typically assumed to be driven by gravitational encounters between stars. If the binary separation does eventually become small enough, gravitational radiation then carries away the remaining angular momentum and the system mergers.

The infall of the black holes to this final stage characterized by gravitational wave emission such that the binary will decay within a Hubble time has been referred to as the "final parsec problem" [85]. Proposed mechanisms to overcome the final parsec problem include gas accretion, star-star encounters, and triaxial distortions of galactic nuclei [86]. Simulations show that if the galaxy is allowed to rotate binaries do coalesce within a Hubble time and the last parsec problem is avoided [87].

These results are consistent with observational evidence indicating that efficient coalescence is the norm. There is very little astrophysical evidence for binary black holes at $\sim$1 parsec separation, suggesting that this is not in fact a physical limit. If some galaxies were to contain uncoalesced binaries, galaxy mergers would bring a third black hole into the nucleus, and the resulting gravitational slingshot interaction

would eject one or more massive black holes from the nucleus. This would produce massive black holes away from the center of the galaxy, but no such off-center objects have been detected. It has also been suggested that ejections by three-body slingshot interactions would weaken the tight M-σ correlations that are observed [88]. This suggests that coalescence should proceed on short timescales. Studies have shown that LISA will be able to detect the gravitational waves from a significant fraction of such mergers in the universe [14].

We can also consider the fact that the gravitational wave coalescence time is shorter for more eccentric binaries [89], and as a result high-eccentricity binaries could be more likely to coalesce within a Hubble time [90, 83].

6.3 Eccentric Orbits of Binary Black Holes

The shape of the orbits of massive black hole binaries has been the subject of some debate. Some galaxy evolution models predict that the resulting central binary black hole system will enter the LISA band with significant orbital eccentricity [91, 92, 93], while other models suggest that the orbits will already have circularized [94, 95]. Stellar dynamical hardening might also leave the binary with non-zero eccentricity, where the binary is considered hard once the orbital velocity is larger than the velocity dispersion of stars in the galactic nucleus. N-body simulations find that perturbations of an initially circular binary from passing stars produce significant eccentricity by the time the binary becomes hard [82]. Analytic calculations and N-body simulations show that, in purely collisionless spherical backgrounds, the expected equilibrium distribution of eccentricities is skewed towards high $e \simeq 0.6 - 0.7$, and that dynamical friction does not play a major role in modifying such a distribution [96].

Simulations that follow the dynamics of binary black holes orbiting in massive, rotationally supported circumnuclear discs [97] suggest that if the binary is *counterrotating* with the disc the initial eccentricity does not decrease, and the black holes may enter the gravitational wave emission phase with high eccentricity. Complementary studies show that eccentricity evolution may occur in later stages of the binary's life because of close encounters with single stars [98] or gas-dynamical processes [99]. The gravitational interaction of the binary with a surrounding gas disc is likely to increase the eccentricity of the system. Another interesting scenario producing highly eccentric mergers that could be observed by LISA involves close triple supermassive black hole encounters [100].

While galaxy merger theories and simulations will continue to improve, it will be the LISA observations of massive black hole binary systems that will be able to provide conclusive answers about the shapes of binary black hole orbits in the centers of galaxies. In order to determine the eccentricity of a system of massive black holes LISA data analysis methods will need to include gravitational waveform templates for spinning black hole binaries in eccentric orbits. The next chapter discusses the calculation of such waveforms and studies the parameter estimation abilities of LISA for these sources.

CHAPTER 7

ECCENTRIC BINARY BLACK HOLE SYSTEMS

NASA's space based gravitational wave detector LISA will be able to detect gravitational waves from coalescing binary systems of compact objects. The gravitational waveforms from such systems have been calculated in various limits such as circular orbits or extreme mass ratios of the orbiting bodies. These limits can be extended to study how LISA observations can be used to measure the eccentricity of the orbits as well as the masses, spins, and luminosity distances of binary black holes. Once LISA is operational, the comparison of observations of eccentric and circular black hole binary sources will constrain theories on galaxy mergers in the early universe. The waveforms for binaries in eccentric orbits may also be necessary for the detection of highly eccentric binaries ($e \simeq 0.9$) predicted by some models. Gravitational wave tests of general relativity in the strong field regime will require the eccentric orbits from the full predictions of general relativity to measure deviations from theory. Alternative theories of gravity predict different gravitational waveforms than those in general relativity. A coherent residual left in the data stream after subtraction of the waveform predicted by general relativity would indicate that another theory could better match the data. Neglecting the effects on the waveform due to eccentricity would also lead to a coherent residual, possibly masking a departure from general relativity [17].

7.1 Spinning Binary Black Holes in Eccentric Orbits

Binary systems of compact objects will be ubiquitous sources for LISA [101, 83]. The gravitational waveforms from binary black hole systems have been studied in

various special limits such as circular orbits, extreme mass ratio inspirals (EMRIs), or specific spin orientations [7, 8, 9, 10, 102]. We have relaxed the assumption of circular orbits to calculate gravitational waveform templates that make it possible to accurately measure the eccentricity of binary black hole systems with LISA. Other parameters such as the masses and luminosity distance will be quite well determined for black hole binary systems and a bias in these parameters can be avoided by using the general eccentric waveforms, even in the case of very small eccentricity.

The *instantaneous* gravitational waveforms describing the early inspiral of a black hole binary with arbitrary spins, masses, and orbital eccentricity were calculated by Majár & Vasúth [103]. Together with the angular momentum and energy dissipation equations [104] we can build the *time dependent* gravitational waveforms for a general binary black hole system with the full seventeen parameters necessary to describe the system. These new waveforms will allow us to accurately measure parameter values for binary black hole systems, constrain galaxy merger scenarios, and permit tests of the theory of general relativity in the strong field regime.

Once LISA is operational, black hole studies with gravitational waves will constrain galaxy merger scenarios and provide critical new information on the distances and rates of massive black hole coalescences. In the last minutes before two super massive black holes collide the signal to noise ratio (SNR) of the source can grow into the thousands. LISA will be able to detect such loud events at vast distances, providing information about previously unprobed regions of the very distant universe. These strong field gravity events will also allow for testing the theory of general relativity and will help to confirm or revolutionize our understanding of physics. Neglecting the effects on the waveforms due to eccentricity results in a loss of estimated power and a bias in the values of the other parameters. Finding departures from the theory of general relativity with black hole waveforms also requires the fully eccentric wave-

forms since the eccentricity effects are on the order of the largest possible departures from theory. The strong field regime around supermassive black holes offers the best tests for Einstein's theory by measuring coherent residuals left after subtracting the waveform template predicted by general relativity from the data.

Black hole binary systems in eccentric orbits may very well be sources for ground based gravitational wave detectors such as LIGO and Virgo [105]. Some models predict that inspiral signals may enter the LIGO band with $e > 0.9$ and that eccentric templates could be necessary to detect such sources [106]. Current LIGO data analysis uses circular templates and could be upgraded to include the search for eccentric sources.

We present here a method for combining the work that has been done to calculate the instantaneous gravitational waveforms for eccentric binary systems with the dissipation equations for the orbital angular momentum and energy of the system and the spin precession equations to build time dependent gravitational waveforms for the general case of a spinning black hole binary system in an eccentric orbit [107].

7.2 Source Modeling

The general binary black hole gravitational waveform depends on seventeen parameters, including physical parameters and parameters describing the orientation of the source and the observer. The physical source parameters include two masses, three parameters to describe the spin of each body, the energy of the system, and three angular momentum parameters. The waveform at the detector also depends on sky location, the distance to the source, and two phase parameters. The specific choice of representation determines the list of parameters, but not the physical waveform output. For instance the concept of the eccentricity of the orbit is not a well defined

quantity in relativity, but some definition based on well defined quantities such as the energy and the magnitude of the orbital angular momentum can be adopted without loss of generality. The energy and magnitude of the orbital angular momentum can be replaced with an eccentricity e and semi-major axis a, defined as functions of E and L.

The first step in calculating the gravitational waveform for a binary black hole system is to solve the equations of motion for the orbital parameters, including the effects due to the spinning bodies. The spins of the black holes in a binary system contribute to the dynamics through both spin-orbit coupling and spin-spin coupling. The spin-orbit precession equations for the two spin vectors and the orbital momentum vector of the system are well known. There are also well known spin-spin effects due to the interaction of the two spins [104].

Binary black hole dynamics have been solved to various post-Newtonian (PN) orders, expanding in the small parameter $\left(\frac{v^2}{c^2}\right)$, assuming that the characteristic velocity of the system is small compared to the speed of light. The post-Newtonian expansion is valid at low orders for systems with $v \ll c$, which corresponds to times well before merger. As the black holes approach each other their velocities increase and higher order PN terms are required to accurately describe the system. We will focus on times well before merger and consider carefully the regime when our approximations begin to break down. The expansion parameter is related by Kepler's law to the total mass and semi-major axis of the binary $\left(\frac{v^2}{c^2} \sim \frac{M}{a}\right)$.

We have solved the various dynamics of the binary black hole system to 1.5 PN order $\left(\frac{v^3}{c^3}\right)$. The spin-spin effects come in at 2 PN order $\left(\frac{v^4}{c^4}\right)$ and to remain self consistent we have not included spin-spin terms. It is certainly possible to extend our treatment to the next order to consistently include these effects, but that will be left for future work.

7.2.1 Equations of Motion

The relativistic equations of motion for a bound binary system have been solved in a Kepler-like form in [108]. In the usual spherical coordinates and in terms of the eccentric anomaly u,

$$\mathbf{r} = r(\cos\phi, \sin\phi, 0) \tag{7.1a}$$

$$nt = u - e_t \sin u \tag{7.1b}$$

$$r = a(1 - e_r \cos u) \tag{7.1c}$$

$$\phi = 2(k+1)\tan^{-1}\left[\left(\frac{1+e_\phi}{1-e_\phi}\right)^{1/2}\tan\frac{u}{2}\right] \tag{7.1d}$$

where r is the relative separation of the two bodies, $n = 2\pi f$ is the mean motion, k is the fractional periastron advance per orbit, a is the semi-major axis, and the regular Keplerian eccentricity has split into the triad of time, radial, and angular eccentricities e_t, e_r, and e_ϕ.

The dynamics of the binary system are described by the Hamiltonian H. The Hamiltonian can be decomposed into its contributions to 1.5 PN order as $H_{\rm 1.5PN} = H_{\rm N} + H_{\rm 1PN} + H_{\rm 1.5PN}$. The solutions to the Hamiltonian to 1 PN were calculated in [108]. To isolate the spin-orbit effects which appear at 1.5 PN order $\left(\frac{v^3}{c^3}\right)$, the Newtonian and spin-orbit contributions to the Hamiltonian can be combined to form $H_{\rm NSO} = H_{\rm N} + H_{\rm SO}$. It is particularly useful to write the spin-orbit contribution in terms of an effective spin parameter $\mathbf{S}_{\rm eff}$:

$$H_{\rm NSO} = \frac{\mathbf{p^2}}{2\mu^2} - \frac{M}{r} + \frac{\mathbf{L}\cdot\mathbf{S}_{\rm eff}}{\mu r^3} \tag{7.2}$$

where the total mass of the system $M \equiv m_1 + m_2$, the reduced mass $\mu \equiv m_1 m_2/M$, $\mathbf{L}$ is the orbital angular momentum, and the effective spin $\mathbf{S}_{\rm eff}$, defined similarly in [109], has been used to express the spin-orbit effects compactly:

$$\mathbf{S}_{\rm eff} = \delta_1 \mathbf{S_1} + \delta_2 \mathbf{S_2} \tag{7.3}$$

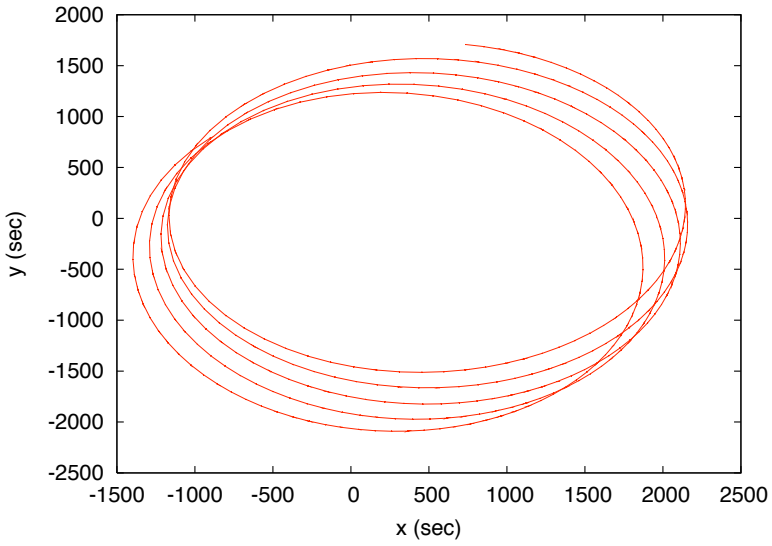

Figure 7.1: The precession of periastron in the orbital plane for a binary system with $e_r = 0.3$.

where

$$\delta_1 = 2\left(1 + \frac{3m_2}{4m_1}\right), \tag{7.4a}$$

$$\delta_2 = 2\left(1 + \frac{3m_1}{4m_2}\right). \tag{7.4b}$$

The Hamiltonian can be used to derive the equations of motion for the spins and the orbital velocity. In [109] it is shown that

$$\frac{d\mathbf{L}}{dt} = \{\mathbf{L}, H_{\rm NSO}\} = \frac{1}{r^3}\mathbf{S_{eff}} \times \mathbf{L}\,, \tag{7.5a}$$

$$\frac{d\mathbf{S}_1}{dt} = \{\mathbf{S}_1, H_{\rm NSO}\} = \frac{\delta_1}{r^3}\mathbf{L} \times \mathbf{S}_1\,, \tag{7.5b}$$

$$\frac{d\mathbf{S}_2}{dt} = \{\mathbf{S}_2, H_{\rm NSO}\} = \frac{\delta_2}{r^3}\mathbf{L} \times \mathbf{S}_2\,, \tag{7.5c}$$

where $\{\ \}$ are Poisson brackets.

It was also shown in [109] that the quantity $\mathbf{L}\cdot\mathbf{S}_{\rm eff}$ is conserved for constant $\mathbf{L}$, since

$$\begin{aligned}\frac{d\mathbf{S}_{\rm eff}}{dt} &= \delta_1\dot{\mathbf{S}}_{\mathbf{1}}+\delta_2\dot{\mathbf{S}}_{\mathbf{2}} = \frac{1}{r^3}\mathbf{L}\times(\delta_1^2\mathbf{S}_{\mathbf{1}}+\delta_2^2\mathbf{S}_{\mathbf{2}})\\ \frac{d}{dt}(\mathbf{L}\cdot\mathbf{S}_{\rm eff}) &= \frac{d\mathbf{L}}{dt}\cdot\mathbf{S}_{\rm eff}+\mathbf{L}\cdot\frac{d\mathbf{S}_{\rm eff}}{dt} = 0\,. \end{aligned} \tag{7.6}$$

We have derived the spin-orbit contribution to the orbital velocity from $H_{\rm NSO}$.

$$\begin{aligned}\frac{d\mathbf{r}}{dt} &= \{\mathbf{r},H_{\rm NSO}\}\\ \dot{\mathbf{r}} &= \frac{\mathbf{p}}{\mu}+\frac{\mathbf{S}_{\rm eff}\times\mathbf{r}}{r^3}\end{aligned} \tag{7.7}$$

We are working to 1.5 PN order, so we do not need to keep the higher order cross terms from $v^2=\dot{\mathbf{r}}\cdot\dot{\mathbf{r}}$. Keeping only the leading order spin-orbit term we find

$$\begin{aligned}v^2 &= \frac{p^2}{\mu^2}+\frac{2}{\mu}\frac{\mathbf{L}\cdot\mathbf{S}_{\rm eff}}{r^3}\\ v_\perp^2 &= \frac{L^2}{\mu^2r^2}+\frac{2}{\mu}\frac{\mathbf{L}\cdot\mathbf{S}_{\rm eff}}{r^3}\,.\end{aligned} \tag{7.8}$$

The relative velocity vector can then be written in terms of the energy E, the magnitude of the orbital angular momentum L, the relative separation between the black holes r, and the spin-orbit effects from $\mathbf{L}\cdot\mathbf{S_{eff}}$.

$$\begin{aligned}v^2 &= \frac{2E}{\mu}+\frac{2M}{r}-\left[3(1-3\eta)\left(\frac{E}{\mu}\right)^2+2(6-7\eta)\frac{EM}{\mu r}+(10-5\eta)\left(\frac{M}{r}\right)^2-\frac{\eta ML^2}{\mu^2r^3}\right]\,,\\ v_\parallel^2 &= \dot{r}^2=\frac{2E}{\mu}+\frac{2M}{r}-\frac{L^2}{\mu^2r^2}-\left[3(1-3\eta)\left(\frac{E}{\mu}\right)^2+2(6-7\eta)\frac{EM}{\mu r}+(10-5\eta)\left(\frac{M}{r}\right)^2\right.\\ &- \left.(2-6\eta)\frac{EL^2}{\mu^3r^2}-(8-3\eta)\frac{ML^2}{\mu^2r^3}\right]-\frac{2\mathbf{L}\cdot\mathbf{S_{eff}}}{\mu r^3}\,,\end{aligned} \tag{7.9}$$

and we find $v_\perp$ using $v_\perp^2=v^2-\dot{r}^2$. Here the dimensionless mass ratio $\eta\equiv\mu/M$ $(0<\eta<1/4)$.

The solutions to the Hamiltonian $H_{\rm NSO}$ for the case of simple precession, with either equal masses or with only one spinning body, can be found in [109]. There the

orbits and precession equations are solved simultaneously, but this can only be done for simple precession. The solutions for a system with general mass ratio and spin orientations were calculated in [110]. We also calculated the solutions for the general case, using the approximation that the orbital angular momentum is constant over an orbit resulting in the adiabatic form of the spin-orbit correction to the orbital parameters. The simple precession results do not agree with our results in the limit where the spin and angular momentum directions are aligned, a case where the adiabatic approach is exact. We also note that the results in [109] have spin-orbit effects that do not vanish for $\mathbf{S} = 0$, where the total spin vector $\mathbf{S} \equiv \mathbf{S_1} + \mathbf{S_2}$.

7.2.2 Non-Inertial Frame Effects

There is another correction to the equations of motion that comes in at 1.5 PN order due to the precession of the orbital angular momentum $\mathbf{L}$ from spin-orbit coupling. The coordinate system fixed to $\mathbf{L}$, with $\mathbf{r}$ defined to be in the orbital plane perpendicular to $\mathbf{L}$, is a non-ineritial precessing reference frame. The Keplerian style parameterization of the orbits is most easily accomplished in this non-inertial frame that precesses with the orbital plane, but the solutions must be modified to account for the non-inertial frame effects.

The equations of motion in the interial frame are

$$\frac{d\mathbf{r}}{dt} = \frac{\mathbf{p}}{\mu} + \frac{\mathbf{S}_{\rm eff} \times \mathbf{r}}{r^3}\,, \tag{7.10}$$

and

$$\frac{d\hat{L}}{dt} = \frac{\mathbf{S}_{\rm eff} \times \hat{L}}{r^3}\,. \tag{7.11}$$

The precessing frame is defined by the condition

$$\left.\frac{d\hat{L}}{dt}\right|_{\rm pre} = \mathbf{0} = \frac{d\hat{L}}{dt} - \boldsymbol{\omega} \times \hat{L}\,, \tag{7.12}$$

which implies that

$$\boldsymbol{\omega} = \frac{\mathbf{S}_{\rm eff}}{r^3}\,. \tag{7.13}$$

The velocity in the precessing frame is given by

$$\left.\frac{d\mathbf{r}}{dt}\right|_{\rm pre} = \frac{d\mathbf{r}}{dt} - \boldsymbol{\omega}\times\mathbf{r} = \frac{\mathbf{p}}{\mu} \tag{7.14}$$

from which it follows that the orbital plane remains fixed in the precessing frame and the radial motion looks identical in the inertial and precessing frames:

$$\dot{r}_{\rm pre} = \hat{r}\cdot\left.\frac{d\mathbf{r}}{dt}\right|_{\rm pre} = \hat{r}\cdot\frac{d\mathbf{r}}{dt} = \dot{r}\,. \tag{7.15}$$

Thus the solutions for a, e_r, n, and e_t are given as before in the inertial frame. In the inertial frame we have

$$v^2 = \dot{r}^2 + v_\perp^2 = 2\frac{E}{\mu} + \frac{2M}{r} \tag{7.16}$$

and

$$v_\perp^2 = \frac{L^2}{\mu^2 r^2} + \frac{2}{\mu}\frac{\mathbf{L}\cdot\mathbf{S}_{\rm eff}}{r^3}\,. \tag{7.17}$$

In the inertial frame $v_\perp$ comes from some combination of azimuthal and equitorial motion. In the precessing frame the motion is purely azimuthal: $v_\perp|_{\rm pre} = r\dot{\phi}$.

$$v_{\rm pre}^2 = v^2 - 2\boldsymbol{\omega}\cdot\mathbf{L} + \mathcal{O}(\omega^2) \tag{7.18}$$

so that

$$\left.v_\perp^2\right|_{\rm pre} = \frac{L^2}{\mu^2 r^2}\,. \tag{7.19}$$

Following the parameterization of [108] we can find the contribution to the orbital parameters from $\mathbf{L}\cdot\mathbf{S}_{\rm eff}$ in terms of the coefficients in (7.20) and (7.21). We can modify their coefficients to include the appropriate spin-orbit terms and solve for the corrections to the various orbital parameters.

$$\dot{r}^2 = A + 2B/r + C/r^2 + D/r^3 \tag{7.20}$$

$$\dot{\phi} = H/r^2 + I/r^3 \tag{7.21}$$

where

$$v_\perp^2 = r^2\dot{\phi}^2 \tag{7.22}$$

$$v^2 = \dot{r}^2 + v_\perp^2 \ . \tag{7.23}$$

The solutions for the orbital parameters based on the coefficients of Eqns. 7.20 and 7.21 are also given in [108]:

$$n = \frac{(-A)^{3/2}}{B} \tag{7.24a}$$

$$e_t = \left[1 - \frac{A}{B^2}\left(C - \frac{BD}{C_0}\right)\right]^{1/2} \tag{7.24b}$$

$$a = -\frac{B}{A} + \frac{D}{2C_0} \tag{7.24c}$$

$$e_r = e_t\left(1 + \frac{AD}{2BC_0}\right) \tag{7.24d}$$

$$k = \frac{H}{n\,\tilde{a}^2\left(1 - e_\phi^2\right)^{1/2}} - 1 \tag{7.25a}$$

$$e_\phi = e_t\left(1 + \frac{AD}{BC_0} - \frac{AI}{BH}\right) \tag{7.25b}$$

where $C_0 = -L^2/\mu^2$ and $\tilde{a} = a - I/(2H)$.

Suppressing the first post-Newtonian correction that can be found in various references [108, 111, 109] to highlight the contribution from the spin-orbit term at 1.5 PN

order we can express the orbital parameters as

$$a = -\frac{\mu M}{2E}\left(1 - 2\eta\frac{\mathbf{L}\cdot\mathbf{S}_{\rm eff}}{L^2}\frac{E}{\mu}\right) \tag{7.26a}$$

$$e_r^2 = 1 + 2\frac{EL^2}{\mu^3 M^2} + 8\left(1 + \frac{EL^2}{\mu^3 M^2}\right)\eta\frac{\mathbf{L}\cdot\mathbf{S}_{\mathbf{eff}}}{L^2}\frac{E}{\mu} \tag{7.26b}$$

$$n = \frac{1}{M}\left(-\frac{2E}{\mu}\right)^{3/2} \tag{7.26c}$$

$$e_t = e_r\left(1 - 2\eta\frac{\mathbf{L}\cdot\mathbf{S}_{\rm eff}}{L^2}\frac{E}{\mu}\right) \tag{7.26d}$$

It is interesting to note that there is no spin-orbit correction to the mean motion $n = 2\pi f$. The expressions for the angular eccentricity e_ϕ and the fractional periastron advance k each acquire an additional 1.5 PN correction due to the non-inertial frame effects in this precessing reference frame. Since there is no spin-orbit correction to $v_\perp^2 = r^2\dot{\phi}^2$ in the precessing frame, we have a new solution for the two orbital parameters that come from the $\dot{\phi}$ equation Eqn. 7.21. For our solutions in the precessing frame, the angular eccentricity e_ϕ and fractional perihelion advance k to 1.5 PN order are given by

$$k = \frac{3\mu^2 M^2}{L^2}\left(1 - \eta\frac{\mathbf{L}\cdot\mathbf{S}_{\rm eff}}{L^2}\right) \tag{7.27a}$$

$$e_\phi = e_r\left(1 - \frac{E}{\mu}\left(\eta - 2\eta\frac{\mathbf{L}\cdot\mathbf{S}_{\rm eff}}{L^2}\right)\right)\,. \tag{7.27b}$$

For completeness the spin-orbit correction to the perihelion precession k is included even though it is formally a 2.5 PN order term. These results are exact to 1.5 PN order, as long as the dissipation time scale is longer than the precession time scale (see the discussion in the section on the separation of time scales 7.2.6 that follows). The non-inertial frame terms are neglected in both [109, 110] and that may account for the discrepancies. We now have the exact solution for any spin magnitudes or orientations to 1.5 PN order.

7.2.3 Spin Supplementary Conditions

In comparing our results and various forms for the solutions to the equations of motion in the literature it must be noted that the spin-orbit contribution to the equations of motion depends on the choice of spin supplementary condition (SSC), described in the Appendix A of [104]. The choice of SSC results in different forms of the spin-orbit contribution to various orbital parameters, but the measurable physical results such as the gravitational waveform must remain invariant.

In [104] we find the following three examples of SSC choices and their resulting form of the spin-orbit acceleration $\mathbf{a}_{\rm SO}$:

$$\begin{aligned}\mathbf{a}_{\rm SO}^{(I)} = \quad & \frac{1}{r^3}\Big\{6\hat{\mathbf{n}}[(\hat{\mathbf{n}}\times\mathbf{v})\cdot(2\mathbf{S}+\frac{\delta m}{m}\mathbf{\Delta})] \\ & -[\mathbf{v}\times(7\mathbf{S}+3\frac{\delta m}{m}\mathbf{\Delta})] \\ & +3\dot{r}[\hat{\mathbf{n}}\times(3\mathbf{S}+\frac{\delta m}{m}\mathbf{\Delta})]\Big\},\end{aligned} \tag{7.28}$$

$$\begin{aligned}\mathbf{a}_{\rm SO}^{(II)} = \quad & \frac{1}{r^3}\Big\{\frac{3}{2}\hat{\mathbf{n}}[(\hat{\mathbf{n}}\times\mathbf{v})\cdot(7\mathbf{S}+3\frac{\delta m}{m}\mathbf{\Delta})] \\ & -[\mathbf{v}\times(7\mathbf{S}+3\frac{\delta m}{m}\mathbf{\Delta})] \\ & +\frac{3}{2}\dot{r}[\hat{\mathbf{n}}\times(7\mathbf{S}+3\frac{\delta m}{m}\mathbf{\Delta})]\Big\},\end{aligned} \tag{7.29}$$

$$\begin{aligned}\mathbf{a}_{\rm SO}^{(III)} = \quad & \frac{1}{r^3}\Big\{3\hat{\mathbf{n}}[(\hat{\mathbf{n}}\times\mathbf{v})\cdot(3\mathbf{S}+\frac{\delta m}{m}\mathbf{\Delta})] \\ & -[\mathbf{v}\times(7\mathbf{S}+3\frac{\delta m}{m}\mathbf{\Delta})] \\ & +6\dot{r}[\hat{\mathbf{n}}\times(2\mathbf{S}+\frac{\delta m}{m}\mathbf{\Delta})]\Big\},\end{aligned} \tag{7.30}$$

are given by the three different SSC's

$$S_A^{\mu\nu}u_{A\nu}=0, \tag{7.31}$$

$$2S_{Ai0} + S_{Aij}v_A^j = 0, \tag{7.32}$$

$$S_A^{i0} = 0, \tag{7.33}$$

respectively, where u_A^μ is the four-velocity of the center-of-mass world line X_A^μ of body A, and

$$S_A^{\mu\nu} \equiv 2\int_A (x^{[\mu} - X_A{}^{[\mu})\tau^{\nu]0} d^3x, \tag{7.34}$$

where $\tau^{\mu\nu}$ denotes the stress-energy tensor of matter plus gravitational fields satisfying $\tau^{\mu\nu}{}_{,\nu} = 0$, and square brackets around indices denote antisymmetrization. Note that the spin vector $\mathbf{S}$ of each body is defined by $S_A^i = \frac{1}{2}\epsilon_{ijk}S_A^{jk}$.

It has been shown that different forms of the SSC are equivalent up to a transformation of the center of mass of the system and can be neglected to lowest order [112]. At 1.5 PN order a change in SSC changes the definition of the location of the center of mass by a term that depends on the spins. This then changes the radiative moments, which in turn changes the waveforms h_+ and $h_\times$. The result is the same physical waveforms from the various SSC since the changes in the equations of motion are compensated for by changes in the waveform. It is thus important to remain consistent with the definition of the location of the center of mass for the chosen SSC for our calculations that include 1.5 PN order terms. In [104] the spin-orbit effects are calculated using the covariant SSC, while simpler equations for the relative motion of the binary can be calculated with the SSC used by [113]. We have thus chosen to use the SSC of [113] for our calculations. We have derived the results from our new choice of SSC and found that there are no changes to the waveform expressions to 1.5 PN order, but there would be new terms introduced at the next higher PN order.

The derivation of the waveforms h_+ and $h_\times$ in the covariant SSC can be found in Ref. [104] where

$$h^{ij} = \frac{2}{D}\Bigg\{ \overset{(2)}{I}{}^{ij} + \frac{1}{3}\overset{(3)}{I}{}^{ijk} N^k + \frac{1}{12}\overset{(4)}{I}{}^{ijkl} N^k N^l + \frac{1}{60}\overset{(5)}{I}{}^{ijklm} N^k N^l N^m + \cdots + \epsilon^{kl(i}\left[\frac{4}{3}\overset{(2)}{J}{}^{j)k} N^l + \frac{1}{2}\overset{(3)}{J}{}^{j)km} N^l N^m + \frac{2}{15}\overset{(4)}{J}{}^{j)kmn} N^l N^m N^n + \cdots\right]\Bigg\}_{TT}, \tag{7.35}$$

contains the mass multipole moments $I^{ij\cdots}$ and the current multipole moments $J^{ij\cdots}$. Here D is the distance from the source to the observer, N^i is a unit vector from the center of mass of the source to the observation point, the notation (n) over each multipole moment denotes the number of derivatives with respect to retarded time, ϵ^{ijk} is the completely antisymmetric Levi-Civita symbol, and parentheses around indices denote symmetrization.

Since we choose a different SSC than [104, 103] we must repeat the derivation of h_+ and $h_\times$ using the equations of motion and multipole moments in the appropriate SSC. We find that the appropriate correction to I^{ij} produces new terms in h^{ij} to higher order than we are working. The corresponding corrections to J^{ij} also produce new terms that first appear at 2 PN order. The extension of this work beyond 1.5 PN order will require the calculation of the terms that appear in the gravitational waveforms due to our choice of SSC.

7.2.4 Spin Precession

The total angular momentum of the binary system is $\mathbf{J} = \mathbf{L} + \mathbf{S_1} + \mathbf{S_2}$. In the absence of gravitational radiation, $\mathbf{J}$ is conserved and the orbital angular momentum

L and total spin angular momentum **S** precess as

$$\dot{\mathbf{L}} = -\dot{\mathbf{S}}\,. \tag{7.36}$$

The orbital angular momentum vector **L** can formally be written as the sum of post-Newtonian and spin-orbit contributions. In the SSC we have chosen, to 1.5 PN order

$$\mathbf{L} = \mathbf{L_N} + \mathbf{L_{PN}} + \mathbf{L_{SO}} \tag{7.37}$$

where

$$\begin{aligned} \mathbf{L}_{\rm N} &= \mu r v_\perp \\ \mathbf{L}_{\rm PN} &= \mathbf{L}_{\rm N}\left\{\frac{1}{2}v^2(1-3\eta)+(3+\eta)\frac{M}{r}\right\} \\ \mathbf{L}_{\rm SO} &= \frac{2\mu}{r}\hat{\mathbf{r}}\times(\hat{\mathbf{r}}\times\mathbf{S}_{\rm eff})\ . \end{aligned} \tag{7.38}$$

The instantaneous precession equations for the spin vectors of the two black holes are given by [104]

$$\dot{\mathbf{S}}_1 = \frac{1}{r^3}\left(\frac{4+3\zeta_1}{2}\,\mathbf{L}_N - \mathbf{S}_2 + \frac{3}{r^2}(\mathbf{r}\cdot\mathbf{S}_2)\,\mathbf{r}\right)\times\mathbf{S}_1 \tag{7.39}$$

$$\dot{\mathbf{S}}_2 = \frac{1}{r^3}\left(\frac{4+3\zeta_2}{2}\,\mathbf{L}_N - \mathbf{S}_1 + \frac{3}{r^2}(\mathbf{r}\cdot\mathbf{S}_1)\,\mathbf{r}\right)\times\mathbf{S}_2 \tag{7.40}$$

where $\zeta_1 = \zeta_2^{-1} = m_2/m_1$.

While it is possible to include the spin-spin interaction in the precession, we are self-consistently including effects up to 1.5 PN order in the description of motion and thus neglect the spin-spin interaction which appears at 2 PN order.

$$\dot{\mathbf{S}}_i = \frac{(4+3\zeta_i)}{2r^3}\,\mathbf{J}\times\mathbf{S}_i \tag{7.41}$$

for $i = 1, 2$.

7.2.5 Dissipation

The loss of energy and angular momentum due to gravitational wave emission has been observed in the Hulse-Taylor binary system of neutron stars, causing the objects to spiral in toward one another. The instantaneous energy and angular momentum dissipation equations for a binary system of compact objects are known to be [111, 104]

$$\dot{E}_{\rm N} = -\frac{8}{15}\frac{M^2\mu^2}{r^4}\left\{12v^2 - 11\dot{r}^2\right\} \tag{7.42}$$

$$\begin{aligned}\dot{E}_{\rm PN} = \quad & -\frac{2}{105}\frac{M^2\mu^2}{r^4}\Bigg\{(785-852\eta)v^4 - 160(17-\eta)\frac{M}{r}v^2 \\ & + 8(367-15\eta)\frac{M}{r}\dot{r}^2 - 2(1487-1392\eta)v^2\dot{r}^2 \\ & + 3(687-620\eta)\dot{r}^4 + 16(1-4\eta)\left(\frac{M}{r}\right)^2\Bigg\}\end{aligned} \tag{7.43}$$

$$\dot{\mathbf{J}}_{\rm N} = -\frac{8}{5}\frac{M\mu}{r^5}\left(\mu r v_\perp \hat{\mathbf{L}}\right)\left\{2v^2 - 3\dot{r}^2 + 2\frac{M}{r}\right\} \tag{7.44}$$

$$\begin{aligned}\dot{\mathbf{J}}_{\rm PN} = -\frac{2}{105}\frac{M\mu}{r^5}\left(\mu r v_\perp \hat{\mathbf{L}}\right)\Bigg\{&(307-548\eta)v^4 - 6(74-277\eta)v^2\dot{r}^2 + 2(372+197\eta)\frac{M}{r}\dot{r}^2 \\ &+15(19-72\eta)\dot{r}^4 - 4(58+95\eta)\frac{M}{r}v^2 - 2(745-2\eta)\left(\frac{M}{r}\right)^2\Bigg\}\,.\end{aligned}$$

The spin-orbit dissipation terms can be found in the above references as well as in [114] where they are written in terms of the total spin angular momentum $\mathbf{S} = \mathbf{S_1} + \mathbf{S_2}$ and a combination of the spins $\mathbf{Z} = \left(\frac{m_2}{m_1}\right)\mathbf{S_1} + \left(\frac{m_1}{m_2}\right)\mathbf{S_2}$.

$$\begin{aligned}\dot{E}_{\rm SO} \quad = \quad & -\frac{8\mu^2 M}{15r^6}\Bigg\{(\mathbf{L_N}\cdot\mathbf{S})\left(27\dot{r}^2 - 37v^2 - 12\frac{M}{r}\right) \\ & +(\mathbf{L_N}\cdot\mathbf{Z})\left(18\dot{r}^2 - 19v^2 - 8\frac{M}{r}\right)\Bigg\}\end{aligned} \tag{7.45}$$

$$
\begin{aligned}
\dot{\mathbf{J}}_{\rm SO} &= -\frac{4\mu^2}{5r^3}\Bigg\{\mathbf{S}\left(6v^2\dot{r}^2 - 6v^4 - \frac{50}{3}v^2\frac{M}{r} + \frac{50}{3}\dot{r}^2\frac{M}{r} - 2\frac{M^2}{r^2}\right) \\
&\quad +\mathbf{n}(\mathbf{n}\cdot\mathbf{S})\left(18v^4 - 30\dot{r}^2v^2 + 25v^2\frac{M}{r} + 6\dot{r}^2\frac{M}{r} + 2\frac{M^2}{r^2}\right) \\
&\quad +\dot{r}\mathbf{n}(\mathbf{v}\cdot\mathbf{S})\left(6v^2 - 21\frac{M}{r}\right) - \dot{r}\mathbf{v}(\mathbf{n}\cdot\mathbf{S})\left(18v^2 - 30\dot{r}^2 + 33\frac{M}{r}\right) \\
&\quad +\mathbf{v}(\mathbf{v}\cdot\mathbf{S})\left(6v^2 - 12\dot{r}^2 + 23\frac{M}{r}\right) \\
&\quad +\mathbf{Z}\left(5\dot{r}^4 - 2v^2\dot{r}^2 - \frac{10}{3}v^4 - \frac{22}{3}v^2\frac{M}{r} + \frac{23}{3}\dot{r}^2\frac{M}{r} - \frac{4M^2}{3r^2}\right) \\
&\quad +\mathbf{n}(\mathbf{n}\cdot\mathbf{Z})\left(13v^4 - 20\dot{r}^2v^2 + \frac{41}{3}v^2\frac{M}{r} + 6\dot{r}^2\frac{M}{r} + \frac{4M^2}{3r^2}\right) \\
&\quad +\dot{r}\mathbf{n}(\mathbf{v}\cdot\mathbf{Z})\left(7v^2 - 5\dot{r}^2 - \frac{34M}{3r}\right) - \dot{r}\mathbf{v}(\mathbf{n}\cdot\mathbf{Z})\left(13v^2 - 20\dot{r}^2 + \frac{64M}{3r}\right) \\
&\quad +\mathbf{v}(\mathbf{v}\cdot\mathbf{Z})\left(\frac{10}{3}v^2 - 5\dot{r}^2 + \frac{38M}{3r}\right)\Bigg\}. \qquad (7.46)
\end{aligned}
$$

7.2.6 Separation of Time Scales

There are several relevant time scales to consider for a binary system of black holes. The orbital time scale can be expressed as the orbital frequency or the orbital period. To first order, the orbital time scale is given by Kepler's law where the orbital period squared is proportional to the semi-major axis cubed, $T^2 \propto a^3$.

$$T_{\rm orb} \sim 2\pi a^{\frac{3}{2}} M^{-\frac{1}{2}} \qquad (7.47)$$

The rate of the advance of periastron is related to the orbital time scale by

$$T_{\rm peri} \sim \frac{2\pi}{k} T_{\rm orb} \qquad (7.48)$$

$$\frac{T_{\rm peri}}{T_{\rm orb}} \sim \frac{a}{M} \qquad (7.49)$$

As expected, periastron advance is a 1 PN effect relative to the orbital time scale.

The time scale on which the orbital angular momentum $\mathbf{L}$ and spins $\mathbf{S_1}$ and $\mathbf{S_2}$ precess about the total angular momentum $\mathbf{J}$ is the precession time scale. The magnitude of the precession vector $\omega_{\rm prec}$ is calculated above and given in Eqn. 7.13. The magnitude of the effective spin vector $S_{\rm eff} \sim M^2$ since the magnitude of the individual spins is given by $S_i = \chi_1 m_i^2$ where the dimensionless spin parameter $\chi_i \sim 1$.

$$T_{\rm prec} \sim \frac{1}{\omega_{\rm prec}} \sim \frac{\mu}{M}\left(\frac{a}{M}\right)^3 \tag{7.50}$$

$$\frac{T_{\rm prec}}{T_{\rm orb}} \sim \left(\frac{a}{M}\right)^{\frac{3}{2}} \tag{7.51}$$

We see that the precession effects come in at 1.5 PN order compared to the orbital time scale.

The rate at which the system loses energy and angular momentum due to gravitational wave emission defines the decay time scale.

$$T_{\rm decay} \sim \frac{E}{\dot{E}} \sim \frac{L}{\dot{L}} \tag{7.52}$$

$$\frac{T_{\rm decay}}{T_{\rm orb}} \sim \frac{1}{\eta}\left(\frac{a}{M}\right)^{\frac{5}{2}} \tag{7.53}$$

At times well before the merger of the system $\left(\frac{a}{M}\right)$ is large and

$$T_{\rm decay} > T_{\rm prec} > T_{\rm peri} > T_{\rm orb}\,. \tag{7.54}$$

Toward the end of the evolution of the system the times scales begin to become comparable. At this point the post-Newtonian approximations to the equations of motion and gravitational waveforms also begin to break down. Considering only times early in the evolution of the system we have a clean separation of time scales and the different processes can be treated differently in the calculations. This simplifies the

problem by allowing an adiabatic treatment where the dissipation is assumed to be small over the course of an orbit and the eccentricity and semi-major axis, e_r and a, are treated as constant while calculating an individual orbit.

The precession time scale is also greater than the orbital time scale for times well before merger. The precession of the spin and angular momentum vectors can thus be calculated on a coarse grid compared to the orbits.

7.2.7 Orbit Averaged Dissipation and Precession

The equations needed to numerically calculate time dependent gravitational waveforms for binary black hole systems have all been derived to various post-Newtonian orders. The whole system of equations could be solved on the orbital time scale with enough time steps to sufficiently resolve each orbit. The separation of time scales allows for an alternative method for solving the equations that is less computationally expensive. Since the decay and precession timescales are much longer than the orbital timescale we can start with a solution to the orbital equations of motion that neglects dissipation. This allows us to use Nyquist sampling of just a couple of samples per orbit for the quantities that depend on the dissipation and precession equations. We would therefore like to know the orbital averages of instantaneous dissipation and precession equations given above.

To average over an orbital period T, denoted by brackets $\langle\rangle$, we integrate $F(t)$ [115]

$$\langle F\rangle = \frac{1}{T}\int_0^T F(t)\,dt = \frac{1}{2\pi}\int_0^{2\pi} 2\pi f\,\frac{dt}{d\phi}\,F(\phi)\,d\phi\ . \tag{7.55}$$

We have chosen a parameterization using the eccentric anomaly u and can write the integral in terms of u.

$$\langle F\rangle = \frac{1}{2\pi}\int_0^{2\pi} n\,\frac{dt}{du}\,F(u)\,du = \frac{1}{2\pi}\int_0^{2\pi} (1-e_t\cos(u))\ F(u)\,du \tag{7.56}$$

where $n = 2\pi f$ and we have used

$$\dot{u} = \frac{n}{(1 - e_t \cos(u))} \ . \tag{7.57}$$

We use this integral to orbit average the instantaneous dissipation equations given above and take advantage of the computational savings from the separation of time scales.

The equations for the orbit averaged dissipation equations to 1 PN order have already been calculated and can be found in [111]. The orbit averages for the $\dot{E}_{\rm SO}$ and $\dot{\mathbf{J}}_{\rm SO}$ terms had not been previously calculated, but are given here. The orbit averaged spin-orbit contribution to the energy dissipation is given by

$$\begin{aligned} \left\langle \dot{E}_{\rm SO} \right\rangle &= \frac{M^2\mu^2}{30a^7(1-e^2)^{11/2}}[\mathbf{L}\cdot\mathbf{S}(784 + 5480e^2 + 3810e^4 + 195e^6) \\ &\quad + \mathbf{L}\cdot\mathbf{Z}(432 + 2928e^2 + 1962e^4 + 96e^6)] \end{aligned} \tag{7.58}$$

Remaining consistent at 1.5 PN order the magnitudes of the spin vectors are conserved ($\dot{S}_i = 0$) and the dissipation of J is due entirely to the loss of L. The time dependent direction of $\mathbf{L}$ is determined by both the precession equations and the component of the dissipation that is perpendicular to $\hat{\mathbf{L}}$. The magnitudes L and J are changed by the component of $\dot{\mathbf{J}}_{\rm SO}$ parallel to $\hat{L}$. Here we write the total change to $\mathbf{L}$ due to spin-orbit effects. The terms with components of the spin vectors along $\mathbf{L}$ change the magnitude of L while those perpendicular to $\mathbf{L}$ (in the orbital plane) change the direction of the orbital angular momentum vector.

$$\begin{aligned} \left\langle \dot{\mathbf{L}}_{\rm SO} \right\rangle &= \frac{M^2\mu^2}{15a^5(1-e^2)^{7/2}}\Bigg\{-\frac{\mathbf{Z}_\perp}{4}(480 + 2496e^2 + 671e^4) \\ &\quad - \frac{\mathbf{S}_\perp}{2}(332 + 1572e^2 + 435e^4) + 2\,\mathbf{Z}_\parallel(72 + 296e^2 + 74e^4) \\ &\quad + \mathbf{S}_\parallel(296 + 1032e^2 + 237e^4)\Bigg\} \end{aligned} \tag{7.59}$$

where $\mathbf{S}_\parallel = \hat{\mathbf{L}}(\hat{\mathbf{L}}\cdot\mathbf{S})$, $\mathbf{S}_\perp = \mathbf{S} - \mathbf{S}_\parallel$, and similarly for $\mathbf{Z}_\parallel$ and $\mathbf{Z}_\perp$.

Averaged over an orbital period the spin precession equations become

$$\left\langle \dot{\mathbf{S}}_\mathbf{1} \right\rangle = \frac{(1-e^2)^{-\frac{3}{2}}}{2a^3}\Bigg\{(\mathbf{L_N}\times\mathbf{S_1})(4+3\frac{m_2}{m_1})+\mathbf{S_2}\times\mathbf{S_1} - 3(\hat{\mathbf{L}}_\mathbf{N}\cdot\mathbf{S_2})\hat{\mathbf{L}}_\mathbf{N}\times\mathbf{S_1}\Bigg\}, \tag{7.60}$$

$$\left\langle \dot{\mathbf{S}}_\mathbf{2} \right\rangle = \frac{(1-e^2)^{-\frac{3}{2}}}{2a^3}\Bigg\{(\mathbf{L_N}\times\mathbf{S_2})(4+3\frac{m_1}{m_2})+\mathbf{S_1}\times\mathbf{S_2} - 3(\hat{\mathbf{L}}_\mathbf{N}\cdot\mathbf{S_1})\hat{\mathbf{L}}_\mathbf{N}\times\mathbf{S_2}\Bigg\}. \tag{7.61}$$

Compared to the case of a circular orbit, the factor of r^3 in the denominator becomes $(a\sqrt{1-e^2})^3$. Again the spin-spin terms can be neglected at 1.5 PN order.

7.2.8 Eccentricity Evolution

The eccentricity of an orbit is ordinarily not a well defined quantity in general relativity since it depends on the choice of coordinate system. This does not prevent the adoption of some proxy for the eccentricity at any moment, defined as a relationship between the energy and angular momentum of the system. It would be possible to define a gauge invariant definition of the eccentricity of a system using a physical observable such as the gravitational waveform. For our purposes adopting some definition of the eccentricity will suffice. Following the form of [111, 109], to first post-Newtonian order the instantaneous radial eccentricity of the orbit can be defined as

$$e_r^2 = 1 + 2\frac{EL^2}{\mu^3M^2} + \frac{E}{\mu}\left[2(\eta-6)+5(\eta-3)\frac{EL^2}{\mu^3M^2}\right] + 8\left(1+\frac{EL^2}{\mu^3M^2}\right)\eta\frac{\mathbf{L}\cdot\mathbf{S_{eff}}}{L^2}\frac{E}{\mu}\ . \tag{7.62}$$

The dissipation equations for E and L should ensure that the eccentricity decreases as the system loses energy and angular momentum. This is indeed true if the expressions for e_r^2, $\dot{E}$, and $\dot{L}$ are expanded to all orders. For the truncated equations

that we use to calculate the various quantities there exist terms that tend to cause e_r^2 to grow for small values of e_r. We would like to have a stable decay of e_r for small values of e_r, including e_r remaining zero once the orbit becomes circular.

It is possible to correct the behavior of e_r due to truncation in the $e = 0$ limit by adding a correction term to either the energy or angular momentum evolution equation.

$$\dot{E}_{\rm fix} = \frac{-\frac{\partial(e_r^2)}{\partial L}\dot{L} - \frac{\partial(e_r^2)}{\partial E}\dot{E}}{\frac{\partial(e_r^2)}{\partial E}} \tag{7.63}$$

where $\dot{L}$ and $\dot{E}$ are evaluated at $e = 0$ and

$$\frac{\partial(e_r^2)}{\partial L} = 2\frac{EL}{\mu^2 M}\left(2 + 5\frac{E}{\mu}\eta - 15\frac{E}{\mu}\right) + 8\frac{E}{\mu}\left(\frac{E}{\mu} - \frac{\mu^2 M^2}{L^2}\right)\eta\frac{\mathbf{L}\cdot\mathbf{S_{eff}}}{L\mu M} \ ,$$

$$\frac{\partial(e_r^2)}{\partial E} = 2\left[\frac{L^2}{\mu^2 M^2} + (5\eta - 15)\frac{EL^2}{\mu^3 M^2} + (\eta - 6) + \left(\frac{4\mu^2 M^2}{L^2} + 8\right)\eta\frac{\mathbf{L}\cdot\mathbf{S_{eff}}}{\mu^2 M^2}\right] \ . \tag{7.64}$$

Even this attempt to modify the numerical behavior of the eccentricity so that it behaves in a physical way breaks down at some point. Using the energy and angular momentum dissipation equations we found that small changes in initial radial eccentricity resulted in very different merger times for systems with all of their other parameters identical. This unphysical result revealed the shortcoming of using the $\left\langle \dot{E} \right\rangle$ and $\left\langle \dot{L} \right\rangle$ equations and motivated a conversion from the parameters (E, L) to (e_r, a). It is still necessary to use the vector equation for $\left\langle \dot{\mathbf{L}} \right\rangle$ since the change in the direction of $\mathbf{L}$ is governed by the perpendicular component of the $\left\langle \dot{\mathbf{L}} \right\rangle$ equation.

The calculation of the complementary $\langle \dot{e}_r \rangle$ and $\langle \dot{a} \rangle$ equations involves using the expressions for $e_r^2(E, L)$ and $a(E, L)$ to find the expressions $\dot{e}_r(\dot{E}, \dot{L})$ and $\dot{a}(\dot{E}, \dot{L})$ and orbit averaging using the equations of motion that include the spin-orbit effects. We are once again faced with the problem of needing a stable decay of e_r for small values of e_r, including e_r remaining zero once the orbit becomes circular. We can see that

since

$$\frac{de_r^2}{dt} = 2e_r\dot{e_r} \ , \tag{7.65}$$

if the terms that come from differentiating Eqn. 7.62 come in at order e_r^2 we will have an expression for $\dot{e}_r$ that is proportional to e_r and that has the behavior we expect for small e_r and $e_r = 0$.

Eqn. 7.62 gives the expression for e_r^2 in terms of E and L, including the spin-orbit effects due to $\mathbf{L} \cdot \mathbf{S_{eff}}$. The corresponding expression for a is

$$a = -\frac{\mu M}{2E}\left(1 - \frac{E}{2\mu}(\eta - 7) - 2\eta\frac{\mathbf{L}\cdot\mathbf{S_{eff}}}{L^2}\frac{E}{\mu}\right) \ . \tag{7.66}$$

Differentiating these expressions with respect to time and using Eqns. 7.64,

$$\begin{aligned} 2e_r\dot{e_r} &= \frac{\partial(e_r^2)}{\partial E}\dot{E} + \frac{\partial(e_r^2)}{\partial L}\dot{L} \\ \dot{a} &= \frac{\partial(a)}{\partial E}\dot{E} + \frac{\partial(a)}{\partial L}\dot{L} \ . \end{aligned} \tag{7.67}$$

To take advantage of the computational savings associated with the separation of time scales we want to find the orbit averaged dissipation equations for the parameters e_r and a to 1.5 PN order. This calculation involves differentiating the 1.5 PN expressions for e_r^2 and a as in Eqns. 7.67 and orbit averaging the 1.5 PN expressions for $\dot{E}$ and $\dot{L}$ with the 1.5 PN equations of motion. There will be terms that come out of the calculation at higher PN order that can be neglected for our 1.5 PN treatment. For instance, the 1.5 PN terms in the expressions for e_r^2 and a only need to be combined with the 0 PN $\dot{E}$ and $\dot{L}$ terms orbit averaged with the 0 PN equations of motion to be consistent to 1.5 PN order.

$$
\begin{aligned}
\left\langle \dot{e_r}^{\mathrm{N}} \right\rangle &= -\frac{1}{15}\frac{\mu}{M^2}\left(\frac{M}{a}\right)^4 \frac{e_r}{(1-e_r^2)^{7/2}}(304+121e_r^2)(1-e_r^2) \\
\left\langle \dot{e_r}^{1} \right\rangle &= -\frac{1}{15}\frac{\mu}{M^2}\left(\frac{M}{a}\right)^4 \frac{e_r}{(1-e_r^2)^{7/2}}\{-\frac{1}{56}\frac{M}{a}[8(16705+4676\eta) \\
&\quad +12(9082+2807\eta)e_r^2-(25211-3388\eta)e_r^4]\} \\
\left\langle \dot{e_r}^{\mathrm{SO}} \right\rangle &= -\frac{1}{30}\frac{\mu}{M^4}\left(\frac{M}{a}\right)^{11/2} \frac{e_r}{(1-e_r^2)^4}\{(7032\,\hat{\mathbf{L}}\cdot\mathbf{S}+4408\,\hat{\mathbf{L}}\cdot\mathbf{Z}) \\
&\quad +(5592\,\hat{\mathbf{L}}\cdot\mathbf{S}+2886\,\hat{\mathbf{L}}\cdot\mathbf{Z})e_r^2+(1313\,\hat{\mathbf{L}}\cdot\mathbf{S}+875\,\hat{\mathbf{L}}\cdot\mathbf{Z})e_r^4\} \quad (7.68)
\end{aligned}
$$

$$
\begin{aligned}
\left\langle \dot{a}^{\mathrm{N}} \right\rangle &= -\frac{2}{15}\frac{\mu}{M}\left(\frac{M}{a}\right)^3 \frac{1}{(1-e_r^2)^{9/2}}(96+292e_r^2+37e_r^4)(1-e_r^2) \\
\left\langle \dot{a}^{1} \right\rangle &= -\frac{2}{15}\frac{\mu}{M}\left(\frac{M}{a}\right)^3 \frac{1}{(1-e_r^2)^{9/2}}\{-\frac{1}{28}\frac{M}{a}[(14008+4704\eta)+(80124+21560\eta)e_r^2 \\
&\quad +(17325+10458\eta)e_r^4-\frac{1}{2}(5501-1036\eta)e_r^6]\} \\
\left\langle \dot{a}^{\mathrm{SO}} \right\rangle &= \frac{1}{15}\frac{\eta}{M^2}\left(\frac{M}{a}\right)^{9/2} \frac{1}{(1-e_r^2)^5}\{(2128\,\hat{\mathbf{L}}\cdot\mathbf{S}+1440\,\hat{\mathbf{L}}\cdot\mathbf{Z})+(7936\hat{\mathbf{L}}\cdot\mathbf{S}+4770\hat{\mathbf{L}}\cdot\mathbf{Z})e_r^2 \\
&\quad +(3510\,\hat{\mathbf{L}}\cdot\mathbf{S}+1737\,\hat{\mathbf{L}}\cdot\mathbf{Z})e_r^4+(363\,\hat{\mathbf{L}}\cdot\mathbf{S}+222\,\hat{\mathbf{L}}\cdot\mathbf{Z})e_r^6\} \quad (7.69)
\end{aligned}
$$

While the calculation of Eqns. 7.68 and 7.69 can be done with all of the required expressions to 1.5 PN order, in practice the calculation can be done in its various pieces. Using the notation that $\langle F^a \rangle_b$ gives the expression for F to a PN order, orbit averaged with the equations of motion to b PN order, to 1.5 PN order

$$
\left\langle F^{1.5} \right\rangle_{1.5} = \left\langle F^{0} \right\rangle_{1.5} + \left\langle F^{1.5} \right\rangle_{0} \ . \quad (7.70)
$$

It turns out that in the $\langle \dot{e}_r \rangle$ calculation, the two terms on the right hand side of Eqn. 7.70 each separately cancel all of their e_r^0 terms that can cause the unphysical behavior of the eccentricity dissipation.

We find that Eqns. 7.68 and 7.69 ensure the proper behavior of the eccentricity as seen in Figures 7.2 and 7.3. These new decay equations require that we write

the parameterized orbital equations Eq. 7.26 and Eq. 7.27 as functions of e_r and a, replacing E and L with the appropriate expressions.

$$E = -\frac{\mu}{2}\left(\frac{M}{a}\right) + \frac{\mu}{8}(7-\eta)\left(\frac{M}{a}\right)^2 - \frac{\mu}{2}\frac{\hat{\mathbf{L}}\cdot\mathbf{S}_{\rm eff}}{M^2(1-e_r^2)^{1/2}}\left(\frac{M}{a}\right)^{5/2} \tag{7.71}$$

$$\begin{aligned} L &= \mu M(1-e_r^2)^{1/2}\left(\frac{a}{M}\right)^{1/2}\left(1+\frac{(4+2e_r^2-\eta e_r^2)}{2(1-e_r^2)}\left(\frac{M}{a}\right)\right. \\ &\quad \left. -\frac{\hat{\mathbf{L}}\cdot\mathbf{S}_{\rm eff}}{M^2}\frac{(3+e_r^2)}{2(1-e_r^2)^{3/2}}\left(\frac{M}{a}\right)^{3/2}\right) \end{aligned} \tag{7.72}$$

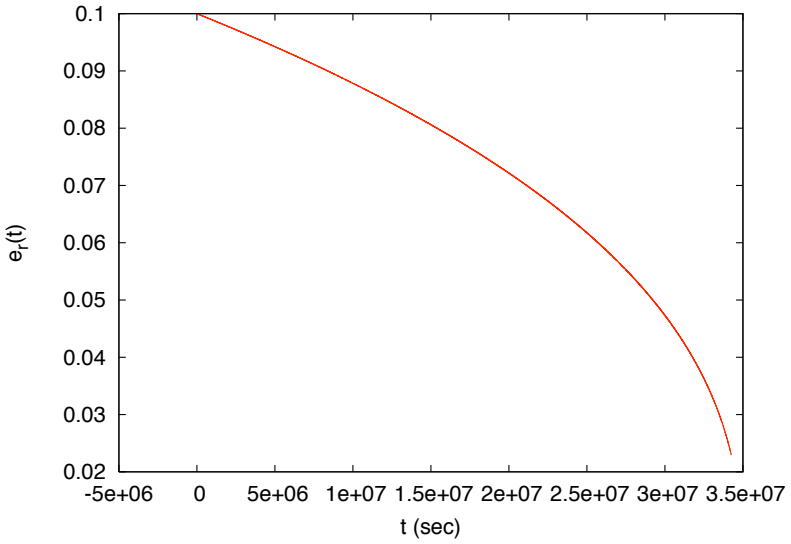

Figure 7.2: The dissipation of eccentricity for a binary black hole system with initial radial eccentricity $e_0 = 0.1$.

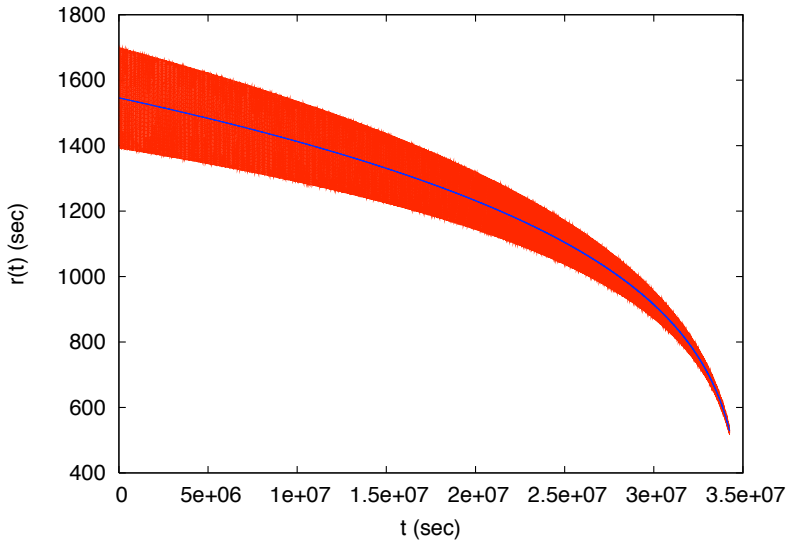

Figure 7.3: The relative separation r in red and the semi-major axis a in blue show the inspiral of the system as a decays as well as the circularization of the binary as r_{min} and r_{max} tend toward a.

We find the following expressions for the 1.5 PN orbital parameters written as functions of e_r and a.

$$n = \frac{1}{M}\left(\frac{M}{a}\right)^{3/2}\left(1 - \frac{1}{2}\left(\frac{M}{a}\right)(9-\eta) + \frac{3}{2}\left(\frac{M}{a}\right)^{3/2}\frac{\hat{\mathbf{L}}\cdot\mathbf{S}_{\rm eff}}{M^2\sqrt{1-e_r^2}}\right) \tag{7.73a}$$

$$e_t = e_r\left(1 + \frac{1}{2}\left(\frac{M}{a}\right)(3\eta - 8) + \left(\frac{M}{a}\right)^{3/2}\frac{\hat{\mathbf{L}}\cdot\mathbf{S}_{\rm eff}}{M^2\sqrt{1-e_r^2}}\right) \tag{7.73b}$$

$$k = \frac{3}{(1-e_r^2)}\left(\frac{M}{a}\right) - 3\left(\frac{M}{a}\right)^{3/2}\frac{\hat{\mathbf{L}}\cdot\mathbf{S}_{\rm eff}}{M^2(1-e_r^2)^{3/2}} \tag{7.73c}$$

$$e_\phi = e_r\left(1 + \frac{\eta}{2}\left(\frac{M}{a}\right) - \left(\frac{M}{a}\right)^{3/2}\frac{\hat{\mathbf{L}}\cdot\mathbf{S}_{\rm eff}}{M^2\sqrt{1-e_r^2}}\right) \tag{7.73d}$$

We have now fully described the time dependence of the system to 1.5 PN order, taking advantage of the separation of time scales for spinning binary black hole systems in eccentric orbits far from merger. We can now build time dependent waveforms

based on the previously calculated instantaneous gravitational waveforms for these systems.

7.2.9 Instantaneous Waveforms

The gravitational radiation from orbiting bodies was first calculated by [89] and has been extended in the post-Newtonian expansion by various authors [115, 116, 111].

The gravitational wave polarization states h_+ and $h_\times$ for spinning compact binaries in eccentric orbits have been given by [103]. The various post-Newtonian and spin-orbit contributions to the waveform are indicated by the superscript.

$$
\begin{aligned}
h_+^{\rm N} &= \left(\dot r^2 - \frac{M}{r}\right)(p_x^2 - q_x^2) + 2v_\perp \dot r (p_x p_y - q_x q_y) + v_\perp^2 (p_y^2 - q_y^2)\ , && (7.74)\\
h_+^{0.5} &= \frac{\delta m}{M}\left(\left(\dot r\left[\frac{2M}{r} - \frac{\dot r^2}{2}\right]N_x + v_\perp\left[\frac{M}{2r} - \dot r^2\right]N_y\right)(p_x^2 - q_x^2)\right.\\
&+ v_\perp\left(\left[\frac{3M}{r} - 2\dot r^2\right]N_x - 2v_\perp \dot r N_y\right)(p_x p_y - q_x q_y)\\
&- \left. v_\perp^2\left(\dot r N_x + v_\perp N_y\right)(p_y^2 - q_y^2)\right)\ , && (7.75)\\
h_+^{1} &= \frac{1}{6}\left((1-3\eta)\left[\left(-\frac{21\dot r^2 M}{r} + \frac{3Mv^2}{r} + 6\dot r^4 + \frac{7M^2}{r^2}\right)N_x^2\right.\right.\\
&+ 4v_\perp \dot r\left(-\frac{6M}{r} + 3\dot r^2\right)N_x N_y + 2v_\perp^2\left(3\dot r^2 - \frac{M}{r}\right)N_y^2\Big]\\
&+ \left.\left[\frac{(19-9\eta)\dot r^2 M}{r} + (3-9\eta)v^2\dot r^2 - \frac{(10+3\eta)v^2 M}{r} + \frac{29M^2}{r^2}\right]\right)(p_x^2 - q_x^2)\\
&+ \frac{v_\perp}{6}\left((1-3\eta)\left[6\dot r\left(-\frac{5M}{r} + 2\dot r^2\right)N_x^2\right.\right.\\
&+ 8v_\perp\left(-4\frac{M}{r} + 3\dot r^2\right)N_x N_y + 12v_\perp^2 \dot r N_y^2\Big]\\
&+ \left.6\dot r\left[\frac{(2+4\eta)M}{r} + (1-3\eta)v^2\right]\right)(p_x p_y - q_x q_y)\\
&+ \frac{v_\perp^2}{6}\left((1-3\eta)\left[2\left(-\frac{7M}{r} + 3\dot r^2\right)N_x^2 + 12v_\perp \dot r N_x N_y + 6v_\perp^2 N_y^2\right]\right.\\
&+ \left.\left[-\frac{(4-6\eta)M}{r} + (3-9\eta)v^2\right]\right)(p_y^2 - q_y^2)\ , && (7.76)\\
h_+^{\rm SO} &= -\frac{1}{r^2}\left[(\mathbf{\Delta}\cdot\mathbf{q})p_x + (\mathbf{\Delta}\cdot\mathbf{p})q_x\right]\ , && (7.77)
\end{aligned}
$$

$$
\begin{aligned}
h_+^{1.5} &= \frac{\delta m}{M}\left\{(1-2\eta)\left(\dot r\left[\frac{3\dot r^2 M}{4r}-\frac{v^2M}{r}-\frac{41M^2}{12r^2}-\dot r^4\right]N_x^3\right.\right.\\
&+ v_\perp\left[\frac{85\dot r^2M}{8r}-\frac{9v^2M}{8r}-\frac{7M^2}{2r^2}-3\dot r^4\right]N_x^2N_y\\
&+ \left.3\dot r v_\perp^2\left[\frac{2M}{r}-\dot r^2\right]N_xN_y^2+v_\perp^3\left[\frac{M}{4r}-\dot r^2\right]N_y^3\right)\\
&+ \dot r\left[-\frac{(10+7\eta)\dot r^2M}{2r}+\frac{(2+\eta)v^2M}{2r}-\frac{(59-30\eta)M^2}{12r^2}-\frac{(1-5\eta)v^2\dot r^2}{2}\right]N_x\\
&+ v_\perp\left[-\frac{(25+26\eta)\dot r^2M}{8r}+\frac{(7-2\eta)v^2M}{8r}-\frac{(26-3\eta)M^2}{6r^2}\right.\\
&- \left.\left.\frac{(1-5\eta)v^2\dot r^2}{2}\right]N_y\right\}(p_x^2-q_x^2)\\
&+ v_\perp\frac{\delta m}{M}\left\{(1-2\eta)\left(\left[\frac{\dot r^2M}{4r}-\frac{7v^2M}{4r}-\frac{11M^2}{r^2}-2\dot r^4\right]N_x^3\right.\right.\\
&+ \left.v_\perp\dot r\left[\frac{16M}{r}-6\dot r^2\right]N_x^2N_y+3v_\perp^2\left[\frac{5M}{2r}-2\dot r^2\right]N_xN_y^2-2v_\perp^3\dot rN_y^3\right)\\
&+ \left[-\frac{(49+14\eta)\dot r^2M}{4r}+\frac{(11-6\eta)v^2M}{4r}-\frac{(32-9\eta)M^2}{3r^2}-(1-5\eta)v^2\dot r^2\right]N_x\\
&- \left.v_\perp\dot r\left[\frac{(2+6\eta)M}{r}+(1-5\eta)v^2\right]N_y\right\}(p_xp_y-q_xq_y)\\
&+ v_\perp^2\frac{\delta m}{M}\left\{(1-2\eta)\left(-\dot r\left[\frac{5M}{4r}+\dot r^2\right]N_x^3\right.\right.\\
&+ \left.v_\perp\left[\frac{29M}{4r}-3\dot r^2\right]N_x^2N_y-3v_\perp^2\dot rN_xN_y^2-v_\perp^3N_y^3\right)\\
&- \dot r\left[\frac{(7+3\eta)M}{r}+\frac{(1-5\eta)v^2}{2}\right]N_x\\
&+ \left.v_\perp\left[\frac{(3-8\eta)M}{4r}-\frac{(1-5\eta)v^2}{2}\right]N_y\right\}(p_y^2-q_y^2)\ ,
\end{aligned}
\tag{7.78}
$$

$$h^{\rm N}_{\times} = 2\left(\left(\dot{r}^2 - \frac{M}{r}\right)p_x q_x + v_\perp \dot{r}(p_x q_y + q_x p_y) + v_\perp^2 p_y q_y\right) \ , \tag{7.79}$$

$$\begin{aligned} h^{0.5}_{\times} &= \frac{\delta m}{M}\left(\dot{r}\left[\frac{4M}{r} - \dot{r}^2\right]N_x + v_\perp\left[\frac{M}{r} - 2\dot{r}^2\right]N_y\right)p_x q_x \\ &+ v_\perp\left(\left[\frac{3M}{2r} - \dot{r}^2\right]N_x - v_\perp \dot{r} N_y\right)(p_x q_y + q_x p_y) \\ &- 2v_\perp^2\left(\dot{r}N_x + v_\perp N_y\right)p_y q_y \ , \end{aligned} \tag{7.80}$$

$$\begin{aligned} h^{1}_{\times} &= \frac{1}{3}\Bigg((1-3\eta)\Bigg(\left[-\frac{21\dot{r}^2 M}{r} + \frac{3Mv^2}{r} + 6\dot{r}^4 + \frac{7M^2}{r^2}\right]N_x^2 \\ &+ 4v_\perp\dot{r}\left[-\frac{6M}{r} + 3\dot{r}^2\right]N_x N_y + 2v_\perp^2\left[3\dot{r}^2 - \frac{M}{r}\right]N_y^2\Bigg) \\ &+ \left[\frac{(19-9\eta)\dot{r}^2 M}{r} + (3-9\eta)v^2\dot{r}^2 - \frac{(10+3\eta)v^2 M}{r} + \frac{29M^2}{r^2}\right]\Bigg)p_x q_x \\ &+ \frac{v_\perp}{6}\Bigg((1-3\eta)\Bigg(6\dot{r}\left[-\frac{5M}{r} + 2\dot{r}^2\right]N_x^2 \\ &+ 8v_\perp\left[-4\frac{M}{r} + 3\dot{r}^2\right]N_x N_y + 12v_\perp^2\dot{r}N_y^2\Bigg) \\ &+ 6\dot{r}\left[\frac{(2+4\eta)M}{r} + (1-3\eta)v^2\right]\Bigg)(p_x q_y + q_x p_y) \\ &+ \frac{v_\perp^2}{3}\Bigg((1-3\eta)\Bigg(2\left[-\frac{7M}{r} + 3\dot{r}^2\right]N_x^2 + 12v_\perp\dot{r}N_x N_y + 6v_\perp^2 N_y^2\Bigg) \\ &- \left[\frac{(4-6\eta)M}{r} - (3-9\eta)v^2\right]\Bigg)p_y q_y \ , \end{aligned} \tag{7.81}$$

$$h^{\rm SO}_{\times} = -\frac{1}{r^2}\left[(\mathbf{\Delta}\cdot\mathbf{q})q_x - (\mathbf{\Delta}\cdot\mathbf{p})p_x\right] \ , \tag{7.82}$$

$$
\begin{aligned}
h_{\times}^{1.5} &= \frac{\delta m}{M}\left\{(1-2\eta)\left(\dot{r}\left[\frac{3\dot{r}^2M}{2r}-\frac{2v^2M}{r}-\frac{41M^2}{6r^2}-2\dot{r}^4\right]N_x^3\right.\right.\\
&+ v_\perp\left[\frac{85\dot{r}^2M}{4r}-\frac{9v^2M}{4r}-\frac{7M^2}{r^2}-6\dot{r}^4\right]N_x^2N_y\\
&+ 6\dot{r}v_\perp^2\left[\frac{2M}{r}-\dot{r}^2\right]N_xN_y^2+v_\perp^3\left[\frac{M}{2r}-2\dot{r}^2\right]N_y^3\Big)\\
&+ \dot{r}\left[-\frac{(10+7\eta)\dot{r}^2M}{r}+\frac{(2+\eta)v^2M}{r}-\frac{(59-30\eta)M^2}{6r^2}-(1-5\eta)v^2\dot{r}^2\right]N_x\\
&+ v_\perp\left[-\frac{(25+26\eta)\dot{r}^2M}{4r}+\frac{(7-2\eta)v^2M}{4r}\right.\\
&- \left.\left.\frac{(26-3\eta)M^2}{3r^2}-(1-5\eta)v^2\dot{r}^2\right]N_y\right\}p_xq_x\\
&+ v_\perp\frac{\delta m}{M}\left\{(1-2\eta)\left(\left[\frac{\dot{r}^2M}{4r}-\frac{7v^2M}{4r}-\frac{11M^2}{r^2}-2\dot{r}^4\right]N_x^3\right.\right.\\
&+ v_\perp\dot{r}\left[\frac{16M}{r}-6\dot{r}^2\right]N_x^2N_y+3v_\perp^2\left[\frac{5M}{2r}-2\dot{r}^2\right]N_xN_y^2-2v_\perp^3\dot{r}N_y^3\Big)\\
&+ \left[-\frac{(49+14\eta)\dot{r}^2M}{4r}+\frac{(11-6\eta)v^2M}{4r}-\frac{(32-9\eta)M^2}{3r^2}-(1-5\eta)v^2\dot{r}^2\right]N_x\\
&- \left.v_\perp\dot{r}\left[\frac{(2+6\eta)M}{r}+(1-5\eta)v^2\right]N_y\right\}(p_xq_y+q_xp_y)\\
&+ v_\perp^2\frac{\delta m}{M}\left\{(1-2\eta)\left(-\dot{r}\left[\frac{5M}{2r}+\dot{r}^2\right]N_x^3\right.\right.\\
&+ v_\perp\left[\frac{29M}{2r}-6\dot{r}^2\right]N_x^2N_y-6v_\perp^2\dot{r}N_xN_y^2-2v_\perp^3N_y^3\Big)\\
&- \left.\dot{r}\left[\frac{(14+6\eta)M}{r}+(1-5\eta)v^2\right]N_x+v_\perp\left[\frac{(3-8\eta)M}{2r}-(1-5\eta)v^2\right]N_y\right\}p_yq_y\ ,
\end{aligned}
\tag{7.83}
$$

where $\delta m = m_2 - m_1$, and $\mathbf{\Delta} = M(\mathbf{S}_2/m_2 - \mathbf{S}_1/m_1)$

The instantaneous waveforms calculated by [103] are given in the comoving coordinate system defined by the motion of the system in the orbital plane and the line of sight vector $\hat{\mathbf{N}}$. The choice of defining the gravitational waves at the source in the comoving coordinate system leads to a form for h_+ and $h_\times$ where the orbital time dependence is carried in the components of the basis vectors $\hat{\mathbf{N}}$, $\hat{\mathbf{p}}$, and $\hat{\mathbf{q}}$.

The line of sight vector $\hat{\mathbf{N}}$ represents the direction from the source to the observer. For the LISA detector the center of the observer coordinate system is located at the barycenter while the LIGO coordinate system is located at the geocenter. $\hat{\mathbf{N}}$ does not change over the observation time and is used to help define both the invariant and comoving coordinate systems for a pair of orbiting black holes.

7.2.9.1 Invariant Coordinate System: The invariant coordinate system is defined by the total angular momentum vector $\mathbf{J}$ and the line of sight vector $\hat{\mathbf{N}}$. The total angular momentum is a slowly changing quantity with $\dot{\mathbf{J}} = \dot{\mathbf{L}}$ because the orbital angular momentum $\mathbf{L}$ decays due to gravitational wave emission and the direction of $\mathbf{L}$ precesses due to spin-orbit coupling effects. The spin vectors of the black holes $\mathbf{S}_1$ and $\mathbf{S_2}$ change direction but not magnitude to 1.5 PN order.

In the invariant coordinate system $\hat{\mathbf{J}} = \hat{\mathbf{k}}$. We choose $\hat{\mathbf{N}}$ to be in the i-k plane and define the angle between $\hat{\mathbf{N}}$ and $\hat{\mathbf{J}}$ such that $\hat{\mathbf{N}} \cdot \hat{\mathbf{J}} = \cos\gamma$. We can then write $\hat{\mathbf{N}}$ in these coordinates as

$$\begin{pmatrix} N_i \\ N_j \\ N_k \end{pmatrix} = \begin{pmatrix} \sin\gamma \\ 0 \\ \cos\gamma \end{pmatrix} \tag{7.84}$$

7.2.9.2 Comoving Coordinate System: The comoving coordinate system is defined by the orbital angular momentum vector $\mathbf{L}$, the separation vector $\mathbf{r}$, and the line of sight vector $\hat{\mathbf{N}}$. In this coordinate system that is attached to the separation vector, $\hat{\mathbf{r}} = \hat{\mathbf{x}}$ and $\hat{\mathbf{L}} = \hat{\mathbf{z}}$.

The polarization vectors $\hat{\mathbf{p}}$ and $\hat{\mathbf{q}}$ are perpendicular to the line of sight and are defined as

$$\hat{\mathbf{p}} \equiv \frac{\hat{\mathbf{L}} \times \hat{\mathbf{N}}}{|\hat{\mathbf{L}} \times \hat{\mathbf{N}}|} \tag{7.85}$$

$$\hat{\mathbf{q}} \equiv \hat{\mathbf{N}} \times \hat{\mathbf{p}} \tag{7.86}$$

With this definition, $\hat{\mathbf{p}}$ is always in the orbital plane and $\hat{\mathbf{p}} = (p_i, p_j, 0)$. Using the additional conditions of orthonormality, $\hat{\mathbf{p}} \cdot \hat{\mathbf{p}} = 1$ and $\hat{\mathbf{N}} \cdot \hat{\mathbf{p}} = 0$, we can calculate the components of $\hat{\mathbf{p}}$.

$$\begin{pmatrix} p_i \\ p_j \\ p_k \end{pmatrix} = \frac{1}{(N_x^2 + N_y^2)^{\frac{1}{2}}} \begin{pmatrix} -N_y \\ N_x \\ 0 \end{pmatrix} \tag{7.87}$$

Similarly, we can find the components of $\hat{\mathbf{q}}$ in the comoving system.

$$\begin{pmatrix} q_i \\ q_j \\ q_k \end{pmatrix} = \frac{1}{(N_x^2 + N_y^2)^{\frac{1}{2}}} \begin{pmatrix} -N_x N_z \\ N_y N_z \\ N_x^2 + N_y^2 \end{pmatrix} \tag{7.88}$$

To transform any vector $\mathbf{u}$ in the comoving system to a vector $\mathbf{u}'$ in the invariant coordinate system we use a set of time dependent rotation matrices.

$$\mathbf{u}' = R_k(\Phi) R_i(i_S) R_k(\Psi) \mathbf{u} \tag{7.89}$$

The rotation angles are Ψ, the polar angle on orbital plane, Φ, the precession of the orbital plane, and i_S, the precession cone angle.

$$\hat{\mathbf{N}} = \begin{pmatrix} \cos\Psi \cos\Phi \sin\gamma + \sin\Psi(-\sin\Phi \sin\gamma \cos i_S + \cos\gamma \sin i_S) \\ -\sin\Psi \cos\Phi \sin\gamma + \cos\Psi(-\sin\Phi \sin\gamma \cos i_S + \cos\gamma \sin i_S) \\ \sin i_S \sin\Phi \sin\gamma + \cos\gamma \cos i_S \end{pmatrix} \tag{7.90}$$

We find the necessary angles to calculate $\left(\hat{\mathbf{N}}, \hat{\mathbf{p}}, \hat{\mathbf{q}}\right)$ in the comoving frame from the physical vector quantities associated with the system defined in the barycenter

reference frame

$$\hat{\mathbf{J}} \cdot \hat{\mathbf{L}} = \cos i_S \tag{7.91}$$

$$\hat{\mathbf{J}} \cdot \hat{\mathbf{N}} = \cos \gamma \tag{7.92}$$

$$\left(\frac{\hat{\mathbf{N}} \times \hat{\mathbf{J}}}{\sin \gamma} \right) \cdot \left(\frac{\hat{\mathbf{J}} \times \hat{\mathbf{L}}}{\sin i_S} \right) = \cos \Phi \ . \tag{7.93}$$

We integrate the following to find Ψ:

$$\dot{\Psi} = \dot{\phi} - \cos i_S \, \dot{\Phi} \ . \tag{7.94}$$

All of the pieces necessary to build efficient time dependent inspiral waveforms for spinning black hole binary systems in eccentric orbits up to 1.5 PN order have now been calculated. Figures 7.4 and 7.5 show the gravitational wave signal $h_+(t)$ and LISA A channel response $A(t)$ for an eccentric binary black hole system. These efficient time dependent gravitational waveforms can now be used to study several gravitational wave parameter estimation problems. Parameter estimation for ground based detectors such as Advanced LIGO and the Einstein Telescope and the use of eccentric waveforms to test alternative theories of gravity are left for future work. The LISA parameter estimation study is described in the next section.

7.3 Parameter Estimation with LISA

We can now use our general time dependent gravitational waveforms to study how well LISA will be able to measure the full set of seventeen parameters necessary to describe a spinning binary black hole system in an eccentric orbit. We are especially interested in the ability of the mission to distinguish small eccentricity values from zero.

A preliminary study using the established Extreme Mass Ratio Inspiral (EMRI) waveforms [44, 117, 95] extended to include small mass ratios indicated how well we

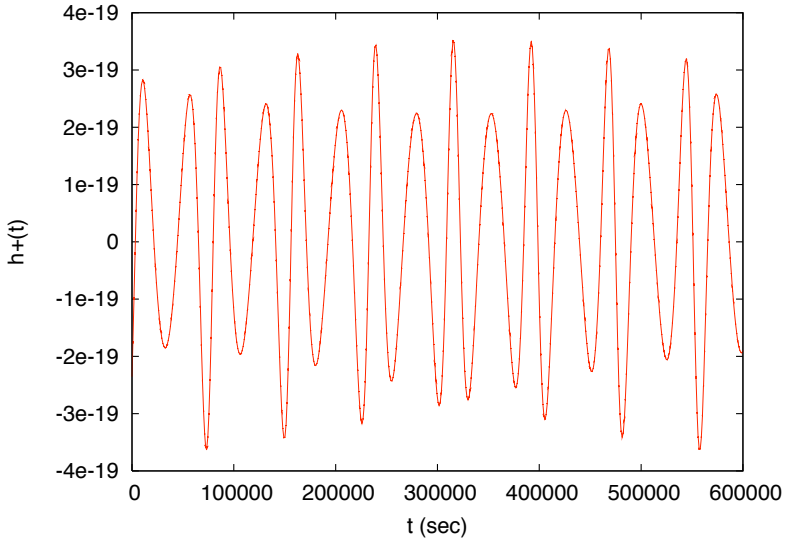

Figure 7.4: The time dependent gravitational waveform $h_+(t)$ in the source frame for a binary black hole system with $e_0 = 0.2$.

might be able to determine the eccentricity parameter for black hole binary systems. We used the non-spinning case to simplify the waveforms, reasoning that the added modulation due to the spin parameters would tend to tighten the parameter estimation ranges resulting in a conservative upper limit. This early study indicated that the eccentricity parameter would be very well determined, with the initial eccentricity when the signal enters the LISA band resolvable for values as small as $e_0 \approx 10^{-3}$ as shown in Figure 7.6.

The full study involves the efficient time dependent waveforms for spinning black hole binary systems in eccentric orbits derived in the previous section. The post-Newtonian expansion begins to break down as the system nears merger. For our calculations out to 1.5 PN order, we choose to terminate our waveforms near $a \approx 20M$, where the expansion parameter $\frac{M}{a} \approx 0.05$. This termination condition is conservative in terms of the SNR LISA will be able to extract from this type of source. Most of the

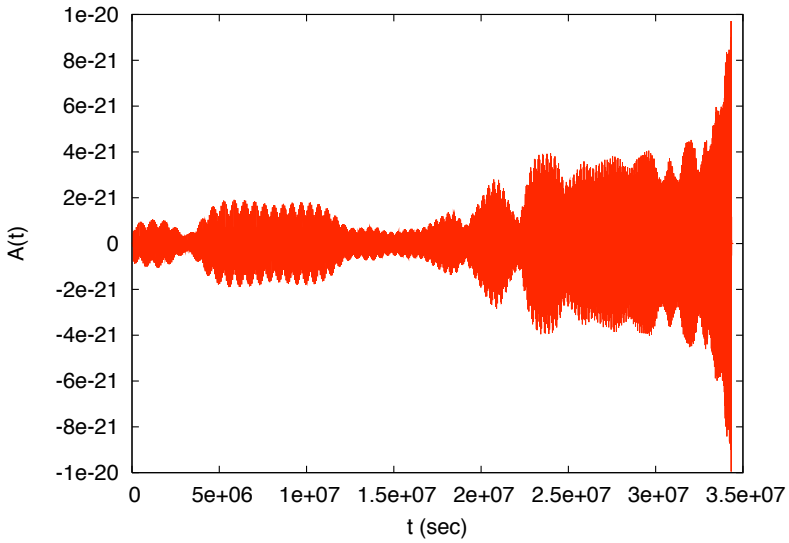

Figure 7.5: The A channel LISA detector response to the spinning binary black hole system in Figure 7.4. Modulations in amplitude are due to the detector motion and the spin precession effects. The overall gravitational wave amplitude grows as the system spirals in and nears merger.

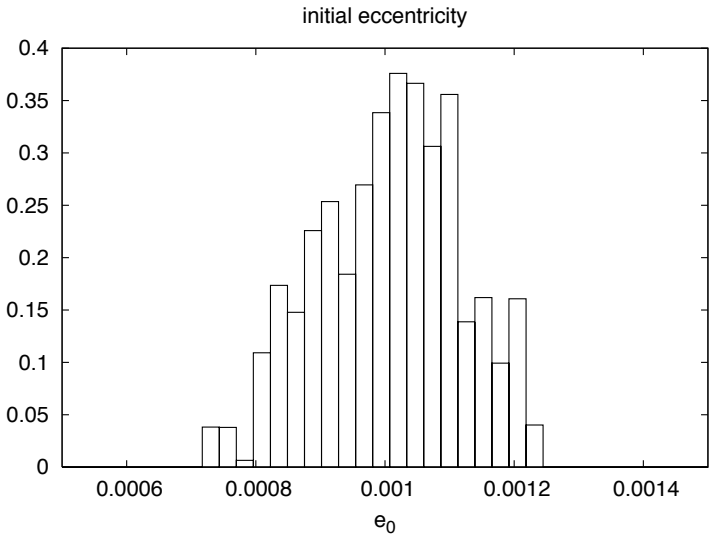

Figure 7.6: Normalized posterior distribution of initial radial eccentricity values e_0 sampled by a Markov Chain Monte Carlo for a non-spinning binary black hole system with SNR= 410 injected into simulated LISA data indicating that the eccentricity when the signal enters the LISA band will be distinguishable from zero for values of $e_0 \sim 10^{-3}$.

SNR comes from times near merger, so the extension of the validity of the waveforms closer to merger results in a big increase in SNR. Our study here is thus a pessimistic estimate of how well LISA will be able to determine the various source parameters. In the case of the radial eccentricity parameter however, the circularization of the waveform toward merger means that most of the eccentricity information is encoded at times well before merger. While increased SNR would improve the determination of the other source parameters, we find that the eccentricity is not highly correlated with the other parameters. Our choice for when to truncate the waveforms thus should not have much of an effect on our study of how well LISA will be able to determine the eccentricity parameter for black hole binary systems.

We chose for our study an observation time of one year, with the merger time just less than the full observation time. In order to choose initial parameter values for a system that will merge in approximately one year, we need to calculate an initial semi-major axis based on the lifetime estimate for a system with some given initial radial eccentricity. The lifetime for an eccentric binary system was derived in [94]. There the author defines

$$\beta = \frac{64}{5}\mu M^2 \tag{7.95}$$

and the lifetime for a system in a circular orbit ($e_0 = 0$)

$$T_c = \frac{a_0^4}{4\beta} \ . \tag{7.96}$$

We want to know the semi-major axis at some time before merger $t \sim$ year and some given e_0. We use

$$a_0 = C(e_0)\,(4\beta T_c)^{1/4} \tag{7.97}$$

where $C(e_0)$ is some correction factor due to the eccentricity of the orbit, expanded in powers of e_0:

$$C(e_0) = 1 + \frac{157}{172}e_0^2 + \frac{5799977}{7336832}e_0^4 + \frac{1888175763}{2523870208}e_0^6 \ . \tag{7.98}$$

We use parameter ranges consistent with typical LISA sources, given in Table 7.1.

Table 7.1: Parameter ranges for our study of spinning black hole binary systems in eccentric orbits.

Parameter	Minimum	Maximum
m_1	$10^5 M_\odot$	$10^7 M_\odot$
m_2	$10^5 M_\odot$	$10^7 M_\odot$
D_L	1 Gpc	100 Gpc
e_0	0	1
a_0	20 M	1000 M
χ_1	0	1
χ_2	0	1
$\cos\theta$	-1	1
$\cos\theta_L$	-1	1
$\cos\theta_{S_1}$	-1	1
$\cos\theta_{S_2}$	-1	1
ϕ	0	2π
ϕ_L	0	2π
ϕ_{S_1}	0	2π
ϕ_{S_2}	0	2π
n_0	0	2π
ϕ_0	0	2π

The masses are given in terms of the mass of the Sun, $M_\odot = 1.9891 \times 10^{30}$ kg, and the luminosity distance D_L is given in units of gigaparsecs, Gpc. The dimensionless spin parameters χ_1 and χ_2 combine with the black hole masses to give the magnitudes of the spins,

$$S_i = \chi_i m_i^2 \ . \tag{7.99}$$

There are initial orientation parameters for the orbital angular momentum vector $\mathbf{L}$, $\cos\theta_L$ and ϕ_L, as well as the spin vectors $\mathbf{S_i}$, $\cos\theta_{S_i}$ and ϕ_{S_i}. The final two parameters n_0 and ϕ_0 are initial phase parameters for the mean motion n and orbital phase ϕ. In the circular limit these parameters are degenerate, but eccentric orbits

require a second phase parameter beyond the initial orbital phase to specify the initial orientation of periastron.

Here we study several representative cases to establish that various LISA sources will have eccentricities distinguishable from zero for initial radial eccentricities $e_0 \approx 10^{-3}$. Marginalized posterior distribution histograms are shown in Figure 7.7 for sources with the same parameter values and SNR = 237 but with several different initial radial eccentricity values. The source parameters are given in Table 7.2. By

Table 7.2: Injected parameter values for two sets of sources with a range of values for e_0. The results of the parameter estimation study for Source 1 are given in Figure 7.7 and the results for Source 2 are given in Figure 7.8.

Parameter	Source 1	Source 2
m_1	$2 \times 10^6 M_\odot$	$2 \times 10^6 M_\odot$
m_2	$1 \times 10^6 M_\odot$	$1 \times 10^6 M_\odot$
D_L	6.36167 Gpc	6.36167 Gpc
e_0	0.001-0.2	0.002-0.1
a_0	69 M	69 M
χ_1	0.5	0.5
χ_2	0.8	0.8
$\cos\theta$	0.2	0.4
$\cos\theta_L$	-0.5	-0.5
$\cos\theta_{S_1}$	-0.8	-0.8
$\cos\theta_{S_2}$	0.6	0.6
ϕ	1.2	2.0
ϕ_L	2.6	2.6
ϕ_{S_1}	0.4	0.4
ϕ_{S_2}	1.7	1.7
n_0	0.2	0.2
ϕ_0	1.65	1.65
SNR	237	576

varying the initial radial eccentricity and keeping the other source parameters constant we find that LISA can determine the value of e_0 to parts in a thousand. This result does not depend on the initial value e_0. This sugggests that the smallest initial

radial eccentricity values detectable for typical LISA sources will be $e_0 \sim 10^{-3}$. We can see in Figure 7.7 that for small values of the initial eccentricity with $e_0 \approx 10^{-3}$ there is weight in the posterior distribution at $e_0 = 0$, indicating that the search could not clearly distinguish a waveform with small eccentricity from a circular waveform. In this example of a typical LISA source (Table 7.2, Source 1) an initial radial eccentricity of $e_0 = 0.005$ is distinguishable from $e_0 = 0$, but the $e_0 = 0.002$ case is just on the margin of detectability (Figure 7.7). Changing just the sky location of this source (Table 7.2, Source 2), there is increased SNR and the $e_0 = 0.002$ case is distinguishable from circular (Figure 7.8).

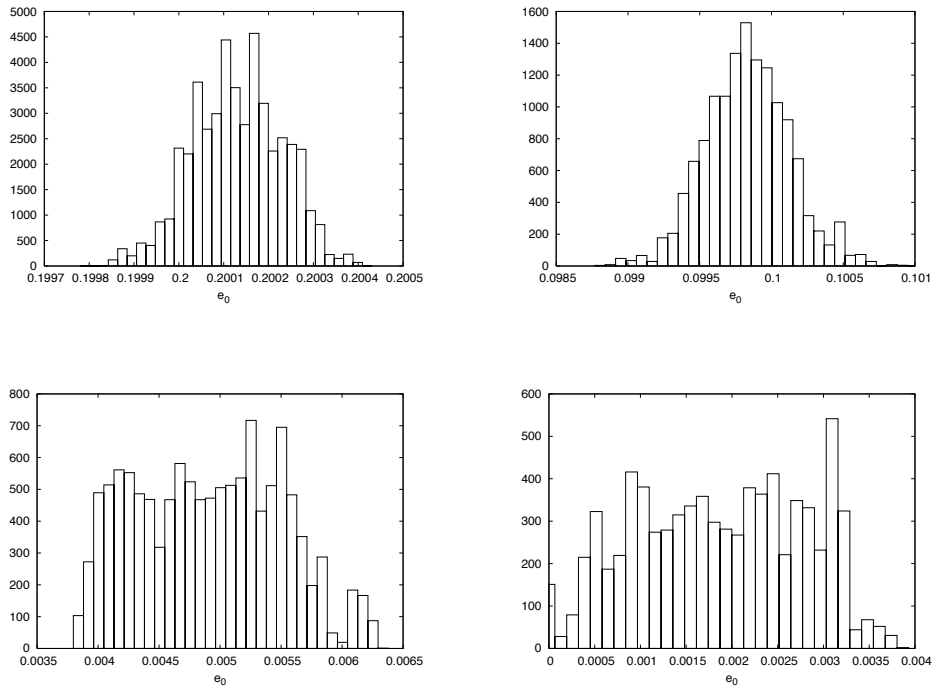

Figure 7.7: The marginalized posterior distribution for the initial radial eccentricity for sources with the same parameter values and SNR = 237, but different initial eccentricities. Top left $e_0 = 0.2$, top right $e_0 = 0.1$, bottom left $e_0 = 0.005$, bottom right $e_0 = 0.002$. The other parameter values are given in Table 7.2, Source 1.

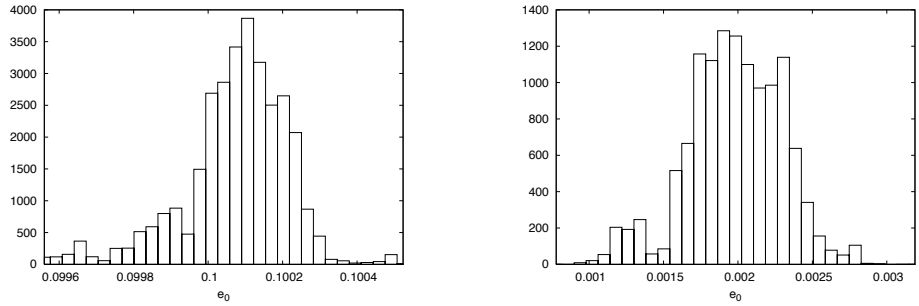

Figure 7.8: The marginalized posterior distribution for the initial radial eccentricity for sources with the same parameter values and SNR = 576, but different initial eccentricities. On the left $e_0 = 0.1$, and on the right $e_0 = 0.002$. For this source, $e_0 = 0.002$ is distinguishable from the circular case. The other parameter values are given in Table 7.2, Source 2.

The other source parameters are also measured quite well by LISA, as seen in some examples in Figure 7.9 and Figure 7.11. Marginalized posterior distributions are shown for the two individual masses, the distance to the source, the initial radial eccentricity, and the two sky location parameters. The injected parameters are given in Table 7.2, except for the initial radial eccentricity $e_0 = 0.3$. The parameters with dimension are given in terms of the natural log of their values because the Fisher matrix calculation uses dimensionless parameters. In each case the Fisher matrix prediction for a Gaussian distribution about the injected value is given by the blue line. The posterior distribution is not expected to be centered on the injected parameter value because the detector noise tends to shift the maximum likelihood location off of the injected source parameters. The corresponding two dimensional posterior distribution for the sky location parameters can be seen in Figures 7.10 and 7.12.

The comprehensive study of the full parameter space is beyond the scope of this project. If we were to choose just two values of each parameter to study the resulting

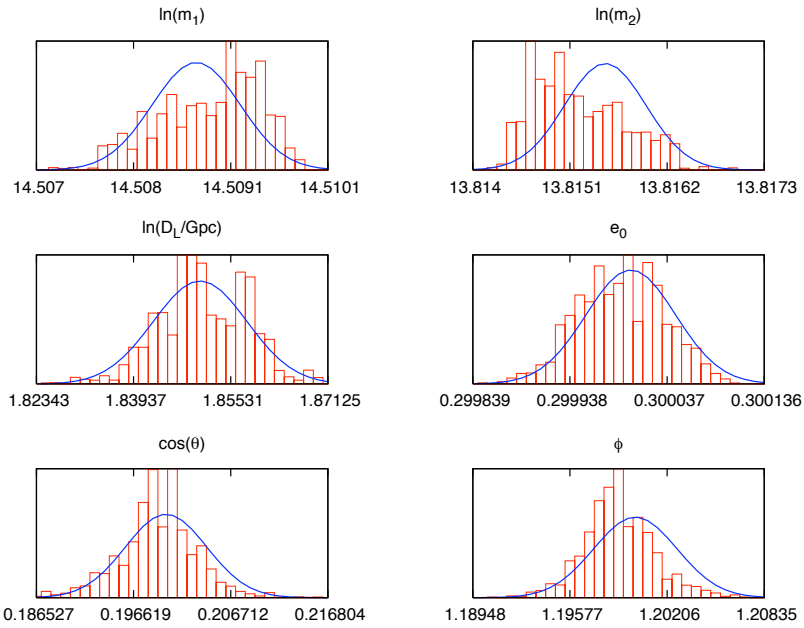

Figure 7.9: The marginalized posterior distribution for several source parameters, including the initial radial eccentricity with injected value $e_0 = 0.3$ and SNR $= 237$. The Fisher matrix prediction for a Gaussian distribution centered on the injected value for each parameter is shown in blue for comparison.

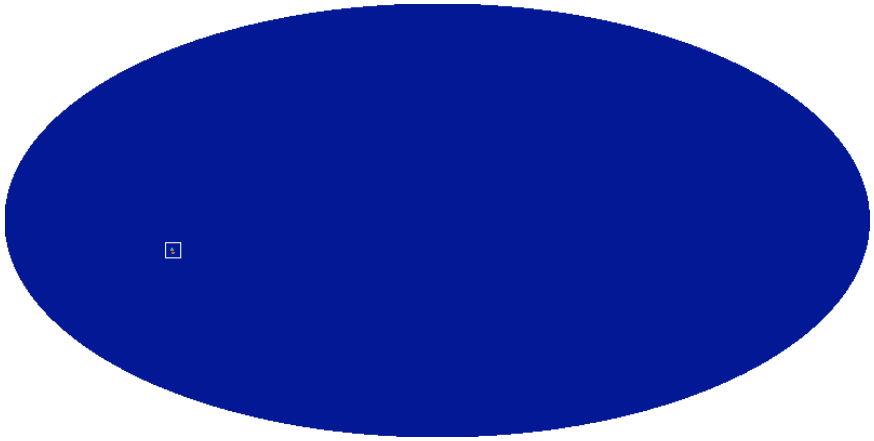

Figure 7.10: Two dimensional posterior distribution of the sky location parameters θ and ϕ projected onto the plane of the sky for a source with initial radial eccentricity $e_0 = 0.3$ and SNR $= 237$. The white box marks the injected parameter values.

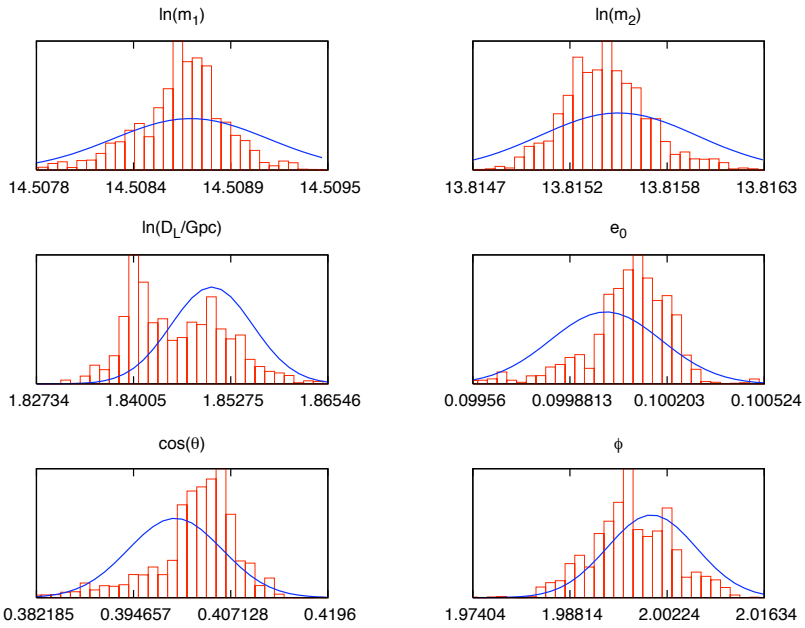

Figure 7.11: The marginalized posterior distribution for several source parameters, including the initial radial eccentricity with injected value $e_0 = 0.1$ and SNR $= 576$. The Fisher matrix prediction for a Gaussian distribution centered on the injected value for each parameter is shown in blue for comparison.

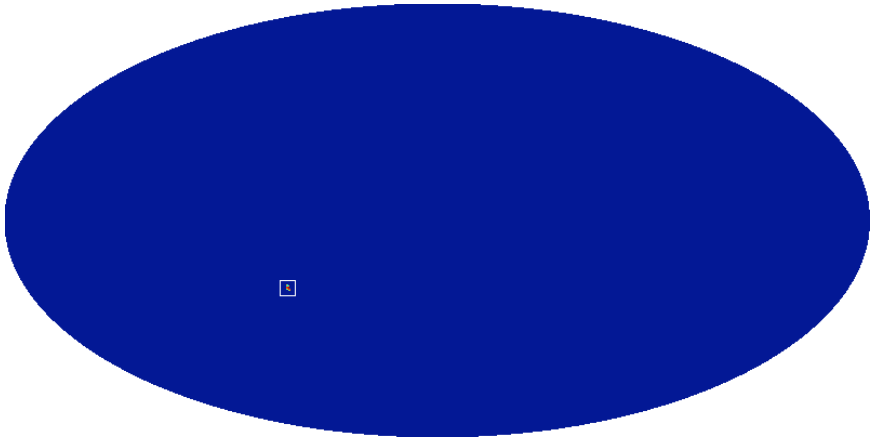

Figure 7.12: Two dimensional posterior distribution of the sky location parameters θ and ϕ projected onto the plane of the sky for a source with initial radial eccentricity $e_0 = 0.1$ and SNR $= 576$. The white box marks the injected parameter values.

sources we would need to perform $2^{17} \sim 10^5$ MCMC parameter estimation studies. The Fisher matrix approximation to the posterior distribution appears to be dependable for values of the initial radial eccentricity that are not too small ($e_0 \sim 10^{-2}$). For smaller values of e_0 the Fisher approximation is not a reliable prediction of the posterior distribution, as seen in an example in Figure 7.13, compared to the corresponding posterior distribution seen in Figure 7.7. A Fisher approximation study of the full parameters space for large values of initial radial eccentricity is left for future work.

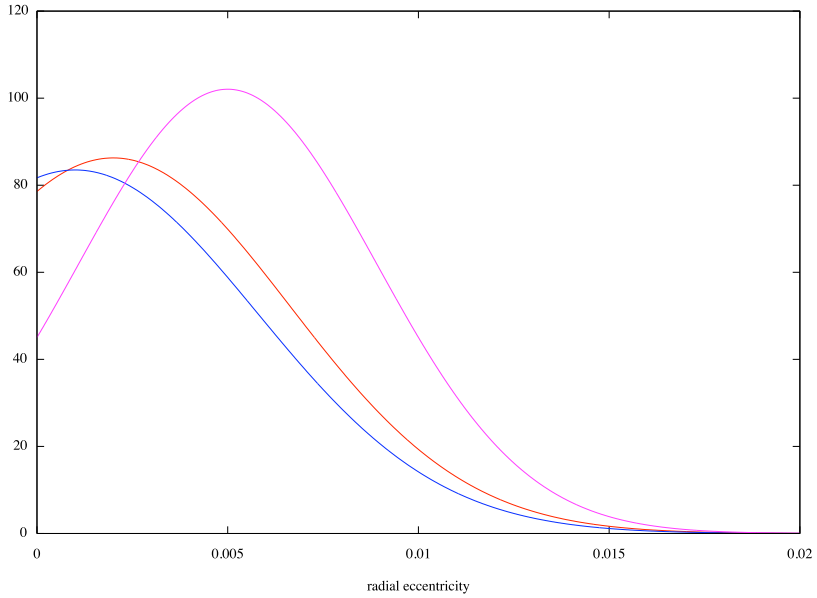

Figure 7.13: The Fisher matrix Gaussian prediction for the distribution of initial radial eccentricity e_0 for Table 7.2, Source 1 for several injected values with $e_0 \sim 10^{-3}$ (e_0 =0.005 in pink, 0.002 in red, 0.001 in blue).

We perform MCMC parameter estimation studies of several representative examples, varying the mass ratio, sky location, distance, eccentricity, and dimensionless spin parameters. We neglect studying the effects of the various initial orientation parameters since we expect in general that the corresponding orbital parameters will

take a wide range of values during the evolution, precession, and orbit of the system regardless of their initial values.

The dimensionless spin parameters χ_1 and χ_2 are varied in Table 7.3 to study the cases of large relative spin and small relative spin. The magnitude of the spin vectors is related to the mass of the black hole $S_i = \chi_i m_i^2$. The posterior distribution for several of the source parameters for these cases are given in Figures 7.14 and 7.15. The Fisher approximation is a reasonable prediction of the width of the posterior distribution for the larger χ_i as seen in Figure 7.14, but the correspondence is degraded for the small χ_i values in Figure 7.15. A Fisher matrix study calculating the Gaussian prediction for the errors in the spin parameters is thus more reliable for larger spin values and in general an MCMC map of the posterior distribution of the spin parameters is a better description of the errors in these parameters.

We expect that the eccentricity parameter will not be highly correlated with the other source parameters since the higher harmonics introduced in the waveform due to eccentricity cannot be simulated by changes in other parameters or their combinations. We indeed find that the initial radial eccentricity is not correlated with the other parameters. Compare the distribution of values for the two masses in Figure 7.16 to the distribution of mass and eccentricity values in Figure 7.17. The two masses are highly correlated since it is the total mass of the system and the ratio of the masses that appear in the waveform. The distribution of eccentricity versus the other source parameters is similar to that seen in Figure 7.17.

7.4 Conclusions

Our studies of the response of the LISA detector to the gravitational wave signal from spinning binary black hole systems in eccentric orbits show that the eccentric-

Table 7.3: Source 3 gives the injected parameter values for Figure 7.14 with large spin values. Source 4 gives the injected parameter values for Figure 7.15 with small spin values.

Parameter	Source 3	Source 4
m_1	$2 \times 10^6 M_\odot$	$2 \times 10^6 M_\odot$
m_2	$1 \times 10^6 M_\odot$	$1 \times 10^6 M_\odot$
D_L	6.36167 Gpc	6.36167 Gpc
e_0	0.1	0.1
a_0	69 M	69 M
χ_1	0.8	0.1
χ_2	0.9	0.11
$\cos\theta$	0.2	0.2
$\cos\theta_L$	-0.5	-0.5
$\cos\theta_{S_1}$	-0.8	-0.8
$\cos\theta_{S_2}$	0.6	0.6
ϕ	1.2	1.2
ϕ_L	2.6	2.6
ϕ_{S_1}	0.4	0.4
ϕ_{S_2}	1.7	1.7
n_0	0.2	0.2
ϕ_0	1.65	1.65
SNR	282	200

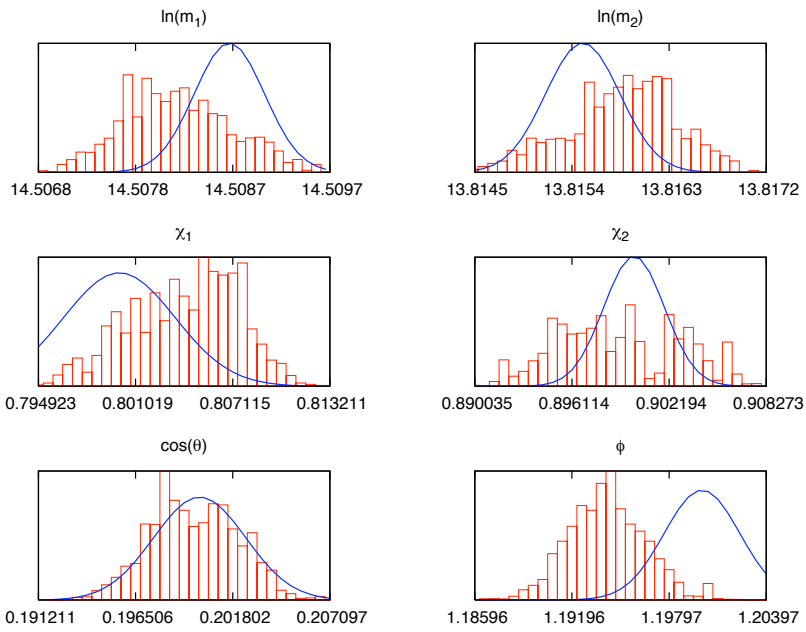

Figure 7.14: The marginalized posterior distribution for several source parameters for a source with SNR = 282, including the dimensionless spin parameters with injected values $\chi_1 = 0.8$ and $\chi_2 = 0.9$ (Table 7.3, Source 3). The Fisher matrix prediction for a Gaussian distribution centered on the injected value for each parameter is shown in blue for comparison.

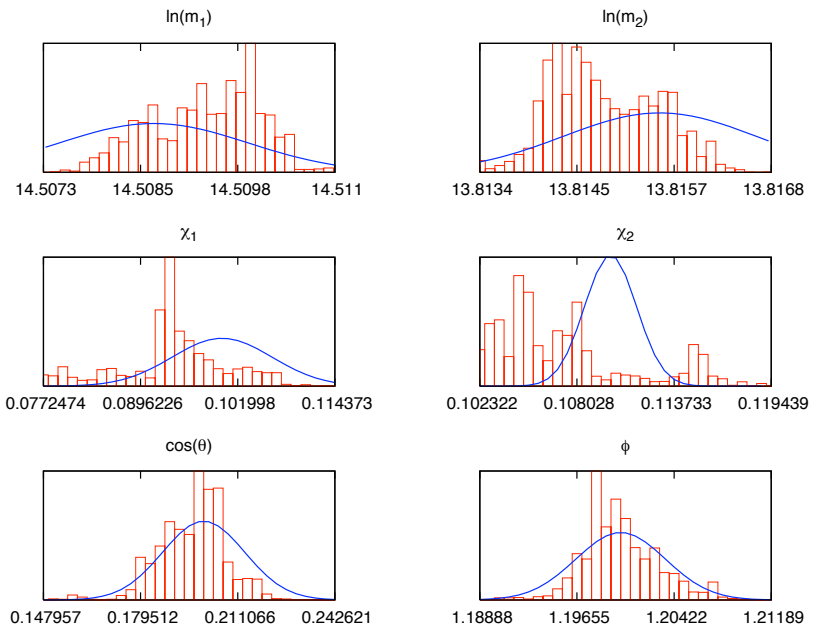

Figure 7.15: The marginalized posterior distribution for several source parameters for a source with SNR = 200, including the dimensionless spin parameters with injected values $\chi_1 = 0.1$ and $\chi_2 = 0.11$ (Table 7.3, Source 4). The Fisher matrix prediction for a Gaussian distribution centered on the injected value for each parameter is shown in blue for comparison.

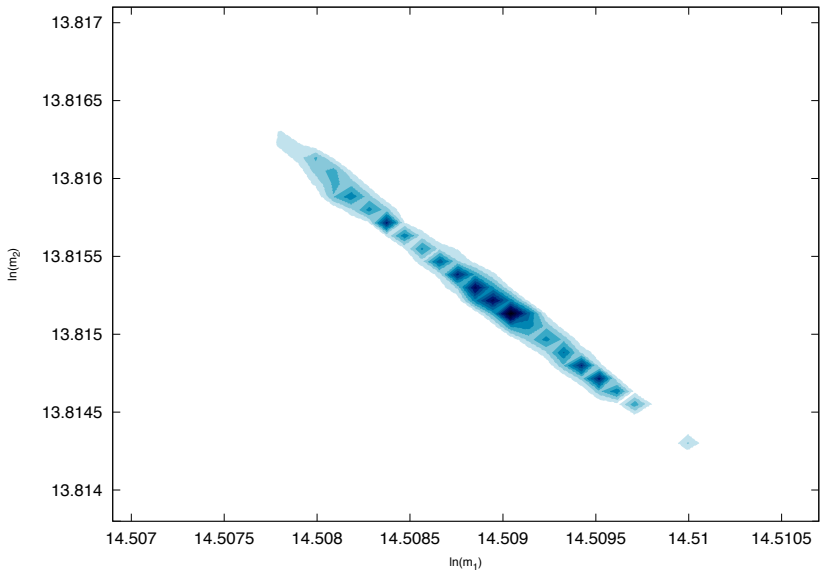

Figure 7.16: Two dimensional posterior distribution showing the correlation of the mass parameters m_1 and m_2 for a source with initial radial eccentricity $e_0 = 0.001$ and SNR = 153.

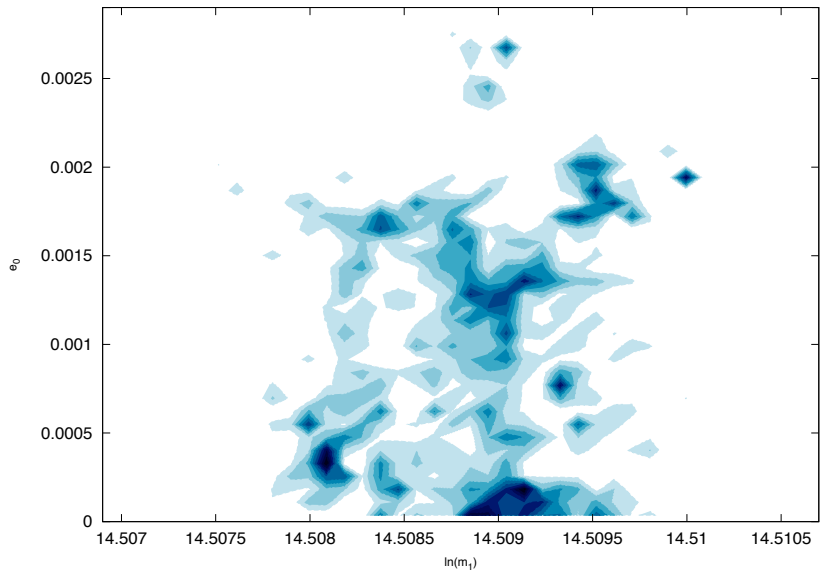

Figure 7.17: Two dimensional posterior distribution of m_1 and e_0 values for a source with initial radial eccentricity $e_0 = 0.001$ and SNR = 153.

ity should not be neglected for LISA data analysis and parameter estimation. The construction of the gravitational waveforms for these general sources to 1.5 PN order establishes the framework for the extension to higher order. Binary black hole wave forms that include eccentricity will be necessary for several of the LISA science goals including constraining galaxy merger scenarios and testing general relativity in the strong field regime near supermassive black holes.

CHAPTER 8
CONCLUSIONS

Once the first direct detections of gravitational waves are made in the next decade and the gravitational wave detector network expands to space with LISA, gravitational wave astronomy will join with electromagnetic observation and cosmic ray detection to increase the breadth of the field of astronomy. The astrophysics that can be done with gravitational wave detectors is enhanced by source modeling and data analysis techniques that allow scientists to dig deep below the noise levels to extract signals of expected forms.

Gravitational wave sources include a possible network of cosmic length strings that will produce a gravitational wave background as well as bursts of gravitational wave radiation that will stand up above the background. These sources have been modeled and our study shows that the next generation of gravitational wave detectors will be able to accurately determine the source parameters.

The most promising source of gravitational waves are inspiraling systems of compact objects such as white dwarf stars, neutron stars, and black holes. Gravitational radiation from such systems has already been indirectly detected through the energy and angular momentum loss observed from binary pulsar systems. The sensitivities and frequency ranges of the next generation of gravitational wave detectors are certain to contain many strong sources of gravitational waves from inspiraling systems.

We present herein the model for the time dependent gravitational waveforms for a general system of binary black holes. We study the LISA instrument response to these signals and determine the parameter uncertainties we should expect for such sources. This work establishes the parameter estimation abilities of LISA for this class of sources and provides the pieces necessary for further studies.

CHAPTER 9

FUTURE WORK

This work on spinning eccentric black hole binaries builds the foundation for further studies including a comprehensive exploration of the parameter space including source sky location, distance, spins, and masses. For sources with initial radial eccentricity greater than $e_0 \sim 0.01$ the Fisher matrix is a good approximation to the posterior distribution. The very large parameter space could be studied quickly using the Fisher approximation, although it is not as useful for the low initial eccentricity cases.

The equations of motion and instantaneous gravitational waveforms have been calculated to the next post-Newtonian order and these pieces can be included systematically as described here. The 2 PN effects include the spin-spin coupling of the two black holes and thus corrections to the precession and evolution of the system. These waveforms can be used to study how well the Advanced LIGO-Virgo network and proposed Einstein Telescope will be able to measure eccentricity and what level of bias could be expected from using circular templates for parameter estimation.

Tests of general relativity near supermassive black holes can also be studied with these general waveforms by adopting alternative theories of gravity for source simulation and determining the residuals left when searching with GR waveforms.

The methods described here for characterizing astrophysical sources of gravitational waves with Markov Chain Monte Carlo techniques are general once a time dependent waveform is known ($h_+(t)$, $h_\times(t)$) for a given source. The detector response for LISA or the ground based detectors can be calculated for any $h_+(t)$ and $h_\times(t)$ and the MCMC methods can be used for parameter estimation. The development of these tools for gravitational wave data analysis has been the work of several

groups, including the Montana Gravitational Wave Astronomy Group at Montana State University. Methods will continue to be improved as the gravitational wave community readies for the new era of frequent gravitational wave detections, but it has already been shown that we will be able to extract a wide range of signals and their various parameters from the noisy data from gravitational wave detectors.

REFERENCES CITED

[1] A. Abramovici et. al. LIGO: The Laser Interferometer Gravitational-Wave Observatory. *Science*, 256(5055):325–333, 1992.

[2] B. Caron et. al. The Virgo interferometer. *Classical and Quantum Gravity*, 14(6):1461, 1997.

[3] P. Bender et. al. LISA Pre-Phase A Report. 1998.

[4] G. Hobbs et. al. The international pulsar timing array project: using pulsars as a gravitational wave detector. 2009.

[5] B. Abbott et. al. Implications for the Origin of GRB 070201 from LIGO Observations. *Astrophys. J.*, 681:1419–1428, 2008.

[6] 12th Gravitational Wave Data Analysis Workshop. *The Mock LISA Data Challenges: from Challenge 1B to Challenge 3*, Cambridge, MA, December 2008. Stanislav Babak et. al.

[7] B. S. Sathyaprakash and S. V. Dhurandhar. Choice of filters for the detection of gravitational waves from coalescing binaries. *Phys. Rev.*, D44:3819–3834, 1991.

[8] Alessandra Buonanno, Yan-bei Chen, and Michele Vallisneri. Detecting gravitational waves from precessing binaries of spinning compact objects: Adiabatic limit. *Phys. Rev.*, D67:104025, 2003.

[9] Ryan N. Lang and Scott A. Hughes. Measuring coalescing massive binary black holes with gravitational waves: The impact of spin-induced precession. *Phys. Rev.*, D74:122001, 2006.

[10] Neil J. Cornish and Edward K. Porter. MCMC Exploration of Supermassive Black Hole Binary Inspirals. *Class. Quant. Grav.*, 23:S761–S768, 2006.

[11] Jeffrey. E. McClintock and Ronald. A. Remillard. Black Hole Binaries. 2003.

[12] Martin G. Haehnelt. Multiple black holes in galactic bulges. *Mon. Not. Roy. Astron. Soc.*, 336:L61, 2002.

[13] M. C. Begelman, R. D. Blandford, and M. J. Rees. Massive black hole binaries in active galactic nuclei. *Nature*, 287:307–309, 1980.

[14] K. G. Arun et. al. Massive Black Hole Binary Inspirals: Results from the LISA Parameter Estimation Taskforce. *Class. Quant. Grav.*, 26:094027, 2009.

[15] M. J. Benacquista. Gravitational radiation from black hole binaries in globular clusters. *Class. Quant. Grav.*, 19:1297–1302, 2002.

[16] Curt Cutler and Michele Vallisneri. LISA detections of massive black hole inspirals: parameter extraction errors due to inaccurate template waveforms. *Phys. Rev.*, D76:104018, 2007.

[17] Carlos F. Sopuerta and Nicolas Yunes. Towards Tests of Alternative Theories of Gravity with LISA. *Proceedings of the Twelfth Marcel Grossmann Meeting on General Relativity*, 2010.

[18] Albert Einstein. On the General Theory of Relativity. *Sitzungsber. Preuss. Akad. Wiss. Berlin (Math. Phys.)*, 1915:778–786, 1915.

[19] R. A. Hulse and J. H. Taylor. Discovery of a pulsar in a binary system. *Astrophys. J.*, 195:L51–L53, 1975.

[20] http://www.ligo.caltech.edu/.

[21] http://www.virgo.infn.it/.

[22] H. Luck. The GEO600 project. *Class. Quant. Grav.*, 14:1471–1476, 1997.

[23] http://www.geo600.org/.

[24] LISA International Science Team. LISA: Probing the Universe with Gravitational Waves, 2007. www.srl.caltech.edu/lisa/documents/lisa_science_case.pdf.

[25] N. Jarosik et. al. Seven-Year Wilkinson Microwave Anisotropy Probe (WMAP) Observations: Sky Maps, Systematic Errors, and Basic Results. 2010.

[26] R. Weiss. Quarterly Progress Report of RLE. *MIT*, (54), 1972.

[27] Michele Maggiore. *Gravitational Waves*, volume Volume 1: Theory and Experiments. Oxford University Press, 2008.

[28] LIGO Scientific Collaboration and Virgo Collaboration. Predictions for the Rates of Compact Binary Coalescences Observable by Ground-based Gravitational-wave Detectors. 2010.

[29] http://lisa.nasa.gov/.

[30] Seth E. Timpano, Louis J. Rubbo, and Neil J. Cornish. Characterizing the galactic gravitational wave background with LISA. *Phys. Rev.*, D73:122001, 2006.

[31] Proceedings of the 19th Workshop on General Relativity and Gravitation in Japan. *Probing strong-field gravity and black holes with gravitational waves.* Scott A. Hughes, 2010.

[32] Massimo Tinto, J.W. Armstrong, and Frank B. Esabrook. Modulator noise suppression in the LISA Time-Delay Interferometric combinations. *Phys. Rev. D*, 2007.

[33] F. B. Estabrook, M. Tinto, and J. W. Armstrong. Time delay analysis of LISA gravitational wave data: Elimination of spacecraft motion effects. *Phys. Rev. D*, 62, 2000.

[34] Neil J. Cornish and Louis J. Rubbo. LISA response function. *Phys. Rev. D*, 67(022001), 2003.

[35] Neil J. Cornish and Ronald W. Hellings. The Effects of orbital motion on LISA time delay interferometry. *Class. Quant. Grav.*, 20:4851–4860, 2003.

[36] N. Metropolis, A.W. Rosenbluth, M.N. Rosenbluth, A.H. Teller, and E. Teller. Equation of State Calculations by Fast Computing Machines. *Journal of Chemical Physics*, 21:1087, 1953.

[37] W.K. Hastings. *Biometrika*, 97:57, 1970.

[38] Neil J. Cornish and Jeff Crowder. LISA Data Analysis using MCMC methods. *Phys. Rev. D*, 72(043005), 2005.

[39] P.C. Gregory. *Bayesian Logical Data Analysis for the Physical Sciences: A Comprehensive Approach with Mathmatica Support.* Cambridge University Press, 2005.

[40] P.C. Gregory. A Bayesian Analysis of Extrasolar Planet Data for HD 73526. *Astrophys. J.*, 631:1198–1214, 2005.

[41] Joey Shapiro Key and Neil J. Cornish. Characterizing the Gravitational Wave Signature from Cosmic String Cusps. *Phys. Rev.*, D79:043014, 2009.

[42] Tyson B. Littenberg and Neil J. Cornish. Parallel Tempering and Thermodynamic Integration. *in preparation*, 2010.

[43] Tyson B. Littenberg and Neil J. Cornish. A Bayesian Approach to the Detection Problem in Gravitational Wave Astronomy. *Phys. Rev.*, D80:063007, 2009.

[44] Neil J. Cornish. Detection Strategies for Extreme Mass Ratio Inspirals. *arXiv*, gr-qc/0804.3323v2, 2008.

[45] Marc van der Sluys et. al. Parameter estimation of spinning binary inspirals using Markov-chain Monte Carlo. *Class. Quant. Grav.*, 25:184011, 2008.

[46] T.W.B. Kibble. Topology of Cosmic Domains and Strings. *J. Phys. A*, 1387:9, 1976.

[47] A. Vilenkin and E.P.S. Shellard. *Cosmic Strings and Other Topological Defects*. Cambridge University, Cambridge, 2000.

[48] Uros Seljak, Anze Slosar, and Patrick McDonald. Cosmological parameters from combining the Lyman-alpha forest with CMB, galaxy clustering and SN constraints. *JCAP*, 2006.

[49] Xavier Siemens, Vuk Mandic, and Jolien Creighton. Gravitational wave stocastic background from cosmic (super)strings. *Phys. Rev. Lett.*, 98, 2007.

[50] S. Sarangi and S.H. Tye. Cosmic String Production Towards the End of Brane Inflation. *Physics Letters B*, 536(185), 2002.

[51] V. Berezinsky, B. Hnatyk, and A. Vilenkin. Gamma ray bursts from superconducting cosmic strings. *Phys. Rev. D*, 64(043004), 2001.

[52] Thibault Damour and Alexander Vilenkin. Gravitational wave bursts from cosmic strings. *Phys. Rev. Lett.*, 85:3761–3764, 2000.

[53] Nicholas Jones, Horace Stocia, and S.H. Tye. Brane Interaction as the Origin of Inflation. *JHEP*, 0207, 2002.

[54] Mark G. Jackson, Nicholas Jones, and Joseph Polchinski. Collisions of Cosmic F- and D-strings. *JHEP*, 0510, 2005.

[55] Nicholas Jones, Horace Stocia, and S.H. Tye. The Production, Spectrum and Evolution of Cosmic Strings in Brane Inflation. *Physics Letters B*, 563, 2003.

[56] Edmund J. Copeland, Robert C. Myers, and Joseph Polchinski. Cosmic F- and D-strings. *JHEP*, 0406, 2004.

[57] G. Dvali and A. Vilenkin. Formation and evolution of cosmic D-strings. *JCAP*, 0403, 2004.

[58] Thibault Damour and Alexander Vilenkin. Gravitational wave bursts from cusps and kinks on cosmic strings. *Phys. Rev. D*, 64(064008), 2001.

[59] T. Damour and A. Vilenkin. Gravitational radiation from cosmic (super)strings: bursts, stochastic background, and observational window. *Phys. Rev. D*, 71(063510), 2005.

[60] X. Siemens, Jolien Creighton, Irit Maor, Saikat Ray Majumder, Kipp Cannon, and Jocelyn Read. Gravitational wave bursts from cosmic (super)strings: Quantitative analysis and constraints. *Phys. Rev. D*, 73(105001), 2006.

[61] M. R. DePies and C. J. Hogan. Stochastic Gravitational Wave Background from Light Cosmic Strings. *Phys. Rev. D*, 75(125006), 2007.

[62] X. Siemens, J.S. Key, and N.J. Cornish. Constraining Cosmic String Networks with LISA Observations. *in preparation*, 2010.

[63] Konrad Kuijken, Xavier Siemens, and Tanmay Vachaspati. Microlensing by Cosmic Strings. *MNRAS*, 384(161), 2008.

[64] David F. Chernoff and S.-H. Henry Tye. Cosmic String Detection via Microlensing of Stars. *astro-ph*, 2007.

[65] X. Siemens and K.D. Olum. Cosmic String Cusps with Small-Scale Structure: Their Forms and Gravitational Waveforms. *Phys. Rev. D*, 68(085017), 2003.

[66] Stanislav Babak et. al. Report on the second Mock LISA Data Challenge. *Class. Quant. Grav.*, 25, 2008.

[67] Thomas A. Prince, Massimo Tinto, Shane L. Larson, and J.W. Armstrong. The LISA Optimal Sensitivity. *Phys. Rev. D*, 66, 2002.

[68] Warren G. Anderson, Patrick R. Brady, Jolien D. E. Creighton, and Eanna E. Flanagan. An excess power statistic for detection of burst sources of gravitational radiation. *Phys. Rev. D*, 63(042003), 2001.

[69] P. M. Goggans and Y. Chi. Using thermodynamic integration to calculate the posterior probability in Bayesian model selection problems. In Gary J Erickson and Yuxiang Zhai, editors, *Bayesian Inference and Maximum Entropy Methods in Science and Engineering: 23rd International Workshop*, volume 707, pages 59–66. AIP Conference Proceedings, 2004.

[70] John Kormendy and Douglas Richstone. Inward bound: The Search for supermassive black holes in galactic nuclei. *Ann. Rev. Astron. Astrophys.*, 33:581, 1995.

[71] John Magorrian et. al. The Demography of Massive Dark Objects in Galaxy Centres. *Astron. J.*, 115:2285, 1998.

[72] Ramesh Narayan. Black holes in astrophysics. *New Journal of Physics*, 7(1):199, 2005.

[73] Kristen Menou, Zoltan Haiman, and Vijay K. Narayanan. The Merger History of Supermassive Black Holes in Galaxies. *Astrophys. J.*, 558:535–542, 2001.

[74] R. Schödel et. al. A star in a 15.2-year orbit around the supermassive black hole at the centre of the Milky Way. *Nature*, 419:694–696, October 2002.

[75] F. Eisenhauer et. al. A Geometric Determination of the Distance to the Galactic Center. *Astrophys. J.*, 597:L121–L124, 2003.

[76] A. M. Ghez et. al. The First Measurement of Spectral Lines in a Short-Period Star Bound to the Galaxy's Central Black Hole: A Paradox of Youth. *Astrophys. J.*, 586:L127–L131, 2003.

[77] A. M. Ghez et. al. Stellar Orbits Around the Galactic Center Black Hole. *Astrophys. J.*, 620:744–757, 2005.

[78] Z.-Q. Shen, K. Y. Lo, M.-C. Liang, P. T. P. Ho, and J.-H. Zhao. A size of ˜1AU for the radio source Sgr A* at the centre of the Milky Way. *Nature*, 438:62–64, November 2005.

[79] David Merritt and Laura Ferrarese. Black Hole Demographics from the M(BH)-sigma Relation. *Mon. Not. Roy. Astron. Soc.*, 320:L30, 2001.

[80] Scott Tremaine et. al. The slope of the black-hole mass versus velocity dispersion correlation. *Astrophys. J.*, 574:740–753, 2002.

[81] Martin G. Haehnelt. Joint Formation of Supermassive Black Holes and Galaxies. *arXiv*, astro-ph/0307378, 2003.

[82] David Merritt, Stefan Harfst, and Gianfranco Bertone. Collisionally regenerated dark matter structures in galactic nuclei. *Phys. Rev. D*, 75(4):043517, Feb 2007.

[83] Alberto Sesana, Marta Volonteri, and Francesco Haardt. The imprint of massive black hole formation models on the LISA data stream. *Mon. Not. Roy. Astron. Soc.*, 377:1711–1716, 2007.

[84] Miloš Milosavljević David Merritt. Massive Black Hole Binary Evolution. *Living Reviews in Relativity*, 8(8), 2005.

[85] Milos Milosavljevic and David Merritt. The final parsec problem. *AIP Conf. Proc.*, 686:201–210, 2003.

[86] Kelly Holley-Bockelmann and Steinn Sigurdsson. A Full Loss Cone For Triaxial Galaxies. *arXiv*, astro-ph/0601520, 2006.

[87] Peter Berczik, David Merritt, Rainer Spurzem, and Hans-Peter Bischof. Efficient Merger of Binary Supermassive Black Holes in Non-Axisymmetric Galaxies. *Astrophys. J.*, 642:L21, 2006.

[88] Martin G. Haehnelt. Hierarchical build-up of galactic bulges and the merging rate of supermassive binary black holes. *Class. Quant. Grav.*, 20:S31, 2003.

[89] P. C. Peters and J. Mathews. Gravitational Radiation from Point Masses in a Keplerian Orbit. *Physical Review*, 131:435–440, July 1963.

[90] Alberto Sesana, Francesco Haardt, and Piero Madau. Interaction of massive black hole binaries with their stellar environment: I. Ejection of hypervelocity stars. *Astrophys. J.*, 651:392–400, 2006.

[91] Ryan M. O'Leary, Frederic A. Rasio, John M. Fregeau, Natalia Ivanova, and Richard O'Shaughnessy. Binary Mergers and Growth of Black Holes in Dense Star Clusters. *Astrophys. J.*, 637:937–951, 2006.

[92] Kayhan Gultekin, M. Coleman Miller, and Douglas P. Hamilton. Three-Body Dynamics with Gravitational Wave Emission. *Astrophys. J.*, 640:156–166, 2006.

[93] Emanuele Berti. LISA observations of massive black hole mergers: event rates and issues in waveform modelling. *Class. Quant. Grav.*, 23:S785–S798, 2006.

[94] P. C. Peters. Gravitational Radiation and the Motion of Two Point Masses. *Physical Review*, 136:1224–1232, November 1964.

[95] Pau Amaro-Seoane et. al. Astrophysics, detection and science applications of intermediate- and extreme mass-ratio inspirals. *Class. Quant. Grav.*, 24:R113–R169, 2007.

[96] Monica Colpi, Lucio Mayer, and Fabio Governato. Dynamical friction and the evolution of satellites in virialized halos: the theory of linear response. *arXiv*, astro-ph/9907088, 1999.

[97] Massimo Dotti, Monica Colpi, and Francesco Haardt. Inspiral of double black holes in gaseous nuclear disks. *arXiv*, astro-ph/0602013, 2006.

[98] Peter Berczik, David Merritt, and Rainer Spurzem. Long-Term Evolution of Massive Black Hole Binaries. II. Binary Evolution in Low-Density Galaxies. *Astrophys. J.*, 633:680–687, 2005.

[99] Philip J. Armitage and Priyamvada Natarajan. Eccentricity of supermassive black hole binaries coalescing from gas rich mergers. *Astrophys. J.*, 634:921–928, 2005.

[100] Loren Hoffman and Abraham Loeb. Dynamics of triple black hole systems in hierarchically merging massive galaxies. *Mon. Not. Roy. Astron. Soc.*, 377:957–976, 2007.

[101] Miroslav Micic, Kelly Holley-Bockelmann, Steinn Sigurdsson, and Tom Abel. Supermassive Black Hole Growth and Merger Rates from Cosmological N-body Simulations. *Mon. Not. Roy. Astron. Soc.*, 380:1533, 2007.

[102] Ryan N. Lang and Scott A. Hughes. Localizing merging massive black hole binaries with gravitational waves. *ApJ*, 2007.

[103] Janos Majar and Matyas Vasuth. Gravitational waveforms for spinning compact binaries. *Phys. Rev.*, D77:104005, 2008.

[104] Lawrence E. Kidder. Coalescing binary systems of compact objects to post-Newtonian 5/2 order. 5. Spin effects. *Phys. Rev.*, D52:821–847, 1995.

[105] Linqing Wen. On the Eccentricity Distribution of Coalescing Black Hole Binaries Driven by the Kozai Mechanism in Globular Clusters. *The Astrophysical Journal*, 598:419, 2003.

[106] Ryan M. O'Leary, Bence Kocsis, and Abraham Loeb. Gravitational waves from scattering of stellar-mass black holes in galactic nuclei. *MNRAS*, 395(4):2127 – 2146, 2009.

[107] N. J. Cornish and J. S. Key. Computing waveforms for spinning compact binaries in quasi-eccentric orbits. *in preparation*, 2010.

[108] Thibault Damour and N Deruelle. General relativisitc celestial mechanics of binary systems I. The post-Newtonian motion. *Ann. Inst. Henri Poincare*, 43(1):107–132, 1985.

[109] Christian Konigsdorffer and Achamveedu Gopakumar. Post-Newtonian accurate parametric solution to the dynamics of spinning compact binaries in eccentric orbits: The leading order spin-orbit interaction. *Phys. Rev.*, D71:024039, 2005.

[110] Manuel Tessmer. Gravitational waveforms from unequal-mass binaries with arbitrary spins under leading order spin-orbit coupling. *Phys. Rev.*, D80:124034, 2009.

[111] W. Junker and G. Schaefer. Binary systems - Higher order gravitational radiation damping and wave emission. *MNRAS*, 254:146–164, January 1992.

[112] B.M. Barker and R.F. O'Connell. *Gen. Relativ. Gravit.*, 5(539), 1974.

[113] Zoltan Keresztes, Balazs Mikoczi, and Laszlo A. Gergely. The Kepler equation for inspiralling compact binaries. *Phys. Rev.*, D72:104022, 2005.

[114] Jing Zeng and Clifford M. Will. Application of energy and angular momentum balance to gravitational radiation reaction for binary systems with spin-orbit coupling. *Gen. Rel. Grav.*, 39:1661–1673, 2007.

[115] L. Blanchet and G. Schaefer. Higher order gravitational radiation losses in binary systems. *MNRAS*, 239:845–867, August 1989.

[116] Craig W. Lincoln and Clifford M. Will. Coalescing binary systems of compact objects to (*post*)5/2-Newtonian order: Late-time evolution and gravitational-radiation emission. *Phys. Rev. D*, 42(4):1123–1143, Aug 1990.

[117] Jonathan R. Gair. Approximate waveform templates for detection of extreme mass ratio inspirals with LISA. *Proceedings of the Eleventh Marcel Grossmann Meeting on General Relativity*, 2007.